



Title	Studies on the Photoinduced Charge-Transfer Processes on Metal-Organic Framework Nanoparticles and Their Composites
Author(s)	Choi, Jun Rye
Citation	大阪大学, 2010, 博士論文
Version Type	VoR
URL	https://hdl.handle.net/11094/27634
rights	
Note	

The University of Osaka Institutional Knowledge Archive : OUKA

<https://ir.library.osaka-u.ac.jp/>

The University of Osaka

Studies on the Photoinduced Charge-Transfer Processes
on Metal-Organic Framework Nanoparticles and Their
Composites

(多孔性金属-有機骨格ナノ粒子およびその複合材料
における光誘起電荷移動過程に関する研究)

Jun Rye Choi

2010

29 11545

Studies on the Photoinduced Charge-Transfer Processes on Metal-Organic Framework Nanoparticles and Their Composites

(多孔性金属-有機骨格ナノ粒子およびその複合材料
における光誘起電荷移動過程に関する研究)

Jun Rye Choi

2010

Preface

The studies presented in this thesis were carried out under the direction of Professor Tetsuro Majima, the Institute of Scientific and Industrial Research (SANKEN), Osaka University during October 2007 to September 2010.

The object of this thesis is concerned with the studies on the photoinduced charge-transfer processes on metal-organic framework nanoparticles and their composites using various spectroscopic methods including single-particle fluorescence microscopy as well as time-resolved spectroscopic method. The author hopes that the results and conclusions presented in this thesis contribute to the further understanding of the photochemical properties of MOFs and the development of advanced photocatalysts as well as for new applications including photoelectronic and optical devices.

Jun Rye Choi

Department of Applied Chemistry
Graduate School of Engineering
Osaka University
2010

Contents

General Introduction.....	1	
 Chapter 1		
Photoinduced Charge-Transfer Processes on MOF-5 Nanoparticles.....	11	
 Chapter 2		
Europium-Based Metal-Organic Framework as a Photocatalyst.....	49	
 Chapter 3		
Host-Guest Interactions in MOF Nanoparticles Using a Polarity-Sensitive Probe.....	69	
 General Conclusions.....		89
 List of Publications.....		91
 Acknowledgements.....		93

General Introduction

It is important to understand and predict the photophysical and photochemical properties of chromophores in various metal-organic materials applications since a control of the spatial interactions of chromophores is still a significant challenge.¹⁻³ Many types of intermolecular forces including hydrogen bond and π - π stacking, which influence the packing of molecules in a crystal, also make a prediction of the geometry of a molecular assembly complicate. Metal-organic frameworks (MOFs) are porous and crystalline materials consisting of either metal ions or clusters linked by organic groups, which provide structural rigidity, high porosity, and well-defined

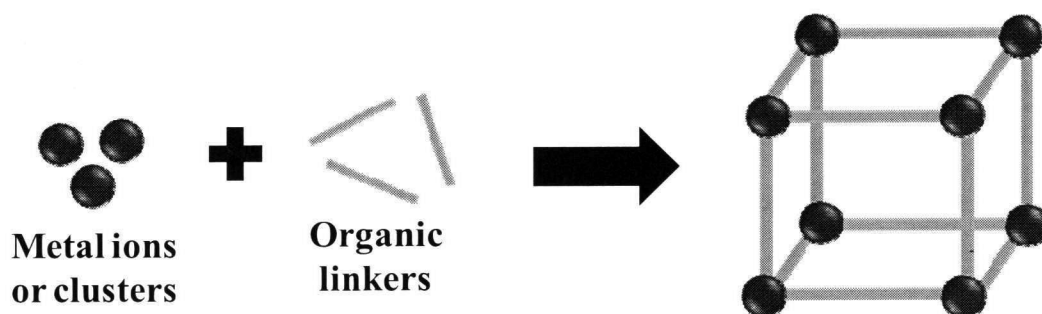


Figure 1. Schematic representation of the definition of metal-organic frameworks (MOFs). Metal atoms are bridged by ligands to form 3D structure.

architectures (Figure 1).⁴⁻⁷ These properties have attracted significant research interest from numerous applications, such as gas storage,^{8,9} catalysis,¹⁰ separations,¹¹ drug delivery,¹² and sensors.¹³ A preliminary synthesis of MOFs was reported by Tomic in 1965.¹⁴ And, a crystalline, polymeric compound, Cu(II) tricyanomethanide was reported by Biondi in 1965.¹⁵ R. Robson reported on the design of scaffold-like materials using Cu(I) ions as a central metal ion and tetracyanotetraphenylmethane as a organic linker in 1990's.¹⁶ The research groups of O. M. Yaghi defined the term of MOF in 1995¹⁷ and reported the structure of MOF-5.¹⁸ They also reported the synthesis and its structural characteristics for a series of isorecticular MOF structures with different molecules acting as organic linkers (Figure 2).¹⁹

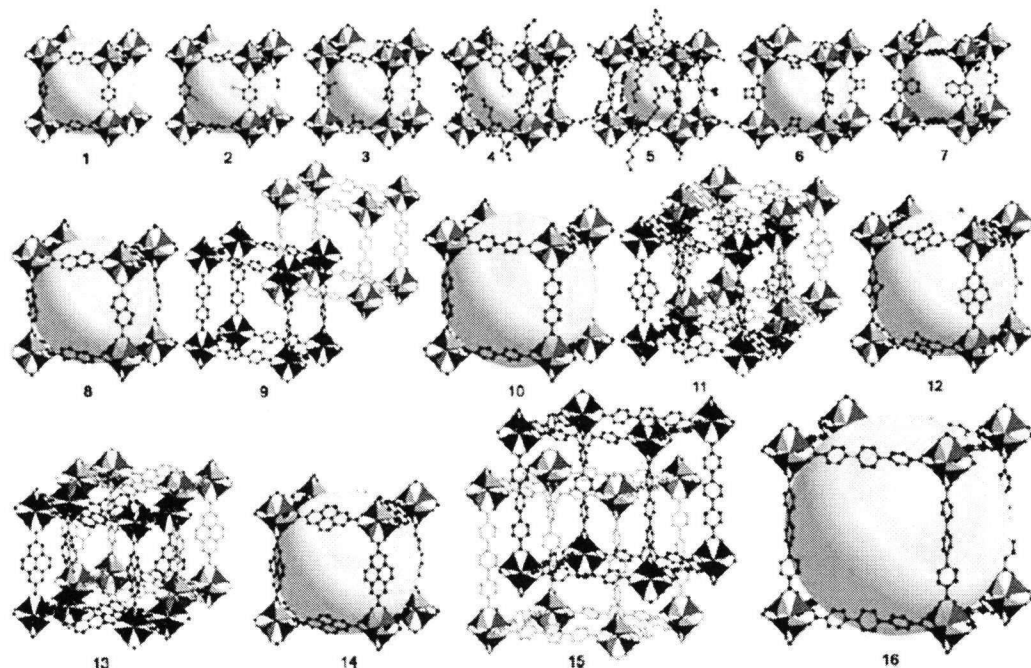


Figure 2. A series of isoreticular metal-organic frameworks (IRMOFs), in which each member shares the same cubic topology, has been produced (adapted from ref. 19).

Contrary to classical solid-state catalysts like zeolites, the pore size, shape, and dimensionality of MOFs can be easily controlled by changing the constituent metals and bridging organic linkers.¹⁹ In particular, MOFs provide very large specific surface areas even above $5900 \text{ m}^2 \text{ g}^{-1}$ and specific pore volumes of up to $2 \text{ cm}^3 \text{ g}^{-1}$, of which value is the highest ones ever reported for any porous material.²⁰ MOFs have an exceptionally open coordination sites, which eventually provide the free space even more than 90% of the crystal volume.¹⁹ Furthermore, it is possible to achieve fine control over the chemical environment and the topology of the internal voids by selecting appropriate building blocks and their interaction. However, the presence of organic building blocks makes MOFs noticeably unstable towards relatively high temperature, chemical agents and even to moisture compared to zeolite as a typical very stable solid-state catalyst.

MOFs results in a wide range of emissive phenomena due to its chemical nature consisting of both an organic ligand and a metal ion. Fluorescence from MOFs directly results from organic linking group of the framework if this moiety is highly conjugated and absorb light in the UV and visible region,^{21,22} mainly through either ligand to metal charge transfer (LMCT)²³ or metal to ligand charge transfer (MLCT).^{24,25} Emission can also result from the central metal ions or its

clusters by usually involving lanthanide ions incorporated into the coordination framework.^{26,27} Guest molecules can also present fluorescent properties of MOFs through exciplex formation.²⁸

Lanthanide-based MOFs (Ln-MOFs), in particular case of Tb^{3+} and Eu^{3+} incorporated in organic framework, have been fascinating due to their versatile coordination geometry, unique luminescent and magnetic properties, and possible high framework stability to water.²⁶ Ln-MOFs are further attractive because the organic linker can serve as an antenna that enhance the lanthanide emission (Figure 3). Recently, several Ln-MOFs with interesting photophysical properties, of which luminescence is rather strongly coupled to its porosity, have been reported.²⁶

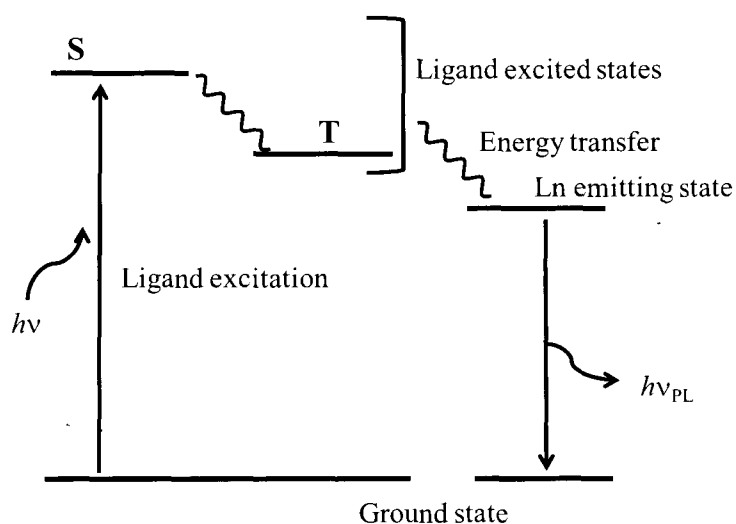


Figure 3. Schematic representation of the antenna effect adapted from ref. 26.

MOFs can be designed to meet the general structural requirements for making MOFs suitable for acting as semiconductors. For example, irradiation of MOFs results in charge separation followed by either the electron or hole migration through the whole particle. The resultant electrons and holes exhibit a typical decaying time constant with submillisecond scale returning to the neutral ground state through charge recombination.²⁹ These properties of MOFs actually plays an important role in photocatalytic reduction or oxidation process of a foreign molecules adsorbed in MOFs framework.

MOFs in the nanosized particles have very unique properties to encapsulate guest molecules. This encapsulation accompanied to conformational changes, photophysical dynamics and intermolecular interaction for both the host and guest molecular system. Due to homogeneous framework of MOFs, the guest molecules can be used as a molecular probe to directly explore the local structures, molecular diffusion, and chemical reactions in MOFs structure if we apply a low dimensional spectroscopic method to investigate the encapsulated MOFs.

As a representative application of low-dimensional spectroscopic method, single-molecule

spectroscopy is an exciting new area of research. It aims at studying the physical and optical properties of individual molecules instead of measuring the properties of a large ensemble. Actually, it also proved to be a powerful tool for investigating heterogeneous systems because it allows us to study the samples with varying probing position in the sample, which impacts the local behavior of molecules to be examined and characterized. The detection of the fluorescence resulted from a single-molecule at room temperature has been published for the first time in 1990.³⁰ They have used pulsed laser excitation configuration for flowing chromophore to minimize the observing volume and light scattering that obscure the signal from a single fluorophore. To observe single-molecule fluorescence, the advanced methods like a wide-field and confocal fluorescence microscopy (Figure 4)³¹ were also introduced in this research field.

In wide-field microscopy like the total internal reflection fluorescence microscopy (TIRFM), a CCD (charge coupled device) camera is adapted to record a fluorescent events taking place in the several hundred square micrometers under volumetric excitation. The resolvable spot size in horizontal direction is limited by optical diffraction, but the resolution in longitudinal direction is not so high enough due to rather large excitation volume and low signal-to-noise ratio. Working with TIRFM implies an optical excitation through an evanescent field which is an electromagnetic wave accompanied with total internal reflection of illuminated light. The penetration depth for the evanescent field in glass-water interface is ca. 200 nm. By combining the total internal reflection and volumetric excitation, TIRFM is advantageous in visualizing the fluorescence from single molecules immobilized or located at the interface (e.g., a glass surface) with a very low background noise using an evanescent field and thus has been applied to the investigation of the temporal dynamics of biomolecules (e.g., DNA, proteins, and enzymes) labeled with dyes, which provides information that is useful for revealing various biological functions at the molecular level.³²

In confocal microscopy, the objective lens is used to focus the excitation light to diffraction limited area. The fluorescence generated by a single molecule residing in the confocal volume can be collected by the same objective lens. Before reaching the detector, the fluorescence light passes an appropriate optical filters and a pinhole to reject background fluorescence from out of focus

light.

The emitted fluorescence can be measured by a point detector, such as an avalanche photodiode (APD), which very efficiently detects photons while having a low dark current, resulting in a good signal-to-noise ratio. The confocal microscopy is widely used for the detection of a molecule freely diffusing in solution, often referred to as fluorescence correlation spectroscopy (FCS),³³ which

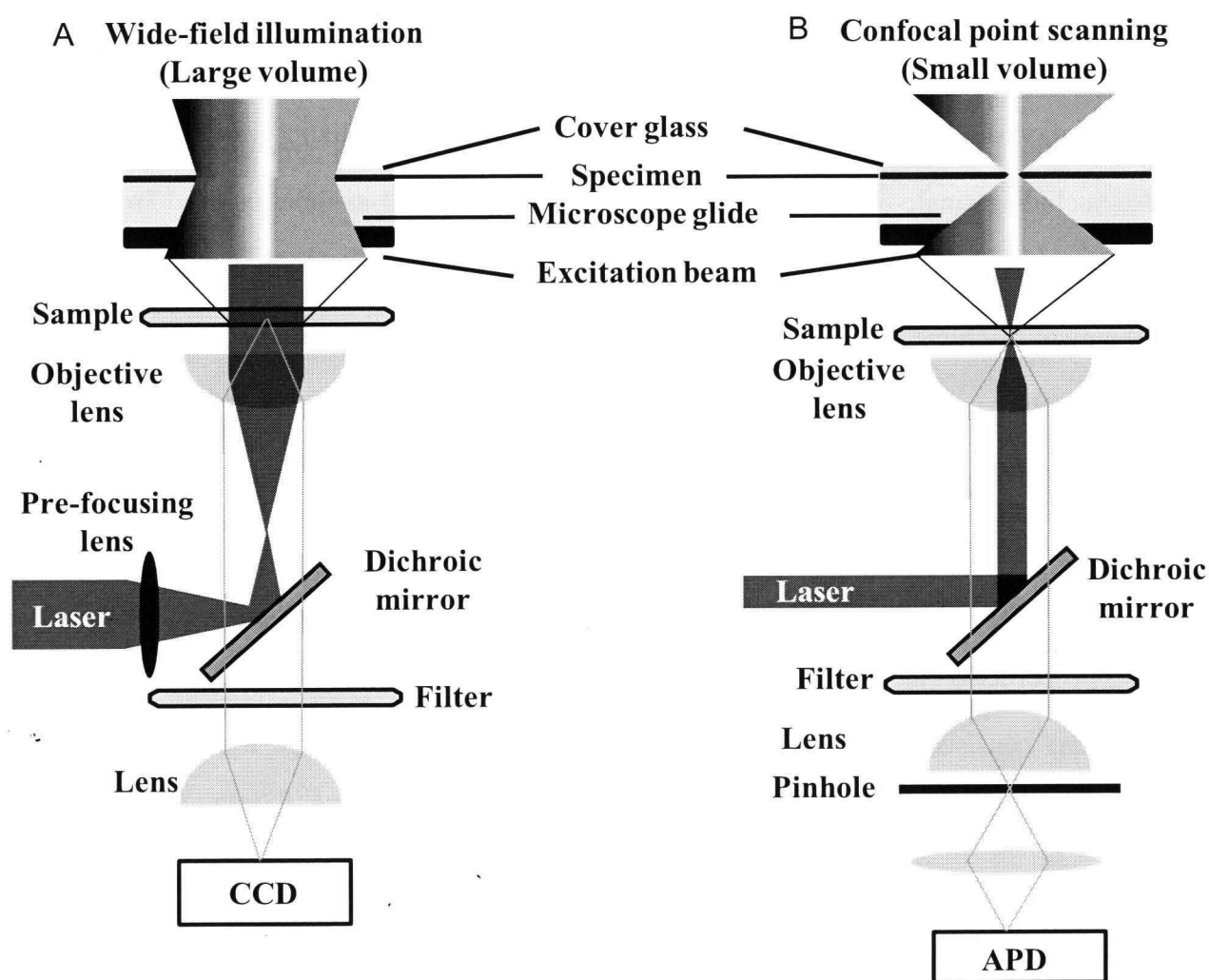


Figure 4. (A) Illustration of wide-field fluorescence microscopy setup. A collimated laser beam is focused into the back-focal plane of the objective to realize a uniform field of illumination. The emission is collected through the same objective and, after passing through filters to remove excitation and scattering light, imaged onto the CCD detector. (B) Illustration of confocal fluorescence microscopy setup. The excitation light is focused *via* an objective lens into a diffraction limited spot. The fluorescence light from the spot is collected by the same objective and passed through optical filters to remove excitation and scattering light. A pinhole is inserted at an image plane to reject scattering/fluorescence light that is not incident from the focal point. Finally, photons are detected by an avalanche photodiode (APD). Adapted from ref. 31.

enables us to investigate and clarify the binding interactions, such as protein-ligand binding and DNA hybridization, by measuring the correlation time of diffusing molecules into the confocal volume. These techniques for single molecule fluorescence detection have advantages superior to the conventional ones that relies on the bulk sample, providing us with opportunities such as the ultimate high sensitivity, the possible observations of the properties hidden in ensemble measurements (subpopulation existing in the sample), and eliminating the need for synchronization.

In this thesis, we try to understand an interfacial electron transfer between photoexcited MOFs particles and various organic compounds as photocatalysts by utilizing various spectroscopic methods including single-particle fluorescence microscopy as well as time-resolved spectroscopic method. There is no precedent study to evaluate detailed mechanisms of photophysical and photochemical reactions for MOFs as well as host-guest interactions in individual MOFs particles until now. Further understanding of the photoinduced redox processes on the MOFs should lead to novel developments of efficient photocatalytic and photoelectrochemical systems with a chemical specificity. Furthermore, a thorough examination of this issue will help us to better understand the molecular interactions within nanopores and provide an exciting new direction for control of materials properties on the molecular level.

This thesis consists of three chapters. Chapter 1, photoinduced charge transfer processes on MOF-5 nanoparticles was investigated by using the time-resolved diffuse reflectance (TDR) and fluorescence spectroscopies. Chapter 2, we investigated the size-selective one-electron oxidation processes of organic compounds under the photoirradiation of nanosized and micro-sized Eu-MOF particles by combining time-resolved emission and absorption spectroscopy, confocal microscopy, and a theoretical calculation based on the Marcus theory. Chapter 3, we carried out in situ observations of host-guest interactions in individual dye encapsulated MOFs by utilizing single-molecule, single-particle fluorescence spectroscopy.

References

1. Gierschner, J.; Mack, H. G.; Oelkrug, D.; Waldner, I.; Rau, H. *J. Phys. Chem. A* **2004**, *108*, 257-263.
2. Bazan, G. C.; Oldham, W. J.; Lachicotte, R. J.; Tretiak, S.; Chernyak, V.; Mukamel, S. *J. Am. Chem. Soc.* **1998**, *120*, 9188-9204.
3. Shukla, A. D.; Strawser, D.; Lucassen, A. C. B.; Freeman, D.; Cohen, H.; Jose, D. A.; Das, A.; Evmenenko, G.; Dutta, P.; van der Boom, M. E. *J. Phys. Chem. B* **2004**, *108*, 17505-17511.
4. Eddaoudi, M.; Kim, J.; Rosi, N.; Vodak, D.; Wachter, J.; O'Keeffe, M.; Yaghi, O. M. *Science* **2002**, *295*, 469-472.
5. Férey, G. *Chem. Soc. Rev.* **2008**, *37*, 191-214.
6. Deng, H.; Olson, M. A. ; Stoddart, J. F. ; Yaghi, O. M. *Nature Chemistry* **2010**, *2*, 439-443.
7. Kitagawa, S.; Kitaura, R.; Noro, S. *Angew. Chem. Int. Ed.* **2004**, *43*, 2334-2375.
8. Murray, L. J.; Dincă, M.; Long, J. R. *Chem. Soc. Rev.* **2009**, *38*, 1294-1314.
9. Li, J.-R.; Kuppler, R. J.; Zhou, H.-C. *Chem. Soc. Rev.* **2009**, *38*, 1477-1504.
10. Lee, J. Y.; Farha, O. K.; Roberts, J.; Scheidt, K. A.; Nguyen, S. T.; Hupp, J. T. *Chem. Soc. Rev.* **2009**, *38*, 1450-1459.
11. Czaja, A. U.; Trukhanb, N.; Müller, U. *Chem. Soc. Rev.* **2009**, *38*, 1284-1293.
12. Horcajada, P.; Chalati, T.; Serre, C.; Gillet, B.; Sebrie, C.; Baati, T.; Eubank, J. F.; Heurtaux, D.; Clayette, P.; Kreuz, C.; Chang, J.-S.; Hwang, Y. K.; Marsaud, V.; Bories, P.-N.; Cynober, L.; Gil, S.; Férey, G.; Couvreur, P.; Gref, R. *Nature Materials* **2010**, *9*, 172-178.
13. Jiang, H.-L.; Tatsu, Y.; Lu, Z.-H.; Xu, Q. *J. Am. Chem. Soc.* **2010**, *132*, 5586-5587.

14. Tomic, E. A. *J. Appl. Polym. Sci.* **1965**, 9, 3745-3752.
15. Biondi, C.; Bonamico, M.; Torelli, L.; Vaciago, A. *Chem. Commun.* **1965**, 191-192.
16. Hoskins, B. F.; Robson, R. *J. Am. Chem. Soc.* **1990**, 112, 1546-1554.
17. Yaghi, O. M.; Li, G. Li, H. *Nature* **1995**, 378, 703-706.
18. Li, H.; Eddaoudi, M.; O'Keeffe, M.; Yaghi, O. M. *Nature* **1999**, 402, 276-279.
19. Eddaoudi, M.; Kim, J.; Rosi, N.; Vodak, D.; Wachter, J.; O'Keeffe, M.; Yaghi, O. M. *Science* **2002**, 295, 469-472.
20. Férey, G.; Mellot-Draznieks, C.; Serre, C.; Millange, F.; Dutour, J.; Surble, S.; Margiolaki, I. *Science* **2005**, 309, 2040-2042.
21. Wang, X. W.; Chen, J. Z.; Liu, J. H. *Cryst. Growth Des.* **2007**, 7, 1227-1229.
22. Sun, R.; Li, Y.-Z.; Bai, J. F.; Pan, Y. *Cryst. Growth Des.* **2007**, 7, 890-894.
23. Song, X.-Q.; Liu, W.-S.; Dou, W.; Wang, Y.-W.; Zheng, J.-R.; Zang, Z.-P. *Eur. J. Inorg. Chem.* **2008**, 1901-1912.
24. Frisch, M.; Cahill, C. L. *Dalton Trans.* **2005**, 1518-1523.
25. Gunning, N. S.; Cahill, C. L. *Dalton Trans.* **2005**, 2788-2792.
26. Allendorf, M. D.; Bauer, C. A.; Bhaktaa, R. K.; Houk, R. J. T. *Chem. Soc. Rev.* **2009**, 38, 1330-1352.
27. Chen, B. L.; Yang, Y.; Zapata, Qian, F. G. D.; Luo, Y. S.; Zhang, J. H.; Lobkovsky, E. B. *Inorg. Chem.* **2006**, 45, 8882-8886.
28. McManus, G. J.; Perry, J. J.; Perry, M.; Wagner, B. D.; Zaworotko, M. J. *J. Am. Chem. Soc.* **2007**, 129, 9094-9101.

29. Alvaro, M.; Carbonell, E.; Ferrer, B.; Llabrés i Xamena, F. X.; Garcia, H. *Chem. Eur. J.* **2007**, *13*, 5106-5112.
30. Shera, E. B.; Seitzinger, N. K.; Davis, L. M.; Keller, R. A.; Soper, S. A. *Chem. Phys. Lett.* **1990**, *174*, 553-557.
31. Wöll, D.; Braeken, E.; Deres, A.; De Schryver, F. C.; Uji-I, H.; Hofkens, J. *Chem. Soc. Rev.* **2009**, *38*, 313-328.
32. Cornish, P. V.; Ha, T. *ACS Chem. Biol.* **2007**, *2*, 53-61.
33. Rigler, R.; Elson, E. S. *Fluorescence Correlation Spectroscopy: Theory and Applications*; Springer: Berlin, 2001.

Chapter 1

Photoinduced Charge-Transfer Processes on MOF-5 Nanoparticles

Abstract

Metal-organic frameworks (MOFs), which exhibit large surface area and porosity retention upon solvent removal, have attracted considerable attention due to their elegant topology and potential applications in separation, gas storage, nonlinear optics, and catalysis. We report herein comprehensive studies on the nature of luminescence transitions in MOF-5 nanoparticles, which are referred to as MOF-5_n, and the interfacial charge transfer from the photoexcited MOF-5_n to various organic compounds. The time-resolved diffuse reflectance (TDR) and fluorescence spectroscopies were combined in order to clarify the photoinduced one-electron oxidation processes of organic compounds on the MOF-5_n. First, to identify the nature of the luminescence transitions in MOF-5, the temperature dependences of the spectral characteristics were elucidated and compared with those of ZnO nanoparticles. The quenching of MOF-5 emission by several substrates (S), such as aromatic sulfides and amines, was then investigated using steady-state and time-resolved fluorescence spectroscopies. The one-electron oxidation reaction of S during the 355 nm laser flash photolysis of MOF-5_n in acetonitrile was directly examined using TDR spectroscopy, and it was revealed that MOF-5 has a much higher oxidation reaction efficiency than that of P-25 TiO₂ powder, which is the most common photocatalyst. The experimental data were rationalized in terms of the Marcus theory on the electron transfer reactions. Moreover, the influence of adsorbed water on the reaction processes was examined because the MOF crystal morphology is affected by exposure to water during synthesis or after evacuation. Consequently, the present study provides an excellent opportunity to understand the difference in the photoinduced charge-transfer processes between MOFs and semiconductors.

Introduction

Metal-organic frameworks (MOFs), which exhibit large surface area and porosity retention upon solvent removal, have attracted considerable attention due to their elegant topology and potential applications in separation, gas storage, nonlinear optics, and catalysis.¹⁻⁴ A key issue is the rational design and the precise control of the formation of a particular network through the appropriate choice of the constituent metal and bridging organic linkers. By varying the length of the organic backbone of these ligands, many desired MOFs are successfully built. For instance, a well-known MOF-5, which consists of metal clusters of $\text{Zn}_4\text{O}(\text{CO}_2)_6$ joined by benzene dicarboxylate (BDC) linkers to form an extended 3D simple cubic topology with intersecting pores with a 0.8 nm aperture width and a 1.2 nm pore diameter (Figure 1A), has been frequently considered as a potential target for commercialization.⁵⁻⁷ The highest known surface area of $2900 \text{ m}^2 \text{ g}^{-1}$ should also be responsible for the efficient gas storage and catalytic systems.⁵

In the past few years, theoretical calculations have suggested that MOFs are semiconductors or insulators with band gaps between 1.0 and 5.5 eV, which are mainly determined by the highest occupied molecular orbital (HOMO)-lowest unoccupied molecular orbital (LUMO) gaps of the

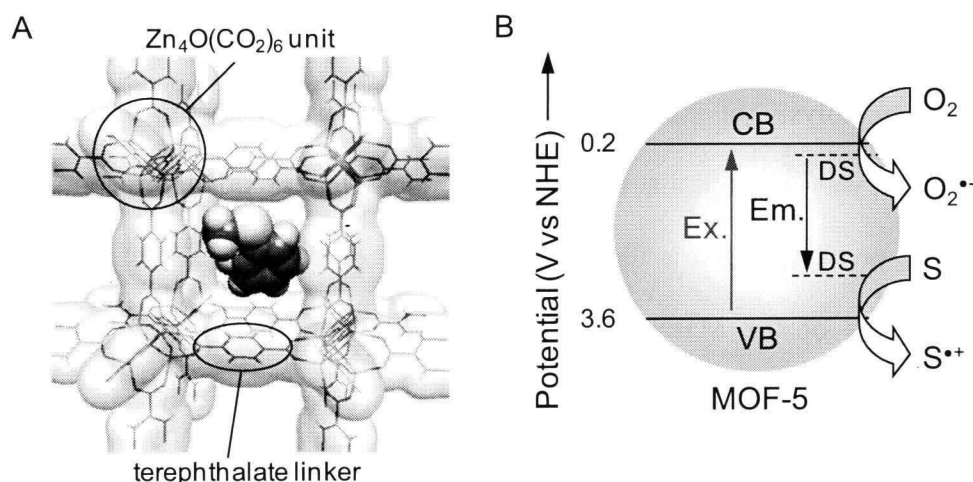


Figure 1. (A) Structure of MOF-5. The octahedral inorganic units are located at the corner of the cell, and the organic units act as linkers. The incorporated thioanisole (TA) in MOF-5 is also shown by the space-filled structure. The image was drawn with the use of MOLEKEL software.¹⁴ (B) The proposed photocatalytic mechanism of MOF-5 nanoparticle. CB is the conduction band, VB is the valence band, and DS is the defect state. Ex and Em indicate the band gap excitation and defect emission, respectively.

linker molecules.⁸⁻¹⁰ The overall electronic properties of MOFs are basically characterized by Zn₄O clusters that bring the systems to the character of a wide band gap semiconductor, ZnO. Because the highest occupied valence bands (VB) are dominated by the contribution of the *p* atomic orbitals of carbon atoms of the aromatic rings with a small contribution of the carboxylate atoms, the band gaps of these materials should be altered by changing the degree of conjugation in the ligands.

Recently, MOF-5 has been investigated in order to understand its electronic and optical properties.¹¹⁻¹³ Garcia et al. reported that an MOF-5 nanoparticle behaves as a semiconductor upon UV light excitation and undergoes charge separation (electrons, e^- , and holes, h^+) decaying on a microsecond time scale.¹² These charge carriers can oxidize or reduce organic molecules in solution like a photocatalyst (Figure 1B). The actual conduction band (CB) energy was estimated to be +0.2 V versus NHE with a band gap of 3.4 eV.¹² However, it has not been fully understood how the photogenerated charge carriers are generated in the MOF materials, how they migrate to the surface (defect states), and how they oxidize or reduce the adsorbates. When trying to answer these basic questions, it is helpful to trace the dynamic behavior of the charge carriers using direct time-resolved spectroscopic measurements. Further understanding of the photoinduced redox processes of organic compounds on the MOFs should lead to novel developments of efficient catalytic systems specific to particular chemical species. Moreover, it is worthwhile to characterize the essential difference in the interfacial charge transfer dynamics between MOFs and semiconductors.

We report herein comprehensive studies on the interfacial charge transfer from the photoexcited MOF-5 nanoparticle (MOF-5_n) to various organic compounds. The time-resolved diffuse reflectance (TDR) and fluorescence spectroscopies were combined in order to clarify the photoinduced one-electron oxidation processes of organic compounds on the MOF-5_n. The TDR spectroscopy is a powerful tool for the investigation of photocatalysis under various conditions.¹⁵⁻²¹ We first examined the temperature dependence of spectral characteristics of the MOF-5 emission and identified the nature of transitions by a comparison with ZnO nanoparticles. We then investigated the quenching of MOF-5 emission by several substrates (S), such as aromatic sulfides

and amines, using steady-state and time-resolved fluorescence spectroscopies in order to confirm whether the photochemical reactions occur by the excitation of MOF-5. In particular, aromatic sulfides were chosen as one S for the TDR measurements, because of their importance in many chemical processes including those of organic synthesis, environmental, and biological significance^{22,23} and the specific spectroscopic properties of S and their radical cations ($S^{\bullet+}$),²⁴⁻²⁶ which have negligible absorption at 355 nm as the excitation wavelength for MOF-5 and absorption in the visible region (around 400-600 nm), respectively. Furthermore, it was recently demonstrated that MOF is capable of mediating highly size- and chemoselective catalytic oxidation of thioethers to sulfoxides by urea hydroperoxide or H_2O_2 .^{27,28}

The one-electron oxidation reaction of S during the 355 nm laser flash photolysis of MOF-5_n in acetonitrile was directly examined using TDR spectroscopy, and the reaction efficiency obtained for MOF-5 was compared to that of P-25 TiO_2 powder,^{20,21,29} which is the most common photocatalyst. The experimental data were rationalized in terms of the Marcus theory on the electron transfer reactions.³⁰ We also clarified the influence of adsorbed water on the reaction processes because the MOF crystal morphology is affected by exposure to water during synthesis or after evacuation.³¹⁻³⁴ Consequently, the present study provides an excellent opportunity to understand the difference in the photoinduced charge transfer processes between MOFs and semiconductors.

Experimental Section

Materials.

MOF-5 nanoparticles were synthesized according to the procedures reported by Huang et al.³² and Garcia et al.¹² by precipitating a mixture of two *N,N*-dimethylformamide (DMF) solutions (40 mL) with triethylamine (TEA) (16 mmol) at room temperature, one of them containing $Zn(NO_3)_2 \cdot 6H_2O$ (4 mmol) and the other consisting of a solution of terephthalic acid (2 mmol). The mixture was allowed to stand for 2 h at room temperature, and the resulting solid was filtered and exhaustively washed with chloroform to remove DMF before drying in an oven for 12 h at 363 K. The resulting powder is denoted as MOF-5_n in this text. The MOF-5_n powder was mixed with

Milli-Q water and then separated by centrifugation (10000 rpm, 10 min) in a high-speed microcentrifuge (Hitachi, himac CF16RX). The resulting powder was dried in a drying oven for 12 h at 363 K (denoted as MOF-5_aq in this text). All chemicals were purchased from commercial sources (Aldrich, Tokyo Chemical Industry, and Nacalai Tesque) in the highest grade available and used without further purification.

ZnO colloidal suspension was synthesized by directly mixing zinc acetate ($\text{Zn}(\text{Ac})_2 \cdot 2\text{H}_2\text{O}$, Aldrich) and lithium hydroxide ($\text{Li}(\text{OH}) \cdot \text{H}_2\text{O}$, Wako) in ethanol with sonication for about 15 min at 273 K.^{35,36} Upon the formation of ZnO nanoparticles in the solution, the solvent was subsequently removed using a rotary evaporator. All chemicals were purchased from commercial sources (Aldrich, Wako, and Nacalai Tesque) in the highest grade available and were used without further purification.

The TiO_2 powder (P-25, Japan Aerosil) used in this study is generously provided by the manufacturer. This photocatalyst has a Brunauer-Emmett-Teller (BET) surface area of $50 \text{ m}^2 \text{ g}^{-1}$, a primary particle size of about 20 nm, and a crystal structure of rutile (20%) and anatase (80%).

For the photoluminescence (PL) quenching measurements, several aromatic sulfides and aliphatic and aromatic amines were used as quenchers. Thioanisole (TA), *p*-methylthioanisole (TA-Me), methoxythioanisole (TA-OMe), and *p*-chlorothioanisole (TA-Cl) were purchased from Tokyo Chemical Industry and were used without further purification. 4-(Methylthio)phenylmethanol (TA- CH_2OH , Aldrich), 1,4-phenylenediamine (PDA, Aldrich), and *N,N,N',N'*-tetramethyl-*p*-phenylenediamine (TMPD, Aldrich) were purified by vacuum sublimation before use. 4-(Methylthio)phenylacetic acid (TA-AcOH, Tokyo Chemical Industry) was recrystallized from ethanol. Phenothiazine (Ptz, Tokyo Chemical Industry) was recrystallized from toluene. 4-Phenylbenzoic acid (PBA, Tokyo Chemical Industry) was recrystallized from ethanol. Aniline (Nacalai Tesque), TEA (Nacalai Tesque), triethanolamine (TEOA, Nacalai Tesque), 1,4-diazabicyclo[2.2.2]octane (DABCO, Aldrich), sodium azide (NaN_3 , Nacalai Tesque), and trichloroacetonitrile (TCA, Tokyo Chemical Industry) were used without further purification. Fresh acetonitrile (CH_3CN , Nacalai Tesque) was used as the solvent.

For the PL and time-resolved diffuse reflectance (TDR) measurements, sample suspensions containing the powders (30 or 5 mg per 1 mL of solvent) were prepared and sonicated for 15 min. The slurries in 1 mm optical cells were maintained in dark at room temperature until used.

Characterizations.

To confirm the crystal phase, morphology, and lattice pattern of the prepared nanoparticles, X-ray diffraction (XRD) and TEM measurements have been performed using a Rigaku RINT2500 XRD spectrometer using a Cu K α source and a Hitachi H-9000 instrument equipped with a tilting device operated at 300 kV, respectively. Steady-state UV-visible absorption and diffuse reflectance spectra were measured by UV-visible-NIR spectrophotometers (Shimadzu, UV-3100, and Jasco, V-570, respectively). Reflectance data were transformed into a Kubelka-Munk function. Steady-state PL spectra were measured by a Hitachi 850 fluorescence spectrophotometer. The sample temperature was controlled with a liquid nitrogen optical cryostat (Oxford Instruments, DN1704) and a temperature controller (Oxford Instruments, IC4) in a temperature range between 110 and 302 K. Fourier transform infrared (FTIR) spectra were recorded on a Jasco 4100 FTIR spectrophotometer equipped with an attenuated total reflectance (ATR) accessory.

Time-resolved Emission Measurements.

The emission lifetime measurements were performed using the third harmonic generation (355 nm, 5 ns full width at half maximum) from a Q-switched Nd³⁺/YAG laser (Continuum, Surelite II-10) for the excitation operated by temporal control using a delay generator (Stanford Research Systems, DG535). The photoluminescence (PL) was collected by a focusing lens and directed through a grating monochromator (Nikon, G250) to a silicon avalanche photodiode detector (Hamamatsu Photonics, S5343). The transient signals were recorded by a digitizer (Tektronix, TDS 580D). The reported signals are the averages of 200 or 300 events. The sample temperature was controlled by circulating a mixture of ethylene glycol and water at a desired temperature around a custom-made cell holder and was measured by a thermocouple probe.

The time-resolved emission spectra and decays in the nanosecond regime were measured by the single photon counting method using a streak scope (Hamamatsu Photonics, C4334-01) equipped

with a polychromator (Acton Research, SpectraPro150). An ultrashort laser pulse was generated with a Ti/sapphire laser (Spectra-Physics, Tsunami 3941 M1BB, fwhm 100 fs) pumped with a diode-pumped solid-state laser (Spectra-Physics, Millennia VIIIs). For excitation of the sample, the output of the Ti/sapphire laser was converted to THG (300 nm) with a harmonic generator (Spectra-Physics, GWU-23FL).

The decay curves were fitted using a nonlinear least-squares method with a multicomponent decay law given by $I(t) = a_1 \exp(-t/\tau_1) + a_2 \exp(-t/\tau_2) + \dots + a_n \exp(-t/\tau_n)$. The average lifetime $\langle \tau \rangle$ was then determined using the equation: $\langle \tau \rangle = \frac{\sum_{i=1}^{i=n} a_i \tau_i^2}{\sum_{i=1}^{i=n} a_i \tau_i}$.

Time-resolved Diffuse Reflectance (TDR) Measurements.

The TDR measurements were performed using the third harmonic generation (355 nm, 5ns fwhm) from a Q-switched Nd³⁺/YAG laser (Continuum, Surelite II-10) for the excitation operated by temporal control using a delay generator (Stanford Research Systems, DG535). The reflected analyzing light from a pulsed 450 W Xe-arc lamp (Ushio, UXL-451-0) was collected by a focusing lens and directed through a grating monochromator (Nikon, G250) to a silicon avalanche photodiode detector (Hamamatsu Photonics, S5343). The transient signals were recorded by a digitizer (Tektronix, TDS 580D). The reported signals are the averages of 30-100 events. The percent absorption (% Abs) is determined using the equation: % Abs = $(R_0 - R)/R_0 \times 100$,^{15,18} where R and R_0 represent the intensities of the diffuse reflected monitor light with and without excitation, respectively.

Results and Discussion

Steady-state Spectral Measurements of MOF-5_n and MOF-5_aq Powders.

MOF-5_n has been characterized by X-ray diffraction (XRD), TEM measurements. The powder XRD patterns were identical to those reported elsewhere (Figure 2).³² Typical diameters of MOF-5_n and MOF-5_aq were determined to be 40 and 150 nm, respectively, based on TEM analysis (Figure 3). The other hands, TEM image and diffraction pattern of ZnO nanoparticles were shown in Figure 4. The average diameter is determined to be around 4 nm. ATR-FTIR spectra of MOF-5_n and MOF-5_aq are displayed in Figure 5. The FTIR spectrum shows vibrational bands between 1560 cm^{-1} and 1376 cm^{-1} characteristic for the asymmetric and symmetric stretching

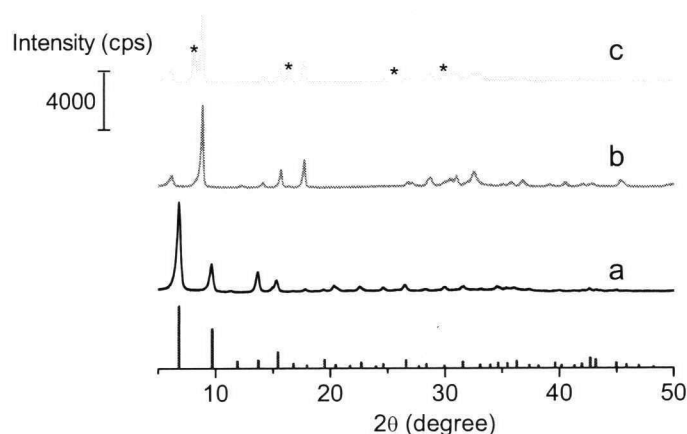


Figure 2. Powder XRD patterns obtained for freshly prepared MOF-5 nanoparticles (MOF-5_n) (a), MOF-5_n exposed to ambient atmosphere for a couple of days (b), and water-treated MOF-5_n (MOF-5_aq) (c). Asterisks indicate new peaks after water treatment. The bars are the XRD pattern for MOF-5.³²

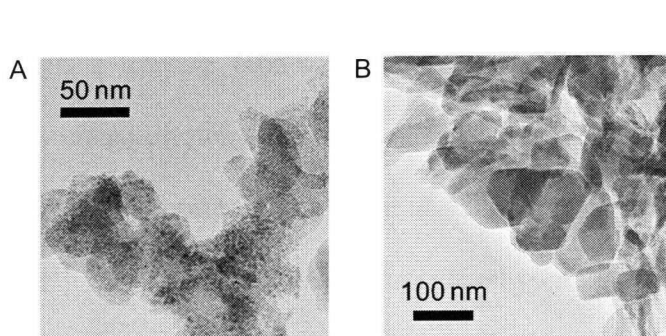


Figure 3. TEM images of MOF-5 nanoparticle (MOF-5_n, A) and water-treated MOF-5_n (MOF-5_aq, B).

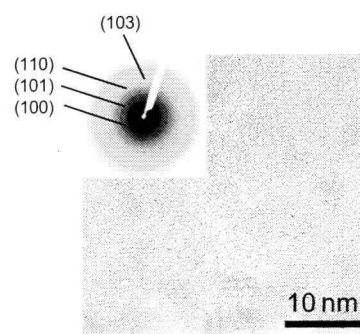


Figure 4. TEM image of ZnO nanoparticles. Inset shows the diffraction pattern.

vibration of the carboxylic groups of the benzene dicarboxylate coordinated to a metal centre. The bands of MOF-5_aq in the region of 3500-3200 cm^{-1} are in agreement with the framework structure of adsorbed water.

The steady-state diffuse reflectance, photoluminescence (PL), and PL excitation spectra of the MOF-5_n powder are shown in Figure 6 (solid lines). A strong green emission at around 535 nm (ca. 2.3 eV) was observed by the excitation at 350 nm for MOF-5_n powder under ambient atmosphere or in acetonitrile. The excitation spectrum measured at fixed emission wavelength of 535 nm is similar to the absorption band at around 350 nm. The biexponential curve fitting of the temporal profile of the emission gives an average τ_0 ($<\tau_0>$) of about 1 μs for dry powder (data not shown). In previous

work, it was suggested that the green emission of MOF-5_n originated from the photoinduced electron transfer from the terephthalate antenna to the Zn_4O_{13} cluster.¹¹ The observed green emission is quite similar to that for ZnO nanocrystals.³⁵⁻⁴⁷ As is well-known, ZnO nanocrystals exhibit a strong emission in the visible with a maximum at around 510-530 nm, which likely originates from surface defects, such as ionizable oxygen vacancies (V_O^0 , V_O^+ , etc.)^{42,43} or zinc vacancies (V_Zn^- , V_Zn^{2-} , etc.)^{47,48} on the surface, although the structure and origin of these surface defects all remain speculative. A key piece of data is given in the next section, which deals with the

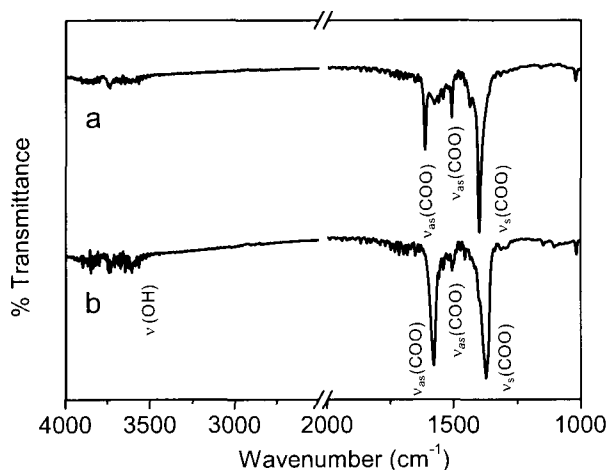


Figure 5. ATR-FTIR spectra of MOF-5_n (a) and MOF-5_aq (b) powders.³²

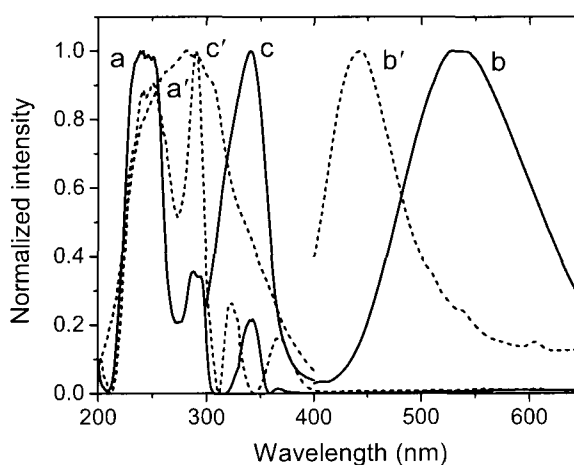


Figure 6. Steady-state diffuse reflectance (a and a'), emission (b and b'), and excitation (c and c') spectra of MOF-5_n (solid lines) and MOF-5_aq (broken lines) powders in ambient atmosphere.

nature of luminescence transitions in MOF-5 and ZnO nanoparticles.

Temperature Dependences of PL Characteristics: Comparison with ZnO Nanoparticles.

Figures 7A and 7B show the PL spectra of MOF-5_n and ZnO powders, respectively, under N₂ atmosphere at different temperatures. In general, a shorter PL lifetime at high temperatures becomes longer at lower temperatures due to nonradiative decay paths that require thermal activation. On the basis of a one-step quenching model, the temperature dependence of the PL intensity can be expressed by the following equation,^{49,50}

$$I_{PL}(T) = I_{PL}(0) / (1 + A \cdot \exp(-E_a / k_B T)) \quad (1)$$

where I_{PL} is the PL intensity, A is a constant, k_B is Boltzmann's constant, T is the absolute temperature, and E_a acts as a fitting parameter that can be obtained from the experimental curve.

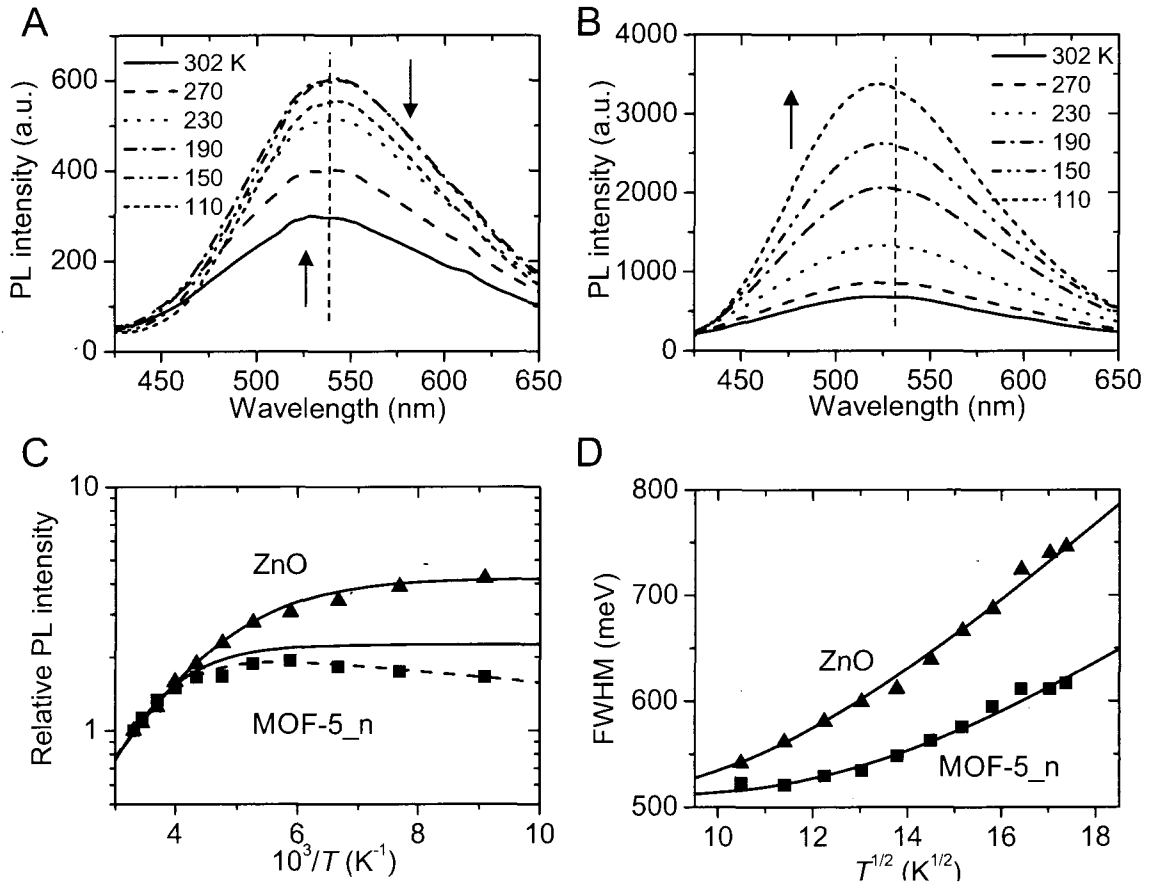


Figure 7. PL spectra of MOF-5_n (A) and ZnO (B) powders under N₂ atmosphere at different temperatures. Temperature dependences of the relative PL intensity (C) and fwhm (D) observed for MOF-5_n (squares) and ZnO (triangles) powders. The error is within $\pm 10\%$. The solid and broken lines in panel C are best fits using eqs 1 and 2, respectively. The solid lines in panel D are best fits using eq 3.

From the fitting result, as shown in Figure 7C, the E_a value is determined to be 80 meV for ZnO, which is larger than that (40 ± 10 meV) calculated using Dijken's data⁴² obtained for a suspension of nanocrystalline ZnO particles in ethanol and eq 1. At the present time, a quantitative comparison is difficult because the experimental conditions (e.g., temperature range and excitation power density) and sample properties (e.g., particle size) are quite different. However, we interpret this energy as the energy required to release minority carriers (electrons) from the vicinity of defect sites, most probably, oxygen vacancies, V_O^0 and V_O^+ , which are located at 50 and 190 meV below the CB edge, respectively,⁴⁷ responsible for the green emission.

On the other hand, interestingly, the PL intensity of MOF-5_n increases at temperatures of 110-170 K and then decreases at temperatures above 170 K. Such temperature dependence of the PL intensity can be described by the following equation,⁵¹

$$I_{PL}(T) = I_{PL}(0) / (1 + A \cdot \exp(-E_a / k_B T)) \cdot \exp(-E_c / k_B T) \quad (2)$$

where E_c is the characteristic energy. From the fitting result, the E_a and E_c values are determined to be 120 and 5 meV, respectively (Figure 7C and Table 2). The estimated E_a is 1.5 times that of ZnO, inferring that the thermal-induced detrapping of charges at the defect sites of MOF-5_n requires a larger energy in the change of equilibrium bond lengths.^{42,48} The E_c value of 5 meV is significantly smaller than the energy difference between defects. At this moment, the origin is unclear. To precisely estimate the activation energies for the MOF-5 emission, the spectra must be measured to temperatures much higher (lower) than 300 K (110 K).

It should also be noted that the PL peak shifts toward lower energies with a decrease in temperature accompanied by a remarkable increase in line width for MOF-5_n, whereas those shifts toward higher energies occur with a decrease in temperature for ZnO (Figures 7A and B, see broken lines). Broad absorption and emission spectra of deep defects in semiconductors are generally attributed to a strong electron phonon interaction typical for localized centers. From the viewpoint based on the configuration coordinate (CC) model,⁵²⁻⁵⁵ the tendency observed for MOF-5_n suggests that the transition responsible for the PL takes place between deeply trapped charges

(localized donor and acceptor levels). On the other hand, in the case of ZnO, the recombination from the e^- trapped in somewhat deeper traps to the trapped h^+ (h_{tr}^+) would result in a shift to lower energies of the emission maximum by the thermal activation. Considering the fact that the particle size of MOF-5_n is 10 times that of ZnO (Table 1), the efficient trapping (localization) of charges at defects would be partially due to a large number of defects inside MOF-5_n nanoparticles.

Table 1. Particle Size of MOF-5, TiO₂, and ZnO Powders and Surface Adsorption Properties of TA-AcOH

materials	d , nm	BET surface area, m ² g ⁻¹	K_{ad} , K ⁻¹ ^a	n_s , mol g ⁻¹ ^b
MOF-5_n	40	600 (1.0) ^c	2×10^3	8×10^{-4} (1.0)
MOF-5_aq	150	45 (0.07) ^c	3×10^3	3×10^{-4} (0.4)
TiO ₂	21	50 (0.08) ^c	3×10^4	3×10^{-4} (0.4)
ZnO	4	N/A	N/A	N/A

^a The equilibrium constants of adsorption for TA-AcOH obtained from Langmuir plots. The experimental procedures are described in ref 21. ^b The amount of saturated sites (n_s) for TA-AcOH.

^c Relative values.

Table 2. Fitting Parameters for Temperature Dependences of the PL Intensity (I_{PL}) and Linewidth (FWHM), and the Activation Free Energy Change (ΔG^\ddagger) for the HT to Phenothiazine (Ptz) Observed for MOF-5_n and ZnO Powders

materials	E_a , meV ^a	E_c , meV ^b	FWHM(0), meV ^c	$\hbar\omega_0^c$, meV ^c	ΔG^\ddagger , eV ^d
MOF-5_n	120 ± 15	5 ± 1	510 ± 20	40 ± 10	0.17 ± 0.02
ZnO	80 ± 15	0	510 ± 20	25 ± 10	0.11 ± 0.02

^a See eq 1. ^b See eq 2. ^c See eq 3. ^d See eq 13 and text for details.

According to the one-dimensional CC model,⁵²⁻⁵⁵ the temperature dependence of the fwhm of the PL band is given by eq 3,

$$\text{FWHM}(T) = \text{FWHM}(0) \sqrt{\coth\left(\frac{\hbar\omega_0^e}{2kT}\right)} \quad (3)$$

where \hbar is the Planck's constant divided by 2π and ω_0^e is the phonon frequency in the excited state. We determined the ω_0^e values of 40 and 25 meV for MOF-5_n and ZnO, respectively (Figure 7D and Table 2). Assuming that the numbers of phonons involved in the transitions are the same for both systems, the larger ω_0^e value obtained for MOF-5_n implies a larger internal reorganization energy, when compared with ZnO.

PL Quenching of MOF-5_n: Comparison with ZnO Nanoparticles.

To obtain the quantitative characteristics of the PL quenching process to allow comparison of oxidation efficiency for the different compounds, Stern-Volmer experiments were carried out. In a typical Stern-Volmer experiment, a powder is added into the solutions with various concentrations of S as a quencher, and the decrease in the emission intensity is described by eq 4,

$$\frac{I_0}{I} - 1 = K_{sv}[S] \quad (4)$$

where I_0 is the initial emission intensity without S, I is the emission intensity with added S of concentration $[S]$, and K_{sv} is the Stern-Volmer constant (which equals $k_q^{av} \tau_0$, where k_q^{av} and τ_0 (which equals 0.62 μs for MOF-5_n powder suspended in acetonitrile) are the average quenching rate constant and the lifetime in the absence of S, respectively). The determined k_q^{av} value is much lower than the diffusion-controlled rate, $\sim 10^{10} \text{ M}^{-1}\text{s}^{-1}$, in the bulk solution (see below for details).

As shown in Figure 8, panels A and B, an almost linear relationship between I_0/I and $[S]$ was obtained for TA, whereas a saturation behavior was observed for TA-AcOH (Figure 8, panels C and D). The quenching of MOF-5 emission by S can be analyzed by considering an equilibrium between uncomplexed and complexed nanoparticles with S. Assuming that the quenching of MOF-5 emission occurs only in the associated complex between MOF-5_n and S, the apparent

association constant (K_a) is given by eq 5,

$$\frac{I_0}{I_0 - I} = \frac{I_0}{I_0 - I'} + \frac{I_0}{K_a (I_0 - I') [S]} \quad (5)$$

where I' is the initial emission intensity of the associated complex.^{36,56,57}

As shown in Figure 8D, the straight-line plot of $I_0/(I_0 - I)$ and $1/[S]$ confirms the validity of the equilibrium model, and the K_a value is determined to be $1900 \pm 300 \text{ M}^{-1}$ for TA-AcOH (Table 1).

The determined apparent k_q^{av} values are plotted against the oxidation potential of the quencher (E_{ox}) as shown in Figure 9. The values obtained for ZnO nanoparticle are also plotted for comparison. The k_q^{av} values increased with the decreasing E_{ox} of S, clearly indicating the HT from the photoexcited MOF-5_n or ZnO nanoparticles to S. However, the k_q^{av} values for TA-AcOH and TA-CH₂OH, which are determined from the initial slope of the normal Stern-Volmer and are denoted by open squares, deviate from the tendency obtained for other quenchers (see solid line),

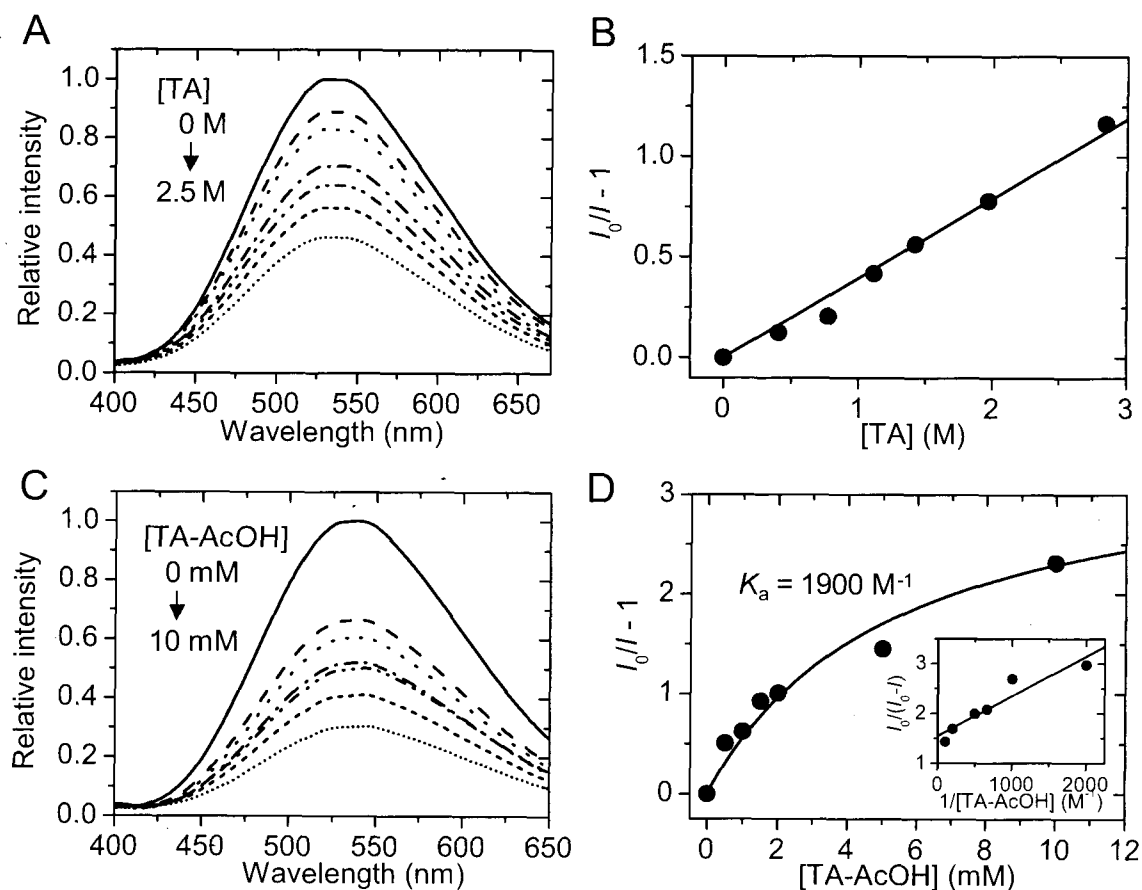


Figure 8. (A) PL spectra of MOF-5_n powder in the absence and presence of TA in acetonitrile. (B) Stern-Volmer plot for TA. (C) PL spectra of MOF-5_n powder in the absence and presence of TA-AcOH in acetonitrile. (D) Stern-Volmer plot for TA-AcOH. Inset indicates the reciprocal plot.

suggesting the adsorption of S on the surface of MOF-5_n by the -COOH or -OH groups. The efficient PL quenching is also observed for 4-phenylbenzoic acid (PBA), which has a high oxidation potential ($E_{ox} = +2.3$ V vs NHE) (see Table 3).⁵⁸

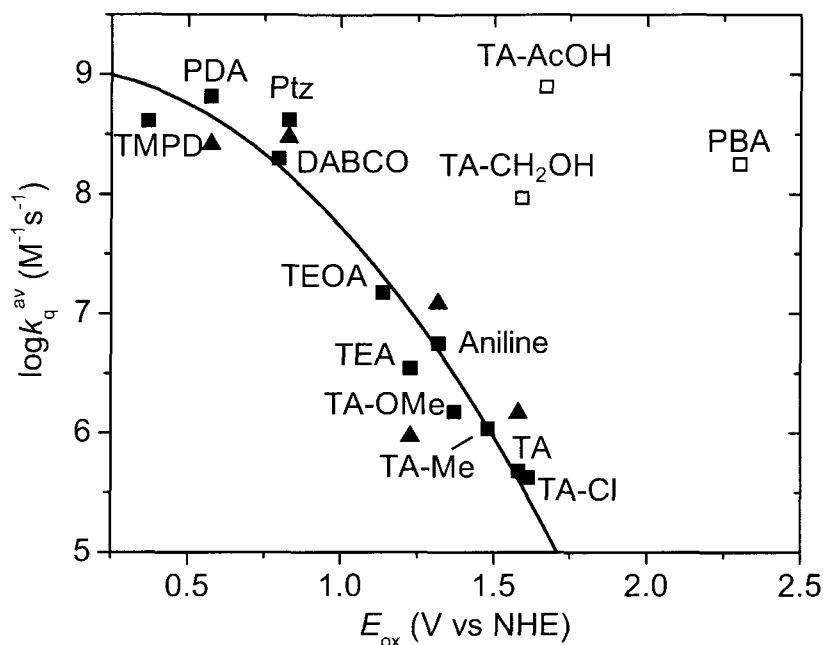


Figure 9. The relationship between E_{ox} and $\log k_q^{av}$ obtained for MOF-5_n (squares) and ZnO (triangles). The open squares, which are obtained for MOF-5_n, significantly deviate from the tendency obtained for other quenchers due to the surface adsorption. The solid line is arbitrary. The k_q^{av} values are summarized in Table 3.

Table 3. Oxidation Potentials of S (E_{ox}) and Average PL Quenching Rate Constants (k_{q}^{av}) Observed for MOF-5_n and ZnO Nanoparticles

S	E_{ox} , V vs NHE	k_{q}^{av} , $\text{M}^{-1} \text{s}^{-1}$ ^g	
		MOF-5_n	ZnO
TMPD	+0.36 ^a	4.1×10^8	N/A
PDA	+0.576 ^b	6.6×10^8	2.6×10^8
DABCO	+0.80 ^b	2.0×10^8	N/A
Ptz	+0.83 ^c	4.2×10^8	3.0×10^8
TEOA	+1.14 ^b	1.5×10^7	N/A
TEA	+1.23 ^b	3.5×10^6	9.3×10^5
Aniline	+1.32 ^b	5.6×10^6	1.2×10^7
TA-OMe	+1.37 ^d	1.5×10^6	N/A
TA-CH ₃	+1.48 ^d	1.1×10^6	N/A
TA	+1.58 ^d	4.8×10^5	1.5×10^6
TA-CH ₂ OH	+1.59 ^e	9.3×10^7	N/A
TA-Cl	+1.61 ^d	4.2×10^5	N/A
TA-AcOH	+1.67 ^e	7.9×10^8	N/A
PBA	+2.3 ^f	1.8×10^8	N/A

^a Reference 59. ^b Reference 60. ^c Reference 61. ^d Reference 62. ^e Reference 20. ^f Reference 58. ^g Error within $\pm 20\%$.

355 nm Laser Flash Photolysis of MOF-5_n Powders.

To confirm the one-oxidation reaction of S, the TDR measurements were performed using a nanosecond pulse laser. Figure 10 A shows the TDR spectra observed after the laser flash during the 355 nm laser photolysis ($3 \pm 0.2 \text{ mJ pulse}^{-1}$) of the MOF-5_n powders slurried in air-saturated acetonitrile. A broad absorption band appeared after the laser flash on MOF-5_n in acetonitrile. The overall spectral shape does not significantly change at a time of over $10 \mu\text{s}$ (the bleaching at around 500-650 nm is due to the emission), and the lifetime reaches $100 \mu\text{s}$ (Figure 10B). A recent transient absorption study revealed that the transient absorption spectrum of the photogenerated e^- appears in the visible and near IR wavelength range.¹² On the basis of the fact that the PL signal decays to almost zero at $5 \mu\text{s}$, the observed transient species is considered to be more deeply trapped charge

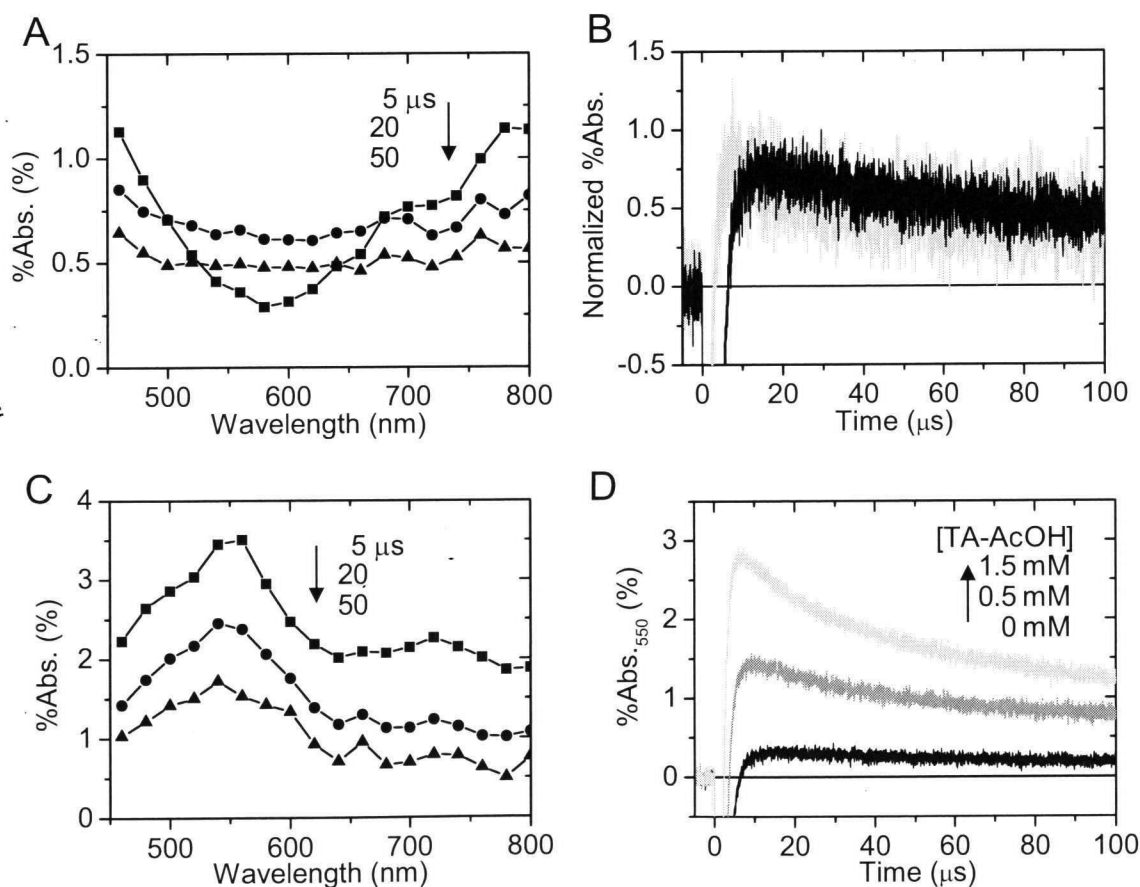


Figure 10. (A) TDR spectra observed at 5, 20, and 50 μs after the laser flash during the 355 nm laser photolysis of the MOF-5_n powder slurried in acetonitrile. (B) Normalized time profiles observed at 550 (black) and 750 (gray) nm. (C) TDR spectra observed during the 355 nm laser photolysis of the MOF-5_n powder slurried in acetonitrile in the presence of TA-AcOH (2 mM). (D) Time profiles observed at 550 nm in the absence and presence of TA-AcOH.

carriers. Because control experiments using Ar or O₂ saturated suspensions showed that oxygen molecules do not react with electrons (e⁻) on a microsecond scale, its only function is to scavenge e⁻ between the consecutive laser shots (10 Hz).

Figure 10C shows the TDR spectra obtained during the laser photolysis of MOF-5_n with the 355 nm light in the presence of TA-AcOH in acetonitrile. The transient absorption band at 450-650 nm immediately appears after the laser flash. The obtained TDR spectra were quite consistent with that attributed to the radical cation of TA-AcOH (TA-AcOH^{•+}),^{20,21} strongly suggesting that the HT from the photoexcited MOF-5_n to the adsorbed TA-AcOH occurs within microseconds after the laser flash. The %Abs' = 0 values increased with the increasing concentration of TA-AcOH, indicating that S⁺ is generated by a bimolecular reaction between the photogenerated species in MOF-5_n and the adsorbed TA-AcOH (Figure 10D).

According to the literature,¹² MOF-5_n generates a valence band hole (h_{VB}⁺) and a conduction band electron (e_{CB}⁻) during the band gap excitation (eq 6).



These photogenerated carriers or trapped carriers (h_{tr}⁺ and e_{tr}⁻, respectively) participate in the redox processes with S at the surface or inside the nanoparticle as described by eq 7.

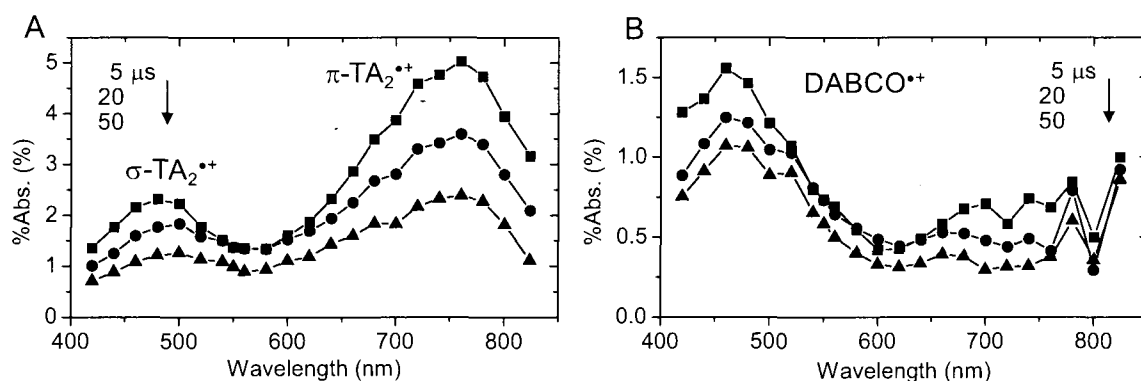
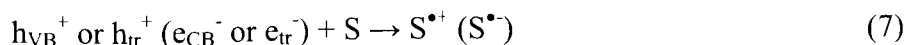


Figure 11. (A) TDR spectra observed at 5, 20, and 50 μs after the laser flash during the 355 nm laser photolysis of the MOF-5_n powder slurried in acetonitrile in the presence of thioanisole (TA) (1.4 M). The σ- and π-type dimer radical cations (TA₂^{•+})²⁵ were observed. (B) TDR spectra observed at 5, 20, and 50 μs after the laser flash during the 355 nm laser photolysis of the MOF-5_n powder slurried in acetonitrile in the presence of DABCO (0.1 M). The DABCO radical cation (DABCO^{•+})⁶³ was observed.



The Marcus theory describes that the free energy change for HT (ΔG_{HT}) from h_{VB}^+ in the MOF-5_n particle to S is simply given by eq 8,^{29,30}

$$\Delta G_{HT} = E_{ox} - E_{VB} \quad (8)$$

where E_{VB} is the potential of the valence band edge. E_{VB} is reported to be +3.6 V vs NHE;¹² therefore, TA-AcOH ($E_{ox} = 1.67$ V vs NHE)²⁰ should be easily oxidized to give its corresponding radical cation. The TDR spectra observed for other compounds, such as TA and DABCO, are given in Figure 11.

One-electron Oxidation Efficiency: Comparison with TiO₂ Nanoparticles.

In the present experiments, it is possible to extract the relative change in the $S^{\bullet+}$ concentration from the initial signal intensity ($\%Abs^{t=0}$) due to the fact that the signal intensity was found to be approximately proportional to the transient concentrations, although we cannot estimate the absolute concentration of $S^{\bullet+}$. Figure 12 shows the relationship between the amount of adsorbates (n_{ad}) and $\%Abs^{t=0}$ obtained for TA-AcOH. The $\%Abs^{t=0}$ values are found to be approximately

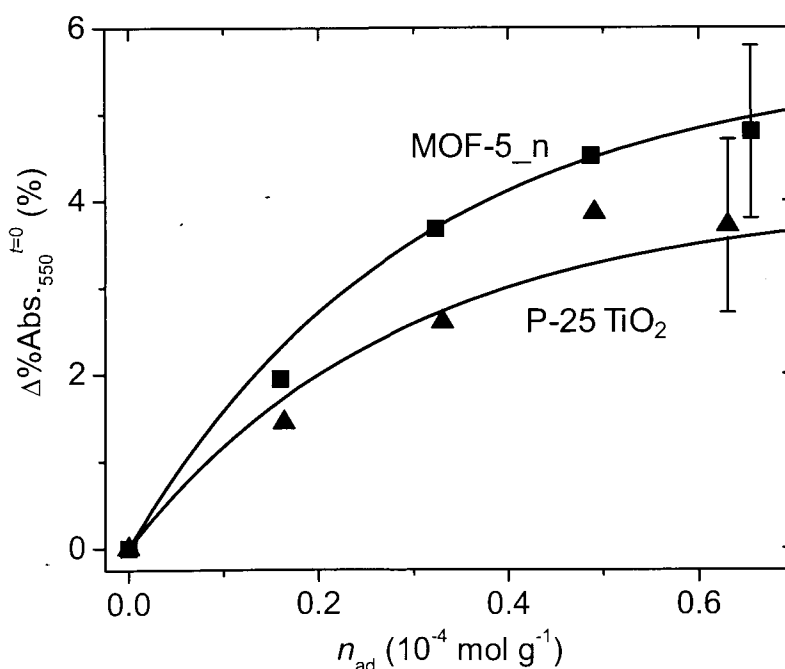


Figure 12. The relationship between the initial transient signal intensity ($\%Abs^{t=0}$) obtained at 550 nm and n_{ad} for TA-AcOH. The lines are arbitrary.

proportional to the n_{ad} values in the present concentrations. It is noteworthy that a relatively high generation yield of radical cations (about 1.3 times) was obtained for MOF-5_n, compared with that for a P-25 TiO₂ photocatalyst, which is the most common photocatalyst.²⁹ Considering that the absorbances at 355 nm are 0.28 and 1.5 for MOF-5_n and P-25 TiO₂ powders in acetonitrile, respectively, the oxidation efficiency, that is, the ratio of the amount of generated radical cations to the absorbed photons, obtained for MOF-5_n is significantly higher than that for P-25 TiO₂. In addition, a longer half-time for charge recombination (over 50 μ s) was observed for MOF-5_n, compared with that for P-25 TiO₂ (about 5 μ s). The observed time profiles cannot fit with a simple single-exponential decay function. For TiO₂ nanoparticles, the nonexponential decay profile of the recombination can be explained using the model of recombination kinetics based on detrapping from deep traps.^{21,64} On the basis of the hypothesis, the observed long half-time for MOF-5_n implies that the charge recombination rate is limited by the motion of electrons in the particles, because TA-AcOH^{•+} is localized at the surface.²¹ Also note that the formation of long-lived intermediates, such as radical cations, should improve the quantum yield for degradation.⁶⁵

Temperature Dependence of Hole Transfer Kinetics.

The temperature-dependent kinetics of electron transfer is characterized in semiclassical Marcus theory with two important parameters: the driving force ($-\Delta G$) and the reorganization energy (λ).³⁰ The activation free energy change (ΔG^\ddagger) involved in the HT was also confirmed for the HT system of MOF-5_n or ZnO and phenothiazine (Ptz) in acetonitrile by the temperature dependence of k_q^{av} (Figure 13, panels A-C). Neglecting the contribution of activation entropy (ΔS^\ddagger), the ΔG^\ddagger values are determined to be 0.17 ± 0.02 and 0.11 ± 0.02 eV for MOF-5_n and ZnO, respectively, from the plots shown in Figure 13D. In the next section, we have discussed the reaction mechanisms in detail.

One-electron Oxidation Mechanisms.

Using steady-state approximation and several assumptions, one can obtain the overall k_q using eq 9,⁶⁶

$$\frac{1}{k_q} = \frac{1}{k_{\text{diff}}} + \frac{1}{k_a} \quad (9)$$

where k_{diff} and k_a are the diffusion- and the activation energy controlled HT reaction rate constants, respectively. The k_a can be calculated using the Jortner and Bixon formalism, which treats the vibrational high-frequency modes quantum mechanically as given by eq 10,^{30,67}

$$k_a = \sqrt{\frac{\pi}{\hbar^2 \lambda_s k_B T}} V(r)^2 \sum_{j_A, j_D} \text{FC}(j_A) \text{FC}(j_D) \times \exp \left\{ -\frac{(\lambda_s + \Delta G_{\text{ET}} + j_D \hbar \nu_D + j_A \hbar \nu_A)^2}{4 \lambda_s k_B T} \right\} \quad (10)$$

where \hbar is Planck's constant divided by 2π , λ_s is the solvent reorganization energy; $j_D \hbar \nu_D$ ($= \lambda_{v,D}$) and $j_A \hbar \nu_A$ ($= \lambda_{v,A}$) are the intramolecular reorganization energies for the hole donor and acceptor, respectively; ΔG_{HT} is the free energy change of the HT reaction; and $V(d)$ is the electronic coupling

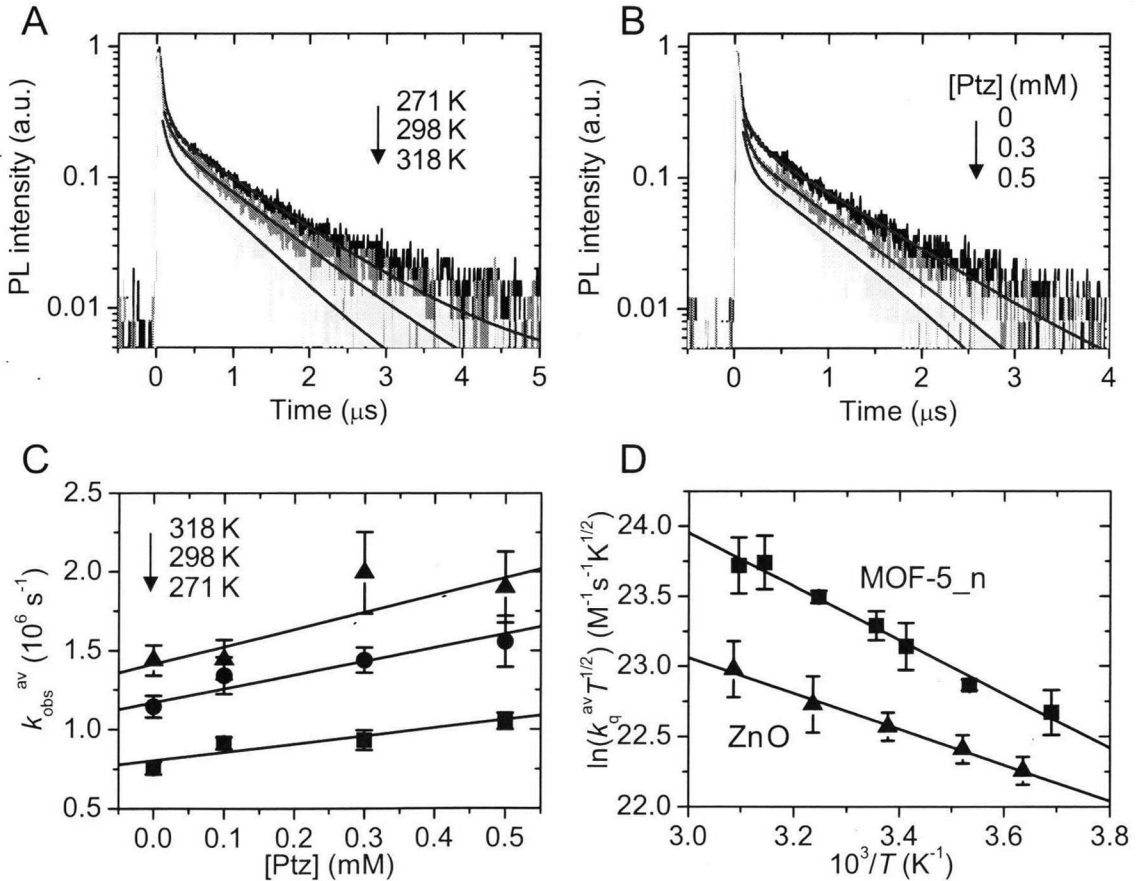


Figure 13. (A) PL decays of MOF-5_n powder in acetonitrile. (B) PL decays of MOF-5_n powder in the absence and presence of Ptz in acetonitrile obtained at 298 K. The lines indicate the results fitted by a biexponential function. (C) Ptz concentration dependence of PL decay rates ($k_{\text{obs}}^{\text{av}}$) observed for the MOF-5_n powder in acetonitrile at different temperatures. (D) Temperature dependence of the PL quenching rates (k_q^{av}) by Ptz obtained for MOF-5_n (squares) and ZnO nanoparticles (triangles).

element between hole donor and acceptor dependent on the distance between these species (d_{DA}) as given by eq 11,⁶⁸

$$V(d_{DA}) = V_0 \exp\left\{-\frac{\beta}{2}(d_{DA} - d_0)\right\} \quad (11)$$

where r_D and r_A are the radii of the hole donor and acceptor, respectively. The permittivity constant of a vacuum and the refractive index and dielectric constant of the solvent are represented by ϵ_0 , n_D , and ϵ , respectively ($n = 1.344$ and $\epsilon = 37.5$ for acetonitrile at 293 K).

With the assumption that two parabolas along a reaction coordinate, which represent the free energy curves of reactant and product states, have the same curvature, the ΔG^\ddagger is given by eq 13.³⁰

$$\Delta G^\ddagger = \frac{(\lambda + \Delta G)^2}{4\lambda} \quad (13)$$

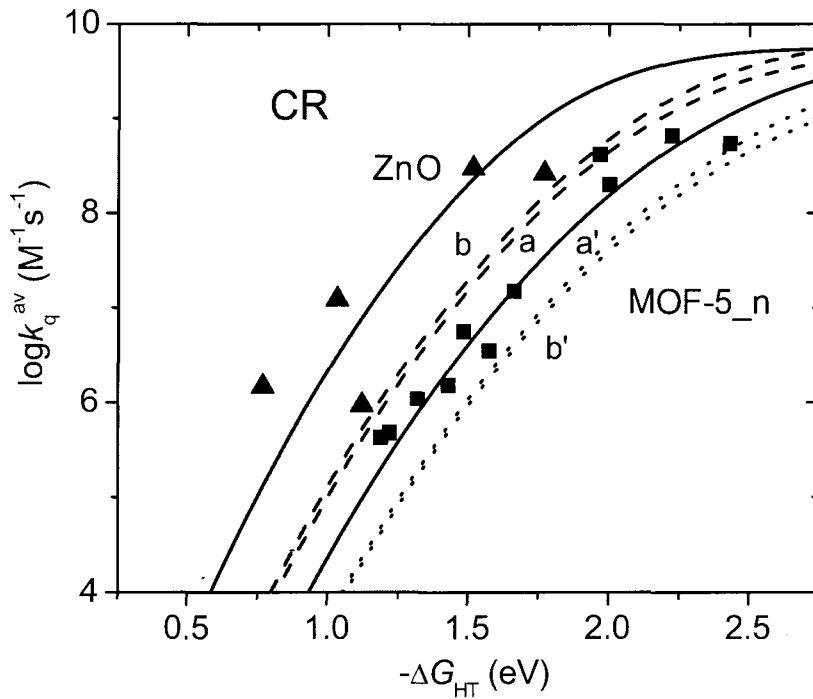


Figure 14. $-\Delta G_{HT}$ dependence of the k_q^{av} rates from the photoexcited MOF-5_n (squares) to S in acetonitrile. The solid line (squares) represents the k_q values calculated with $\lambda_D = 1.2$ eV and $d_{DA} = 1.0$ nm. The broken (a) and dotted (a') lines represent those calculated with $\lambda_D = 0.9$ and 1.5 eV, respectively ($d_{DA} = 1.0$ nm). The broken (b) and dotted (b') lines represent those calculated with $d_{DA} = 0.9$ and 1.1 nm, respectively ($\lambda_D = 1.2$ eV). The k_q^{av} rates from the photoexcited ZnO (triangles) to S in ethanol ($n_D = 1.36$ and $\epsilon = 24.55$) are also shown. The solid line (triangles) represents the k_q values calculated with $\lambda_D = 0.45$ eV and $d_{DA} = 1.0$ nm. The charge recombination (CR) rates would fall in the order of 10^4 s⁻¹ for the MOF-5_n system (gray-colored region).

According to the semiclassical Marcus equation,³⁰ k_a can be described by eq 14.

$$\ln(k_a T^{1/2}) = \ln \left\{ \frac{2\pi^{3/2} |V|^2}{h(\lambda k_B)^{1/2}} \right\} - \frac{\Delta G^\ddagger}{k_B T} \quad (14)$$

In the former section, we determined the ΔG^\ddagger value of 0.17 ± 0.02 eV for the HT system of MOF-5_n and Ptz. Considering the h_{tr}^+ with a potential of +2.8 V versus NHE as a hole donor, we obtain a ΔG value of -1.9 eV for Ptz ($E_{ox} = +0.83$ V vs NHE). Using eqs 10-12 and taking $\lambda_{V,A} = 0.25$ eV for S;⁶⁸⁻⁷⁰ radii of 0.20 and 0.45 nm for the $Zn_4O(CO_2)_6$ cluster (the average Zn-O distance) (r_D)⁷¹ and Ptz (r_A), respectively; and $d_{DA} = 1.0$ nm; we have calculated the λ_S and $\lambda_{V,D}$ values of 2.0 and 1.2 eV, respectively, from the relationship of $\lambda_{total} = \lambda_{V,D} + \lambda_{V,A} + \lambda_S$.

On the other hand, the k_{diff} value is obtained from the Smoluchowski expression as given by eq 15,

$$K_{diff} = 4\pi N(D_D + D_A)d_{DA} \quad (15)$$

where D_D and D_A are the self-diffusion coefficients of the oxidizing species and S, respectively.⁶⁶ In the case of the HT reaction at the MOF-5 surface, because D_D , D_A , we obtained the k_{diff} value of $9 \times 10^9 \text{ M}^{-1}\text{s}^{-1}$ from eq 15. This value is approximately half of that ($2 \times 10^{10} \text{ M}^{-1}\text{s}^{-1}$) calculated for the HT reaction in the bulk acetonitrile solution at room temperature.⁶⁶

Overall, the kinetic data give a reasonable fit to eq 10 with $V_0 = 100 \text{ cm}^{-1}$;⁷² $\beta = 10 \text{ nm}^{-1}$;⁷³ $\lambda_{V,A} (= j_A h \nu_A) = 0.25$ eV for S;⁶⁸⁻⁷⁰ $\lambda_{V,D} (= j_D h \nu_D) = 1.2$ eV; the average frequency ν_A and ν_D of 1500 cm^{-1} , which is typical of carbon-carbon skeletal vibrations and the asymmetric and symmetric modes of carboxylates;^{69,70,74} radii of 0.20 and 0.35 nm for the $Zn_4O(CO_2)_6$ cluster (the average Zn-O distance) (r_D)⁷¹ and S (r_A), respectively; and $d_{DA} = 1.0$ nm, as shown by a solid line in Figure 14. On the other hand, for ZnO nanoparticles, the $-\Delta G_{HT}$ dependence of k_{aq}^{av} is well-reproduced by adapting the h_{tr}^+ with a potential of +2.35 V versus NHE as a hole donor, which is calculated from the E_{VB} of +3.15 V versus NHE^{37,75} and the potential of a trapped site (+0.8 eV above the E_{VB}),⁴⁷ and using the same parameters set for V_0 , β , r_A , r_D , d_{DA} , and $\lambda_{V,A}$, and $\lambda_{V,D} = 0.45$ eV and $\lambda_S = 1.9$ eV. It is noteworthy that the $\lambda_{V,D}$ value for MOF-5_n is significantly higher than those for various

aromatic compounds (0.2-0.3 eV),^{68,69} a hydrated electron (~0 eV),⁷⁶ and a hydroxyl radical (~0 eV).⁷⁶ In addition, the λ_{total} of 3.45 eV is 1.2 times that (2.80 eV) determined for the ZnO system.^{77,78} It seems that the large $\lambda_{\text{V,D}}$ value of the HT process results from a significant structural change in the metal-ligand distances, force constants, and angles of the defects.⁷⁹ Mattesini et al. have used ab initio density function theory to predict the elastic properties of MOF-5 and concluded that MOF-5 is actually not an exceptionally rigid material.⁸⁰ Such flexibility of the MOF structure might induce the collective reorganization process of h^+ -trapping sites in nanoparticles. Meanwhile, for semiconductor nanoparticles, the λ_{S} value would be very low because the solvation process at the surface should be inhibited due to the crystalline structure in which close packed layers of atoms or ions are stacked. On the other hand, in the case of MOF-5_n, the solvent molecules can easily access the vicinity of defect sites located in the interior region and at the surface of the nanoparticles.^{81,82} According to the above calculation and assuming that S^{++} recombines with the e_{tr}^- at the defect state with a potential of around +0.5 to +1.0 V versus NHE^{38,47} and a similar λ_{V} value, the charge recombination (CR) rates would fall in the order of 10^4 s^{-1} for the MOF-5_n/TA-AcOH system (gray-colored region). This might be one of the possible reasons why the lifetime of S^{++} is over 50 μs .⁸³

Influence of Adsorbed Water.

The zinc-based MOFs are water sensitive, losing their high surface area after prolonged exposure to humid atmosphere. Therefore, it is very important to examine the influence of adsorbed water molecules on the interfacial charge transfer processes at the surface of MOF-5 for the technological applications of MOFs.

Meanwhile, water molecules could easily penetrate the pores and disrupt the framework because Zn ions interact with water molecules through nonbonded (electrostatic and van der Waals) interactions.³¹⁻³⁴ Exposure of a freshly prepared sample of MOF-5_n to humid atmosphere for two days resulted in the appearance of new peaks, for example, $2\theta = 8.8^\circ$, in the powder X-ray diffraction pattern, indicating a complete conversion to a second phase (Figure 2).³¹ On other hand, for the water-treated MOF-5_n powder (MOF-5_aq, see Experimental Methods for details),

additional new peaks at $2\theta = 8.1^\circ$ and 16.3° are clearly observed. A significant difference in the particle size and the emission and excitation spectra, compared to those of MOF-5_n, also suggests that the MOF crystal morphology is changed by exposure to water (Figures 3 and 6). By the addition of a small amount of water, the emission is changed to a blue emission at around 440 nm (2.8 eV), and the lifetime is reduced to about 5 ns (Figures 15 and 16). It is considered that the observed blue emission results from the following origins: (1) the surface-state emission (peak wavelength: 430-440 nm) originated from the defects on the particles,⁸⁴ interstitial zinc,⁸⁵ OH- groups at the surface of the particles,⁸⁶ or the interface states related to the surface bonded molecules;⁸⁷⁻⁸⁹ (2) room temperature phosphorescence of terephthalate;⁹⁰ or (3) fluorescence of OH-adducts, that is, 2-hydroxyterephthalate.⁹¹

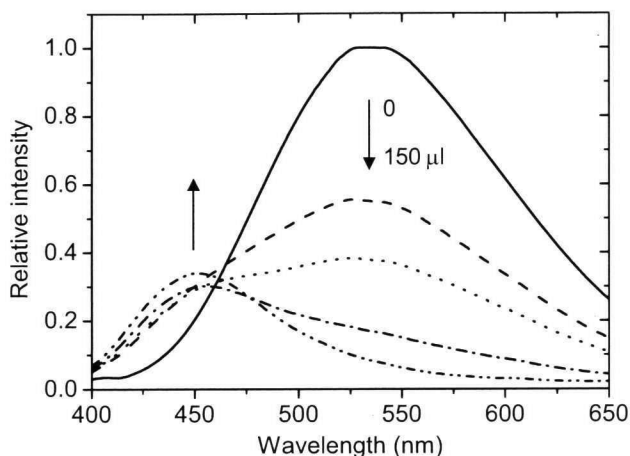


Figure 15. Change of emission spectra of MOF-5_n slurried in acetonitrile (1 mL) by the addition of water.

To confirm the origin of the blue emission, the emission and excitation spectra and lifetimes of terephthalate and 2-hydroxyterephthalate in alkaline water were measured at room temperature. As shown in Figures 17 and 18, the peak wavelengths of 410 and 427 nm and the lifetimes of 8 and 10

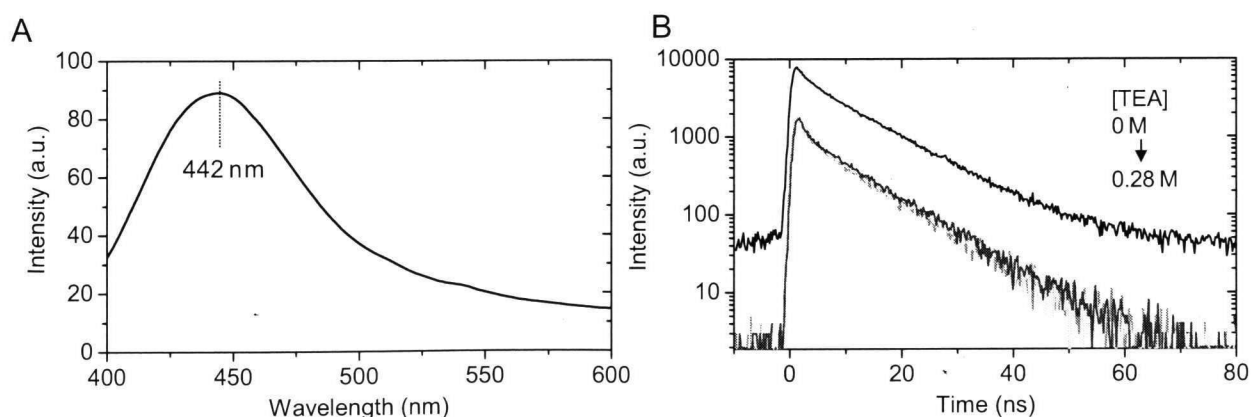


Figure 16. (a) Steady-state PL spectrum of MOF-5_aq in acetonitrile. (b) PL decays obtained for MOF-5_aq in acetonitrile in the absence and presence of TEA.

ns were obtained for terephthalate and 2-hydroxyterephthalate, respectively. The possibility of 2-hydroxyterephthalate would be ruled out by the fact that a high reactivity with TEA as well as the spectral characteristics are quite different from those of the blue emission of MOF-5_aq (Figures 15 and 16). It was also reported that a strong blue emission was observed for ZnO nanoparticles capped with amines, such as diethanolamine.⁸⁹

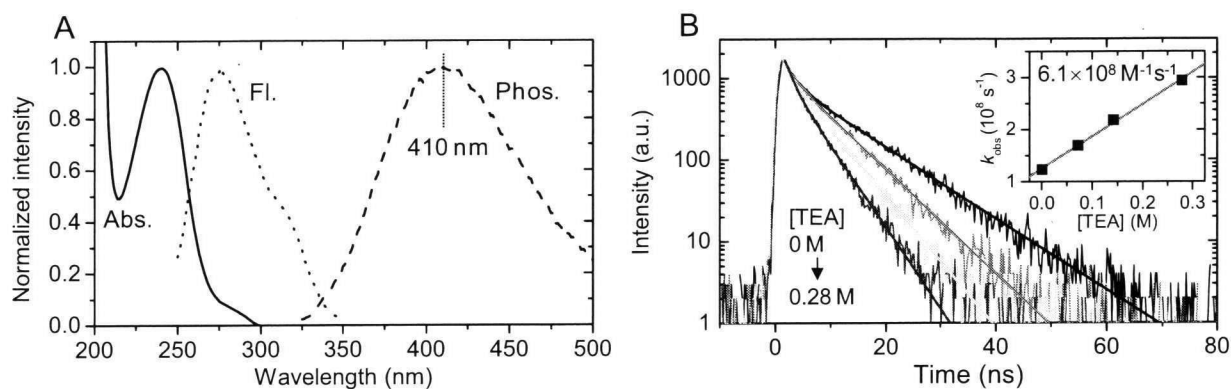


Figure 17. (A) Steady-state absorption, fluorescence, and phosphorescence spectra of terephthalate in alkaline water ([NaOH] = 2 mM). (B) Fluorescence decays obtained for terephthalate in alkaline water ([NaOH] = 2 mM) in the absence and presence of TEA. Inset shows the TEA concentration dependence of the observed decay rates (k_{obs}).

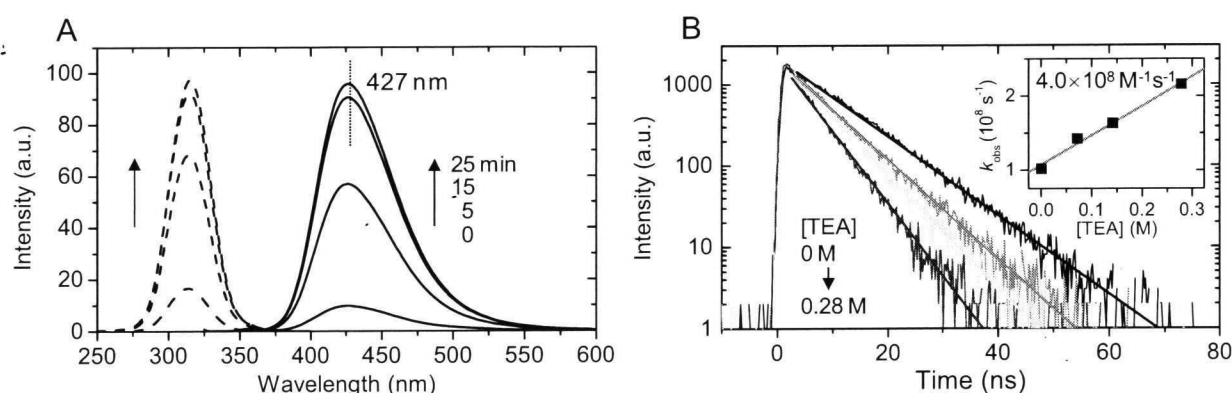


Figure 18. (A) Steady-state fluorescence ($\lambda_{\text{ex}} = 315 \text{ nm}$) and fluorescence excitation ($\lambda_{\text{em}} = 430 \text{ nm}$) spectra of the solution of terephthalate in alkaline water ([NaOH] = 2 mM) before and after UV irradiation. (B) Fluorescence decays obtained for terephthalate in alkaline water after UV irradiation, i.e., 2-hydroxyterephthalate, in the absence and presence of TEA. Inset shows the TEA concentration dependence of the observed decay rates (k_{obs}).

For OH adducts, 2-hydroxyterephthalate seems to be generated from the bimolecular reactions between terephthalate and $\cdot\text{OH}$ radicals, which might be formed during the photoirradiation of MOF-5_aq powder, for example, $h\nu_{\text{VB}}^+ + \text{surface-bound OH}^- \rightarrow \cdot\text{OH}$. However, this possibility is unlikely because no significant increase or blue-shift was observed during the UV irradiation of MOF-5_aq powder (Figure 19). From these findings, we speculate that the blue emission originates from the adsorbate-induced transitions, most probably due to OH^- groups or terephthalic acid (Scheme 1). The MOF-5 structure changes upon addition of water to form a different solid, and

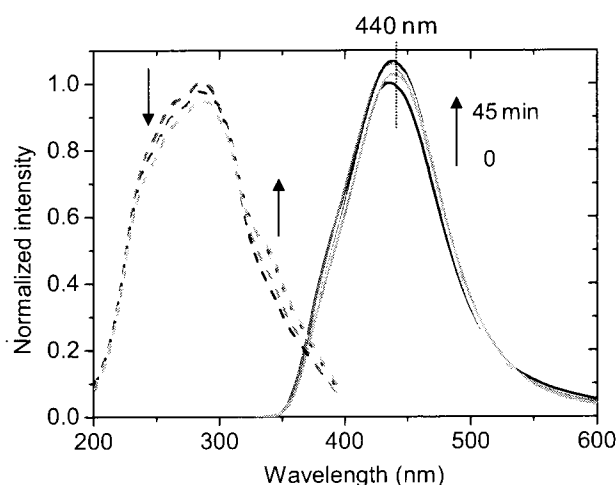
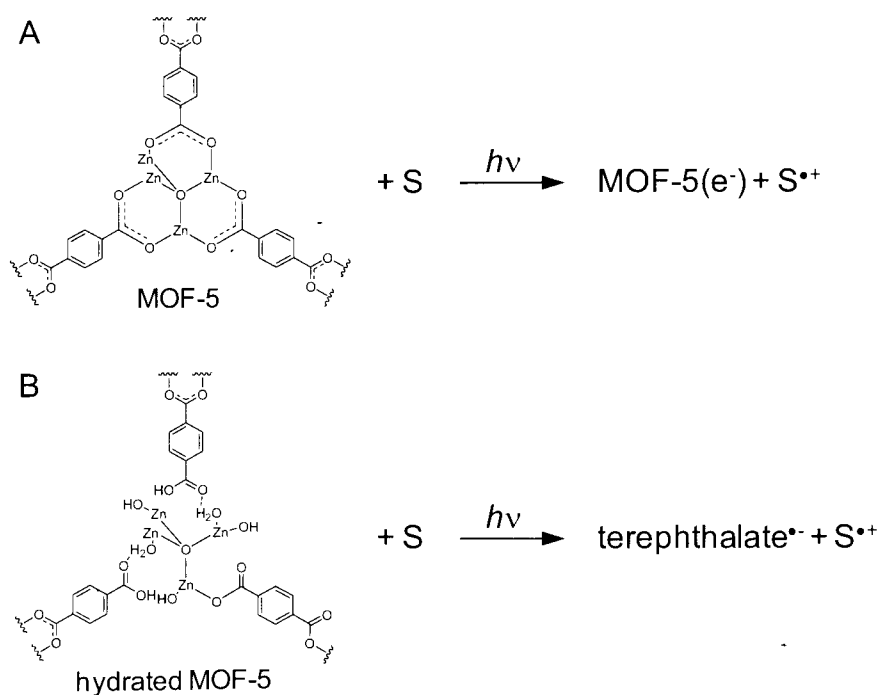


Figure 19. Steady-state PL ($\lambda_{\text{ex}} = 315 \text{ nm}$) and PL excitation ($\lambda_{\text{em}} = 440 \text{ nm}$) spectra of MOF-5_aq powder slurried in acetonitrile before and after UV irradiation.



SCHEME 1: Photoinduced One-Electron Oxidation of S on Unhydrated (A) and Hydrated (B) MOF-5 Nanoparticles

consequently, the photophysical and photochemical properties change.

According to the literature, $(\text{Zn}_4\text{O})(\text{BDC})_3$ is partially decomposed to give the hydrated structure of MOF-5 as given by eq 16.³³

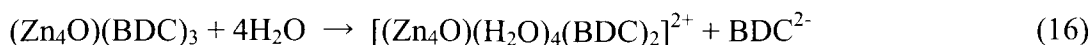


Figure 20A shows the TDR spectra observed after the laser flash during the 355 nm laser photolysis ($3 \pm 0.2 \text{ mJ pulse}^{-1}$) of the MOF-5_aq powder slurried in air-saturated acetonitrile. A strong absorption band with two maxima around 480 and 740 nm was observed, and these peaks decayed with the same kinetics (Figure 20B), although we could not assign these peaks at the present stage.

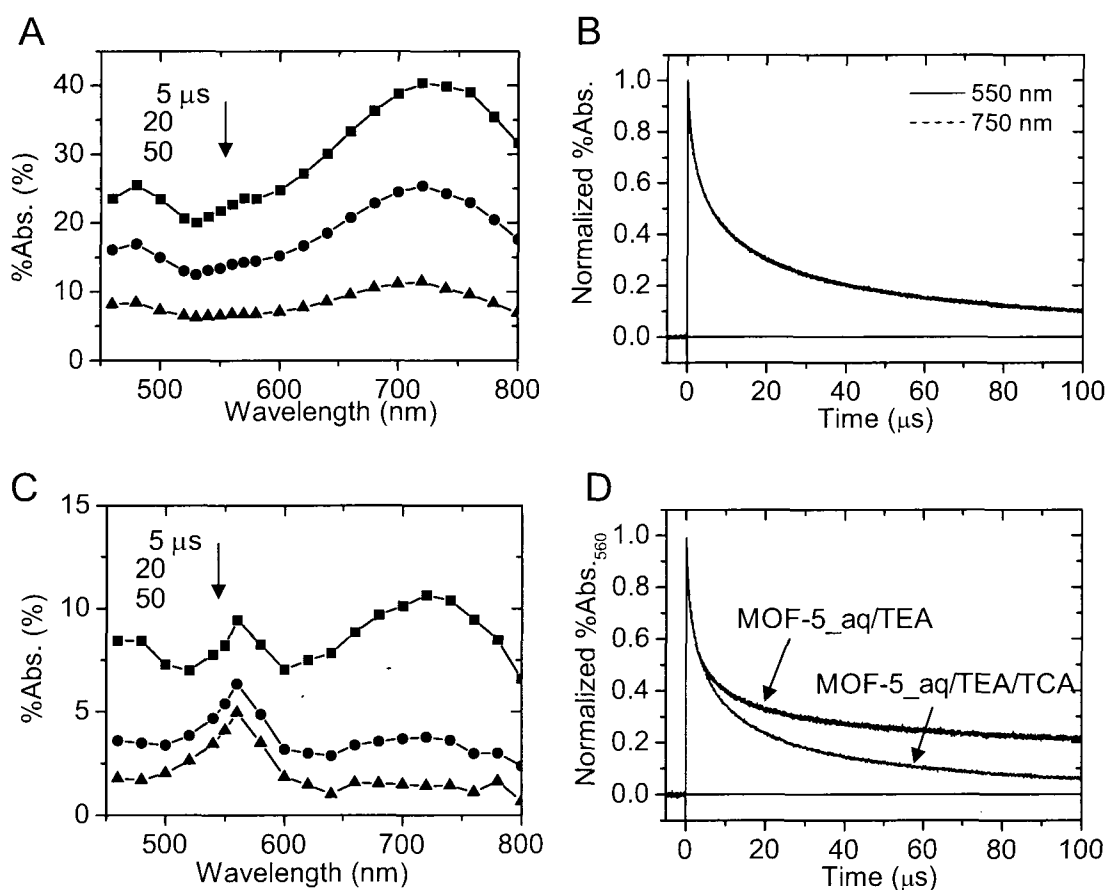


Figure 20. (A) TDR spectra observed at 5, 20, and 50 μs after the laser flash during the 355 nm laser photolysis of the MOF-5_aq powder slurried in acetonitrile. (B) Normalized time profiles observed at 550 (solid line) and 750 (dash line) nm. (C) TDR spectra observed during the 355 nm laser photolysis of the MOF-5_aq powder slurried in acetonitrile in the presence of TEA (0.1 M). (D) Time profiles observed at 560 nm during the 355 nm laser photolysis of the MOF-5_aq powder slurried in acetonitrile in the presence of TEA with and without trichloroacetonitrile (TCA) as an electron scavenger.

To examine the photoinduced charge-transfer reactions, several experiments were performed as follows: (1) the laser flash photolysis of MOF-5_aq in the presence of an electron donor, that is, TEA in acetonitrile, and (2) the laser flash photolysis of MOF-5_n in the presence of an electron acceptor, that is, methyl viologen (MV^{2+}) in water.

Experiment 1 shows an absorption band with a peak at around 550 nm, which could be assigned to the terephthalic acid radical anion,^{92,93} suggesting the electron transfer between the photoexcited MOF-5_aq and TEA. This absorption is efficiently quenched by the addition of TCA (the reduction potential, E_{red} , is -0.09 V vs NHE)⁹⁴ as an electron acceptor. Experiment 2 also shows a broad absorption band with a peak at around 600 nm assigned to $MV^{•+}$,⁹⁵ indicating the electron transfer from the photoexcited MOF-5_aq to MV^{2+} (Figure 21 and ref 12). If terephthalate ion is partially dissociated from the MOF structure by the adsorption of water molecules, the excited triplet state of terephthalate should be involved in the redox reactions with S (Scheme 1). Using the excited triplet energy level of terephthalate, which is estimated to be +3.36 eV from the crossover of the absorption and phosphorescence (Figure 17), the E_{ox} values of +2.17^{96,97} and +1.23 V⁶⁰ for terephthalate and TEA, respectively, the E_{red} values of -1.69⁹⁸ and -0.445 V⁹⁹ for terephthalate and MV^{2+} , respectively (all values vs NHE), and the work term of +0.05 eV,⁷⁸ one can calculate the free energy change for an electron transfer (ΔG_{ET}) of -0.82 and -0.26 eV for the one-electron oxidation and reduction of terephthalate, respectively. Thus, it is energetically possible that the reaction

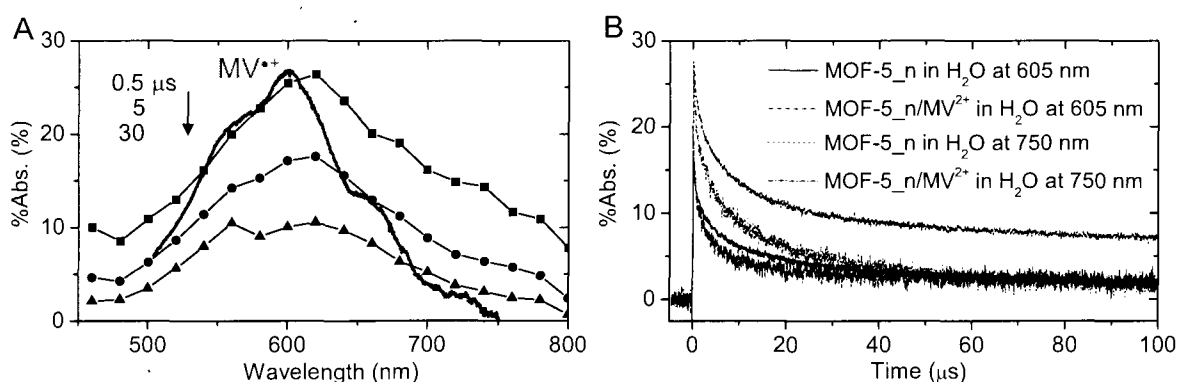


Figure 21. (A) TDR spectra observed at 0.5, 5, and 30 μ s after the laser flash during the 355 nm laser photolysis of the MOF-5_n powder slurried in water (pH 7) in the presence of methyl viologen (MV^{2+}) (10 mM). The solid line indicates the absorption spectrum of $MV^{•+}$ in water.⁹⁵ (B) Time traces observed at 605 and 750 nm in the absence and the presence of MV^{2+} (10 mM).

proceeds to yield the charge separated state.

Conclusions

We have investigated the nature of luminescence transitions in MOF-5 nanoparticles (MOF-5_n) and the interfacial charge transfer from the photoexcited MOF-5_n to the surface adsorbates. Basically, the transition responsible for the green emission of MOF-5 is similar to that of ZnO. However, there are significant differences in the temperature dependences of the PL intensity change and peak-energy shift and in the activation energies for the thermal quenching or activation processes. From the steady-state and time-resolved PL measurements, the bimolecular reaction rates between the photoexcited MOF-5_n and S, such as aromatic sulfides and amines, were determined. The one-electron oxidation reaction of S during the 355 nm laser flash photolysis of MOF-5_n in acetonitrile was directly examined using TDR spectroscopy. The relatively high oxidation efficiency, which is evaluated from the relationship between the amount of adsorbates and the concentration of S^{•+}, was obtained for MOF-5_n, compared with that of the P-25 TiO₂ photocatalyst. It should be noted that S^{•+} generated in the MOF-5 system has a significant long lifetime of over 50 μ s. The long-lived intermediates should enhance the quantum yield for degradation.

The theoretical calculation based on the Marcus theory on the electron transfer reactions revealed that a relatively low HT rate and a long lifetime of S^{•+} obtained for the MOF-5 system are ascribed to the larger λ value ($\lambda_{v,D} = 1.2 \pm 0.3$ eV for the MOF-5_n (h_{tr}⁺)/MOF-5_n couple), contrary to semiconductor nanoparticles, such as ZnO and TiO₂. It is believed that the flexibility of the MOF structure and the accessibility of solvent molecules into the porous structure play important roles in overall reorganization of the charge transfer system.

Moreover, the influence of adsorbed water on the photoinduced reaction processes of MOF-5_n was examined. Although the spectral assignment is incomplete, the electron transfer reactions with S were observed during the 355 nm laser flash photolysis of water-treated MOF-5_n (MOF-5_{aq}) powder in acetonitrile. It was concluded that the excited triplet state of terephthalate, which is dissociated from the MOF structure, is involved in the redox processes.

Our findings provide valuable insights into the charge transfer processes, especially, the one-oxidation reaction of organic compounds, upon the photoexcitation of MOF materials. However, the ultrafast dynamics of charge trapping and transfer at the interface are still unclear.

References and Notes

1. Yaghi, O. M.; O'Keeffe, M.; Ockwig, N. W.; Chae, H. K.; Eddaoudi, M.; Kim, J. *Nature* **2003**, *423*, 705-714.
2. Rowsell, J. L. C.; Yaghi, O. M. *Microporous Mesoporous Mater.* **2004**, *73*, 3-14.
3. Kitagawa, S.; Kitaura, R.; Noro, S. *Angew. Chem. Int. Ed.* **2004**, *43*, 2334-2375.
4. Janiak, C. *Dalton Trans.* **2003**, 2781-2804.
5. Li, H.; Eddaoudi, M.; O'Keeffe, M.; Yaghi, M. *Nature* **1999**, *402*, 276-279.
6. Eddaoudi, M.; Kim, J.; Rosi, N.; Vodak, D.; Wachter, J.; O'Keeffe, M.; Yaghi Omar, M. *Science* **2002**, *295*, 469-472.
7. Rosi, N. L.; Eckert, J.; Eddaoudi, M.; Vodak, D. T.; Kim, J.; O'Keeffe, M.; Yaghi, O. M. *Science* **2003**, *300*, 1127-1130.
8. Fuentes-Cabrera, M.; Nicholson, D. M.; Sumpter, B. G.; Widom, M. *J. Chem. Phys.* **2005**, *123*, 124713/1-124713/5.
9. Civalleri, B.; Napoli, F.; Noel, Y.; Roetti, C.; Dovesi, R. *Cryst Eng Comm* **2006**, *8*, 364-371.
10. Kuc, A.; Enyashin, A.; Seifert, G. *J. Phys. Chem. B* **2007**, *111*, 8179-8186.
11. Bordiga, S.; Lamberti, C.; Ricchiardi, G.; Regli, L.; Bonino, F.; Damin, A.; Lillerud, K. P.; Bjorgen, M.; Zecchina, A. *Chem. Commun.* **2004**, 2300-2301.
12. Alvaro, M.; Carbonell, E.; Ferrer, B.; Llabrés i Xamena, F. X.; Garcia, H. *Chem. -Eur. J.* **2007**, *13*, 5106-5112.

13. Llabrés i Xamena, F.; Corma, A.; Garcia, H. *J. Phys. Chem. C* **2007**, *111*, 80-85.
14. Flukiger, P.; Luthi, H. P.; Portmann, S.; Weber, J. *MOLEKEL* 4.3; Swiss Center for Scientific Computing: Manno, Switzerland, 2000-2002.
15. Kessler, R. W.; Krabichler, G.; Uhl, S.; Oelkrug, D.; Hagan, W. P.; Hyslop, J.; Wilkinson, F. *Opt. Acta* **1983**, *30*, 1099-1111.
16. Draper, R. B.; Fox, M. A. *J. Phys. Chem.* **1990**, *94*, 4628-4634.
17. Draper, R. B.; Fox, M. A. *Langmuir* **1990**, *6*, 1396-1402.
18. Asahi, T.; Furube, A.; Fukumura, H.; Ichikawa, M.; Masuhara, H. *Rev. Sci. Instrum.* **1998**, *69*, 361-371.
19. Tachikawa, T.; Tojo, S.; Fujitsuka, M.; Majima, T. *Langmuir* **2004**, *20*, 2753-2759.
20. Tachikawa, T.; Tojo, S.; Fujitsuka, M.; Majima, T. *J. Phys. Chem. B* **2004**, *108*, 5859-5866.
21. Tachikawa, T.; Yoshida, A.; Tojo, S.; Sugimoto, A.; Fujitsuka, M.; Majima, T. *Chem. -Eur. J.* **2004**, *10*, 5345-5353.
22. Tobien, T.; Cooper, W. J.; Nickelsen, M. G.; Pernas, E.; O'Shea, K. E.; Asmus, K.-D. *Environ. Sci. Technol.* **2000**, *34*, 1286-1291.
23. Ozaki, S.; Ortiz de Montellano, P. R. *J. Am. Chem. Soc.* **1995**, *117*, 7056-7064.
24. Ioele, M.; Steenken, S.; Baciocchi, E. *J. Phys. Chem. A* **1997**, *101*, 2979-2987.
25. Yokoi, H.; Hatta, A.; Ishiguro, K.; Sawaki, Y. *J. Am. Chem. Soc.* **1998**, *120*, 12728-12733.
26. Mohan, H.; Mittal, J. P. *J. Phys. Chem. A* **2002**, *106*, 6574-6580.
27. Dybtsev, D. N.; Nuzhdin, A. L.; Chun, H.; Bryliakov, K. P.; Talsi, E. P.; Fedin, V. P.; Kim, K. *Angew. Chem. Int. Ed.* **2006**, *45*, 916-920.

28. Nuzhdin, A. L.; Dybtsev, D. N.; Bryliakov, K. P.; Talsi, E. P.; Fedin, V. P. *J. Am. Chem. Soc.* **2007**, *129*, 12958-12959.
29. Tachikawa, T.; Fujitsuka, M.; Majima, T. *J. Phys. Chem. C* **2007**, *111*, 5259-5275.
30. Marcus, R. A.; Sutin, N. *Biochim. Biophys. Acta* **1985**, *811*, 265-322.
31. Kaye, S. S.; Dailly, A.; Yaghi, O. M.; Long, J. R. *J. Am. Chem. Soc.* **2007**, *129*, 14176-14177.
32. Huang, L.; Wang, H.; Chen, J.; Wang, Z.; Sun, J.; Zhao, D.; Yan, Y. *Microporous Mesoporous Mater.* **2003**, *58*, 105-114.
33. Greathouse, J. A.; Allendorf, M. D. *J. Am. Chem. Soc.* **2006**, *128*, 10678-10679.
34. Ramanan, A.; Whittingham, M. S. *Cryst. Growth Des.* **2006**, *6*, 2419-2421.
35. Spanhel, L.; Anderson, M. A. *J. Am. Chem. Soc.* **1991**, *113*, 2826-2833.
36. Kamat, P. V.; Patrick, B. *J. Phys. Chem.* **1992**, *96*, 6829-6834.
37. Bahnemann, D. W.; Kormann, C.; Hoffmann, M. R. *J. Phys. Chem.* **1987**, *91*, 3789-3798.
38. Djurišić, A. B.; Leung, Y. H. *Small* **2006**, *2*, 944-961.
39. Bohle, D. S.; Spina, C. J. *J. Am. Chem. Soc.* **2007**, *129*, 12380-12381.
40. Lin, Y.; Wang, D.; Zhao, Q.; Li, Z.; Ma, Y.; Yang, M. *Nanotechnology* **2006**, *17*, 2110-2115.
41. Vanheusden, K.; Warren, W. L.; Seager, C. H.; Tallant, D. R.; Voigt, J. A.; Gnade, B. E. *J. Appl. Phys.* **1996**, *79*, 7983-7990.
42. Van Dijken, A.; Meulenkamp, E. A.; Vanmaekelbergh, D.; Meijerink, A. *J. Phys. Chem. B* **2000**, *104*, 1715-1723.
43. van Dijken, A.; Meulenkamp, E. A.; Vanmaekelbergh, D.; Meijerink, A. *J. Phys. Chem. B* **2000**, *104*, 4355-4360.

44. Sakohara, S.; Ishida, M.; Anderson, M. A. *J. Phys. Chem. B* **1992**, *102*, 10169-10175.
45. Norberg, N. S.; Gamelin, D. R. *J. Phys. Chem. B* **2005**, *109*, 20810-20816.
46. Lin, B.; Fu, Z.; Jia, Y. *Appl. Phys. Lett.* **2001**, *79*, 943-945.
47. Egelhaaf, H. J.; Oelkrug, D. *J. Cryst. Growth* **1996**, *161*, 190-194.
48. Janotti, A.; Van de Walle, C. G. *Phys. Rev. B* **2007**, *76*, 165202/1-165202/22.
49. Bimberg, D.; Sondergeld, M.; Grobe, E. *Phys. Rev. B* **1971**, *4*, 3451-3455.
50. Jiang, D. S.; Jung, H.; Ploog, K. *J. Appl. Phys.* **1988**, *64*, 1371-1377.
51. Leroux, M.; Grandjean, N.; Beaumont, B.; Nataf, G.; Semond, F.; Massies, J.; Gibart, P. *J. Appl. Phys.* **1999**, *86*, 3721-3728.
52. Reshchikov, M. A.; Morkoc, H. *J. Appl. Phys.* **2005**, *97*, 061301/1-061301/95.
53. Shionoya, S.; Koda, T.; Era, K.; Fujiwara, H. *J. Phys. Soc. Jpn.* **1964**, *19*, 1157-1167.
54. Ogino, T.; Aoki, M. *Jpn. J. Appl. Phys.* **1980**, *19*, 2395-2405.
55. Reshchikov, M. A.; Shahedipour, F.; Korotkov, R. Y.; Ulmer, M. P.; Wessels, B. W. *Physica B* **1999**, *273-274*, 105-108.
56. Kamat, P. V.; Huehn, R.; Nicolaescu, R. *J. Phys. Chem. B* **2002**, *106*, 788-794.
57. Ramakrishna, G.; Ghosh, H. N. *Langmuir* **2003**, *19*, 3006-3012.
58. Tachikawa, T.; Tojo, S.; Fujitsuka, M.; Majima, T. *Tetrahedron Lett.* **2004**, *45*, 3753-3756.
59. Bock, C. R.; Connor, J. A.; Gutierrez, A. R.; Meyer, T. J.; Whitten, D. G.; Sullivan, B. P.; Nagle, J. K. *J. Am. Chem. Soc.* **1979**, *101*, 4815-4824.
60. Ruiz, G.; Rodriguez-Nieto, F.; Wolcan, E.; Feliz, M. R. *J. Photochem. Photobiol., A* **1997**, *107*, 47-54.

61. Barra, M.; Calabrese, G. S.; Allen, M. T.; Redmond, R. W.; Sinta, R.; Lamola, A. A.; Small, R. D., Jr.; Scaiano, J. C. *Chem. Mater.* **1991**, *3*, 610-616.
62. Fukuzumi, S.; Shimoosako, K.; Suenobu, T.; Watanabe, Y. *J. Am. Chem. Soc.* **2003**, *125*, 9074-9082.
63. Halpern, A. M.; Forsyth, D.A.; Nosowitz, M. *J. Phys. Chem.* **1986**, *90*, 2677-2679.
64. Haque, S. A.; Tachibana, Y.; Willis, R. L.; Moser, J. E.; Grätzel, M.; Klug, D. R.; Durrant, J. R. *J. Phys. Chem. B* **2000**, *104*, 538-547.
65. Tachikawa, T.; Takai, Y.; Tojo, S.; Fujitsuka, M.; Majima, T. *Langmuir* **2006**, *22*, 893-896.
66. Kavarnos, G. J.; Turro, N. J. *Chem. Rev.* **1986**, *86*, 401-449.
67. Bixon, M.; Jortner, J.; Cortes, J.; Heitele, H.; Michel-Beyerle, M. E. *J. Phys. Chem.* **1994**, *98*, 7289-7299.
68. Miller, J. R.; Beitz, J. V.; Huddleston, R. K. *J. Am. Chem. Soc.* **1984**, *106*, 5057-5068.
69. Gould, I. R.; Ege, D.; Moser, J. E.; Farid, S. *J. Am. Chem. Soc.* **1990**, *112*, 4290-4301.
70. Gould, I. R.; Young, R. H.; Moody, R. E.; Farid, S. *J. Phys. Chem.* **1991**, *95*, 2068-2080.
71. Hafizovic, J.; Bjørgen, M.; Olsbye, U.; Dietzel, P. D. C.; Bordiga, S.; Prestipino, C.; Lamberti, C.; Lillerud, K. P. *J. Am. Chem. Soc.* **2007**, *129*, 3612-3620.
72. Tachiya, M.; Murata, S. *J. Phys. Chem.* **1992**, *96*, 8441-8444.
73. Tavernier, H. L.; Kalashnikov, M. M.; Fayer, M. D. *J. Chem. Phys.* **2000**, *113*, 10191-10201.
74. Bordiga, S.; Vitillo, J. G.; Ricchiardi, G.; Regli, L.; Cocina, D.; Zecchina, A.; Arstad, B.; Bjørgen, M.; Hafizovic, J.; Lillerud, K. P. *J. Phys. Chem. B* **2005**, *109*, 18237-18242.
75. Hagfeldt, A.; Grätzel, M. *Chem. Rev.* **1995**, *95*, 49-68.

76. Ichino, T.; Fessenden, R. W. *J. Phys. Chem. A* **2007**, *111*, 2527-2541.
77. A difference in λ_S between acetonitrile and ethanol is estimated to be within 5 % from eq 12. However, the hydrogen bonding between ZnO (h^+ -trapping sites) and ethanol may increase the λ_S value. For instance, the λ_S determined for the radical ion pair systems involving the hydrogen-bonded complexes between the duroquinone anion and alcohol are larger by about 0.2 eV than those calculated from the Marcus continuum dielectric model.⁸⁵
78. Yago, T.; Kobori, Y.; Akiyama, K.; Tero-Kubota, S. *Chem. Phys. Lett.* **2003**, *369*, 49-54.
79. Janotti, A.; Van de Walle, C. G. *Appl. Phys. Lett.* **2005**, *87*, 122102/1-122102/3.
80. Mattesini, M.; Soler, J. M.; Ynduráin, F. *Phys. Rev. B* **2006**, *73*, 094111/1-094111/8.
81. The effective self-diffusion coefficients of organic compounds, such as *n*-hexane and benzene, in the MOF-5 structure are only slightly smaller than their values in the neat liquids at the same temperature.⁸² This also suggests that significant low k_{HT}^{av} values are not explained by considering the suppressed diffusion of S inside MOF-5_n.
82. Stallmach, F.; Gröger, S.; Künzel, V.; Kärger, J.; Yaghi, O. M.; Hesse, M.; Müller, U. *Angew. Chem. Int. Ed.* **2006**, *45*, 2123-2126.
83. Another explanation is that S^{*+} is desorbed from the surface of MOF-5_n due to the electronic repulsion between them. However, this mechanism should be excluded because no significant increase in k_q^{av} was observed for anionic quenchers, such as azide ion (data not shown). In addition, the half time for charge recombination of about 1 μs was obtained for the P-25 TiO₂/TA-CH₂OH system, where TA-CH₂OH has a relatively low K_{ad} value of $\sim 10^2 \text{ M}^{-1}$.²⁰
84. Kahn, M. L.; Cardinal, T.; Bousquet, B.; Monge, M.; Jubera, V.; Chaudret, B. *ChemPhysChem* **2006**, *7*, 2392-2397.
85. Fang, Z.; Wang, Y.; Xu, D.; Tan, Y.; Liu, X. *Opt. Mater.* **2004**, *26*, 239-242.

86. Monticone, S.; Tufeu, R.; Kanaev, A. V. *J. Phys. Chem. B* **1998**, *102*, 2854-2862.
87. Xiong, H.-M.; Liu, D.-P.; Xia, Y.-Y.; Chen, J.-S. *Chem. Mater.* **2005**, *17*, 3062-3064.
88. Xiong, H.-M.; Wang, Z.-D.; Xia, Y.-Y. *Adv. Mater.* **2006**, *18*, 748-751.
89. Fu, Y.-S.; Du, X.-W.; Kulinich, S. A.; Qiu, J.-S.; Qin, W.-J.; Li, R.; Sun, J.; Liu, J. *J. Am. Chem. Soc.* **2007**, *129*, 16029-16033.
90. Ford, C. D.; Hurtubise, R. *J. Anal. Chem.* **1978**, *50*, 610-612.
91. Mason, T. J.; Lorimer, J. P.; Bates, D. M.; Zhao, Y. *Ultrason. Sonochem.* **1994**, *1*, S91-S95.
92. Qin, L.; Tripathi, G. N. R.; Schuler, R. H. *J. Phys. Chem.* **1989**, *93*, 5432-5437.
93. Natarajan, P.; Fessenden, R. W. *J. Phys. Chem.* **1989**, *93*, 6095-6100.
94. Costentin, C.; Robert, M.; Saveant, J.-M. *J. Am. Chem. Soc.* **2003**, *125*, 10729-10739.
95. Das, T. N.; Ghanty, T. K.; Pal, H. *J. Phys. Chem. A* **2003**, *107*, 5998-6006.
96. Jonsson, M.; Lind, J.; Reitberger, T.; Eriksen, T. E.; Merenyi, G. *J. Phys. Chem.* **1993**, *97*, 11278-11282.
97. Hansch, C.; Leo, A.; Taft, R. W. *Chem. Rev.* **1991**, *91*, 165-195.
98. Hall, M. E.; McNutt, R. C. *Anal. Chem.* **1960**, *32*, 1073-1074.
99. Dung, D.; Ramsden, J.; Grätzel, M. *J. Am. Chem. Soc.* **1982**, *104*, 2977-2985.

Chapter 2

Europium-Based Metal-Organic Framework as a Photocatalyst

Abstract

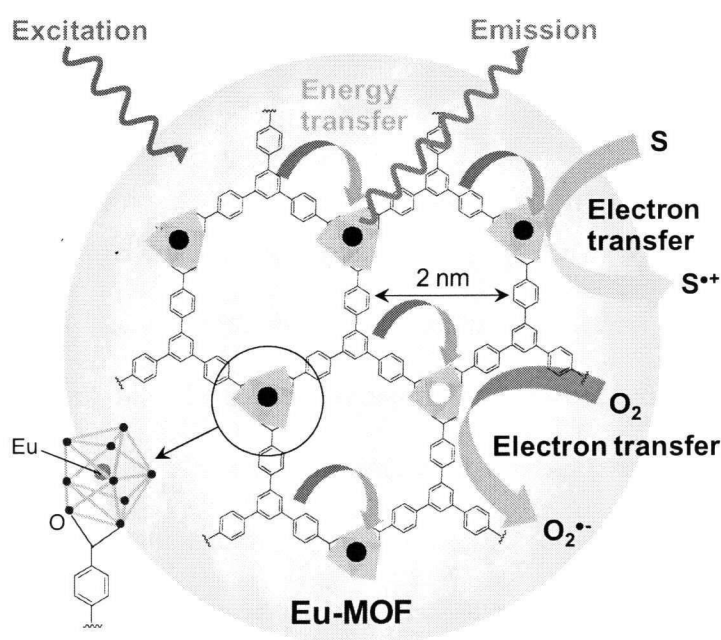
Lanthanide-based metal-organic frameworks (Ln-MOFs) are fascinating because of their versatile coordination geometry, unique luminescent and magnetic properties, and possible high framework stability to water. We synthesized nanosized europium-based MOF (Eu-MOF) particles and investigated the photoinduced electron transfer between the excited Eu-MOF nanoparticles and various organic compounds, such as aromatic sulfides and amines. From the time-resolved emission measurements, the bimolecular quenching rate constants of luminescence from the Eu^{3+} ions in the MOF framework by electron donors were determined and explained in terms of the Marcus theory of electron-transfer reactions. Furthermore, spatially resolved emission quenching images obtained by confocal fluorescence microscopy revealed that small (large) quencher molecules quickly (slowly) and homogeneously (inhomogeneously) penetrate micro-sized Eu-MOF crystals. These observations led us confidently to assume the possibility that Eu-MOFs work as a size-selective photocatalyst for the one-electron oxidation of organic compounds.

Introduction

Metal-organic frameworks (MOFs) have attracted significant research interest because their widely tunable topology makes for numerous applications, such as gas storage, catalysis, separations, drug delivery, and sensors.^{1,2} Compared to classical solid-state catalysts such as zeolites, MOFs with a variety of pore sizes and functions can be easily built by choosing the constituent metals and bridging organic linkers. In addition, upon photoexcitation of organic linkers or metal clusters, MOFs can act as a charge-carrier transporting system.³ On the basis of this concept, we recently investigated the photoinduced charge-transfer process between excited MOF-5 nanoparticles and organic compounds by using time-resolved emission and diffuse reflectance

spectroscopies.⁴ However, the slight exposure of Zn-based MOFs, such as MOF-5, to the ambient atmosphere or residual water in the solvent remarkably lowers their photocatalytic activity because of the destruction of the pore structures.^{4,5} Lanthanide-based metal-organic frameworks (Ln-MOFs), in particular, Tb^{3+} and Eu^{3+} , are fascinating because of their versatile coordination geometry, unique luminescent and magnetic properties, and possible high framework stability to water.^{6,7} Ln-MOFs are also attractive because the organic linker can serve as an antenna that sensitizes the lanthanide emission. Recently, several Ln-MOFs with interesting photophysical properties, of which luminescence is coupled to porosity, have been reported.⁶ Nevertheless, there are no precedent studies to evaluate detailed mechanisms of photophysical and photochemical reactions for Ln-MOFs. A further understanding of the photoinduced redox processes on the Ln-MOFs should lead to novel developments of efficient photocatalytic and photoelectrochemical systems with chemical specificity.

In this chapter, we report systematic studies of interfacial electron transfer between photoexcited europium-based MOF (Eu-MOF) particles and various organic compounds, such as aromatic sulfides and amines, adsorbed on the surface and trapped inside the pores of the MOF structure



SCHEME 1. Proposed Photocatalytic Mechanism of an Eu-MOF Nanoparticle. The Symbols Represent the $[\text{EuO}_9]$ Polyhedra. The Black and White Circles Represent Eu^{3+} and Eu^{2+} Ions. S is the Organic Substrate (Electron Donor).

(Scheme 1). To increase both the surface area and pore volume of MOFs, we choose the 1,3,5-benzenetribenzoate (BTB) ligand as a linker.^{5,8} We also select the Eu^{3+} ion as the constituent metal because Eu^{3+} has a very low reduction potential ($E_{\text{red}} = \text{Eu}^{3+}/\text{Eu}^{2+} = -0.35 \text{ V vs NHE}$)⁹ and the resultant Eu^{2+} ion can be reoxidized to its initial state by various oxidants such as O_2 and H_2O_2 .^{10,11} Time-resolved spectroscopic methods as well as confocal microscopy are utilized to clarify the reaction dynamics of the excited Eu^{3+} ions in the Eu-MOF with the organic compounds.

Experimental Methods

Materials.

Nanosized and micro-sized Eu-MOF were synthesized according to the procedures reported in literature with some modifications.^{5,8} In a typical method for nanosized Eu-MOF synthesis, triethylamine (TEA) (160 μL 1.15 mmol, Aldrich,) was very slowly added to 40 mL methanol (Nacalai Tesque) solution containing $\text{Eu}(\text{NO}_3)_3 \cdot 5\text{H}_2\text{O}$ (0.2 g, 0.47 mmol, Aldrich) and 1,3,5-tris(4-carboxyphenyl)benzene (H_3BTB , 0.2 g, 0.46 mmol, Tokyo Chemical Industry). The mixture was allowed to stand for 2 h at room temperature, and precipitated solid product was collected by centrifugation, washed six times with methanol, and then dried in an oven for 12 h at 363 K.

Micro-sized Eu-MOF was synthesized by the following procedure.⁸ Fer y group already reported its synthesis and named it as MOF, MIL-103 (MIL= Materials Institute Lavoisier), but we denoted it as micro-sized Eu-MOF in the text.⁸ $\text{Eu}(\text{NO}_3)_3 \cdot 5\text{H}_2\text{O}$ (0.1 g, 0.23 mmol) and H_3BTB (0.10 g, 0.23 mmol) were placed in a 50 mL vial. Water (6 mL) and 0.5 mL of a 2 M NaOH solution were added, and the mixture stirred at room temperature. After 2 min, warm ($T \approx 40^\circ\text{C}$) cyclohexanol (6 mL) was added and the biphasic mixture was stirred for 10 min. The vial was heated to 100 $^\circ\text{C}$ and kept at this temperature for 5 days. After cooling, the powder was washed several times with methanol and dried in an oven for 12 h at 363K. The TiO_2 powder (P-25, Japan Aerosil) used in this study is generously provided by the manufacturer. This photocatalyst has a Brunauer-Emmett-Teller (BET) surface area of 50 $\text{m}^2 \text{ g}^{-1}$, a primary particle size of about 20 nm, and a crystal structure of rutile

(20 %) and anatase (80 %).

Commercial sources of aromatic sulfides and aliphatic and aromatic amines were used as electron donors after purification before experiments as follows. *N,N,N',N'*-tetramethyl-*p*-phenylenediamine (TMPD, Aldrich) was purified by vacuum sublimation. Phenothiazine (Ptz, Tokyo Chemical Industry) was recrystallized from toluene. Triethylamine (TEA, Aldrich), 1,4-diazabicyclo[2.2.2]octane (DABCO, Aldrich), triphenylamine (Aldrich), 2,4,6-triphenylaniline (Aldrich), 4-(methylthio)phenylmethanol (TA-CH₂OH, Aldrich), thioanisole (TA, Tokyo Chemical Industry), 4-methylthioanisole (TA-Me, Tokyo Chemical Industry) and 4-methoxythioanisole (TA-OMe, Tokyo Chemical Industry) were used without further purification. Fresh acetonitrile (CH₃CN, Nacalai Tesque) was used as the solvent.

For the time-resolved emission and absorption measurements, sample suspensions containing the powders (8 mg per 40 mL solvent) were prepared and sonicated for 30 min. The suspensions in 1 cm optical cells were kept under dark condition at room temperature until used.

Characterizations.

To confirm the crystal phase and morphology of the prepared Eu-MOF particles, powder XRD and TEM measurements were performed by using a Rigaku RINT2500 XRD spectrometer with a Cu K α source and a Hitachi H-9000 instrument equipped with a tilting device operating at 300 kV, respectively. SEM images were also obtained with a Hitachi S-2150 instrument. Steady-state UV-visible absorption and diffuse reflectance spectra were measured with UV-visible-NIR spectrophotometers (Shimadzu, UV-3100, and Jasco, V-570, respectively). Steady-state emission spectra were measured by a Hitachi 850 fluorescence spectrophotometer. Measurements for the gas adsorption isotherms of N₂ (77 K) were performed using BELSORP-mini II volumetric adsorption equipment from BEL Japan.

Photocatalytic Efficiency Measurement of Eu-MOF and P-25 TiO₂.

1 cm \times 1 cm quartz cell containing Ar saturated acetonitrile solutions (2 mL) of TMPD (10 mM) with photocatalytic agents of either Eu-MOF nanoparticles or P-25 TiO₂ (5 mg mL⁻¹) was irradiated by a 120 W high-pressure Hg lamp (Asahi Spectra, REX-120) equipped with a bandpass filter (365

± 5 nm) for 10 min. After the photoirradiation, the photocatalytic particles remained in solution were completely removed by filtration using a PTFE filter (Whatman, 0.1 μm). The absorbance changes in UV-visible absorption spectra of the resultant solutions before and after irradiation were used to estimate the relative photocatalytic efficiency between the two different agents.

Time-Resolved Emission Measurements.

The emission lifetime measurements were performed using the third harmonic generation (355 nm, 5 ns fwhm, 20 mJ pulse⁻¹) from a Q-switched Nd³⁺:YAG laser (Continuum, Surelite II-10) for the excitation operated by temporal control using a delay generator (Stanford Research Systems, DG535). The emission from the sample was collected by a focusing lens and dispersed by a grating monochromator (Nikon, G250), and then detected by a silicon avalanche photodiode detector (Hamamatsu Photonics, S5343). The transient signals were averaged with 2000 events by a digitizer (Tektronix, TDS 580D) and fed into personal computer (PC) for further analysis. The decay curves were fitted using a nonlinear least-squares method with a multicomponent decay law given by $I(t) = a_1 \exp(-t/\tau_1) + a_2 \exp(-t/\tau_2) + \dots + a_n \exp(-t/\tau_n)$. The average lifetime $\langle \tau \rangle$ was then determined using the equation: $\langle \tau \rangle = \frac{\sum_{i=1}^{i=n} a_i \tau_i^2}{\sum_{i=1}^{i=n} a_i \tau_i}$.

Transient Absorption Measurements.

The transient absorption measurements were performed using the third-harmonic generation (355 nm, 5 ns fwhm, 10 mJ pulse⁻¹) from a Q-switched Nd³⁺:YAG laser (Continuum, Surelite II-10) for the excitation operated by temporal control using a delay generator (Stanford Research Systems, DG535). The analyzing light from a pulsed 450 W Xe arc lamp (Ushio, UXL-451-0) was collected by a focusing lens and directed through a grating monochromator (Nikon, G250) to a silicon avalanche photodiode detector (Hamamatsu Photonics, S5343). The transient absorption spectrum was obtained at the probe wavelength by scanning the monochromator. The transient signals at different wavelengths were also recorded by a digitizer (Tektronix, TDS 580D). The reported signals are the averages of 200 events.

Confocal Fluorescence Images Measurements.

Well-dispersed methanol suspensions of the micro-sized EuMOF samples were spin-coated on cleaned cover glasses and annealed at 363 K for 30 min to immobilize the particles on the surface.

Confocal fluorescence images were taken on an objective-scanning confocal microscope system (PicoQuant, MicroTime 200) based on an inverted microscope (Olympus, IX-71). The samples were excited through an oil objective (Olympus, UAPON 150XOTIRF) with a 405 nm continuous wave laser (PicoQuant, LDH-D-C-405) controlled by a PDL-800B driver (PicoQuant), and emission was collected with the same objective and detected by a single photon avalanche photodiode (Micro Photon Devices, PDM 50CT) through a dichroic beam splitter and a bandpass filter (Semrock, FF01-615/24-25).

Results and Discussion

Steady-state Spectral Measurements of Eu-MOF Powders.

It was found that synthesized Eu-MOF nanoparticles have a Brunauer-Emmett-Teller (BET) surface area of $1001 \text{ m}^2 \text{ g}^{-1}$, a pore volume of $0.50 \text{ cm}^3 \text{ g}^{-1}$, and a pore diameter of 2 nm. Powder X-ray diffraction (XRD) patterns of both samples were almost identical to those reported elsewhere (Figure 1).⁸ The morphological and structural features of the nanosized and micro-sized Eu-MOF particles were studied by using transmission electron microscopy (TEM) and scanning electron microscopy (SEM) and were found to have a rodlike shape (Figure 2). TEM and SEM images also show that nanosized Eu-MOF particles have a length of ca. 200 nm and a width of ca. 50 nm (Figure 2A) and micro-sized particles have lengths in the range of 2-5 μm (Figure 2B).

Figure 3 exhibits the steady-state

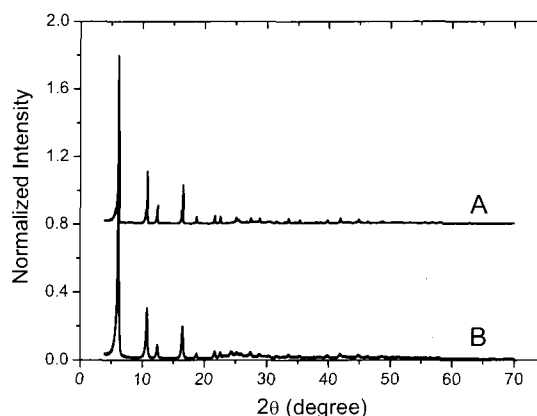


Figure 1. Powder XRD patterns obtained from synthesized Eu-MOF nanoparticles (A) and microparticles (B).

UV-visible diffuse reflectance, emission, and excitation spectra of Eu-MOF nanoparticles in

ambient atmosphere at room temperature. When the BTB ligands of Eu-MOF are selectively excited at 285 nm, one can observe the characteristic emission spectral features of Eu^{3+} ions at 593, 615, 653, and 698 nm, which are ascribed to the $^5\text{D}_0 \rightarrow ^7\text{F}_1$, $^5\text{D}_0 \rightarrow ^7\text{F}_2$, $^5\text{D}_0 \rightarrow ^7\text{F}_3$, and $^5\text{D}_0 \rightarrow ^7\text{F}_4$ transitions, respectively.⁶ It should be noted that no emission from the ligands was observed in the present wavelength region.⁵ These observations strongly suggest that the excitation energy

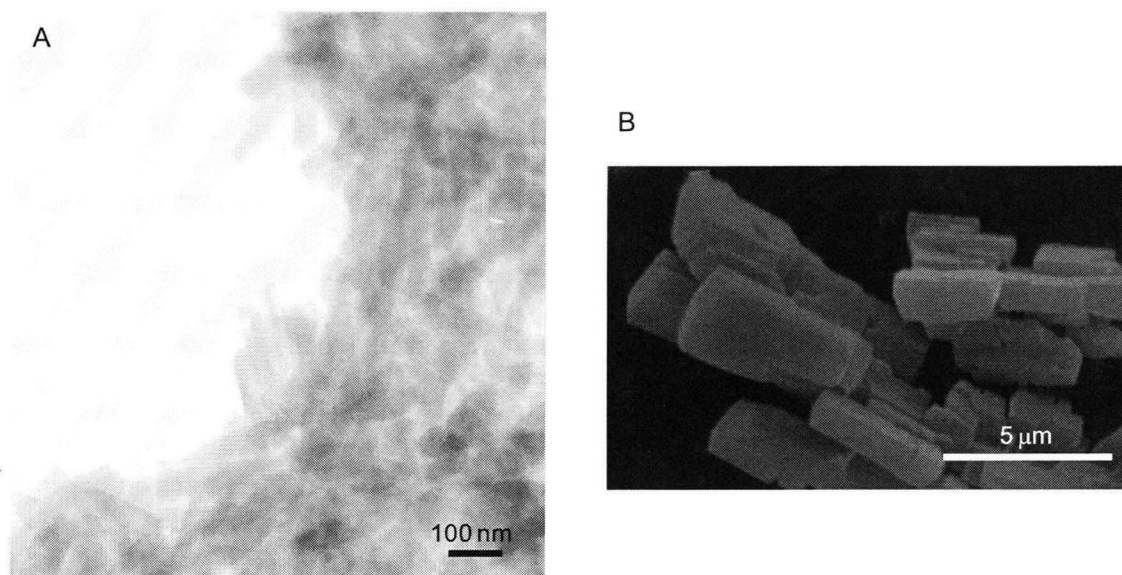


Figure 2. TEM image of Eu-MOF nanoparticles (A) and SEM image of Eu-MOF microparticles (B).

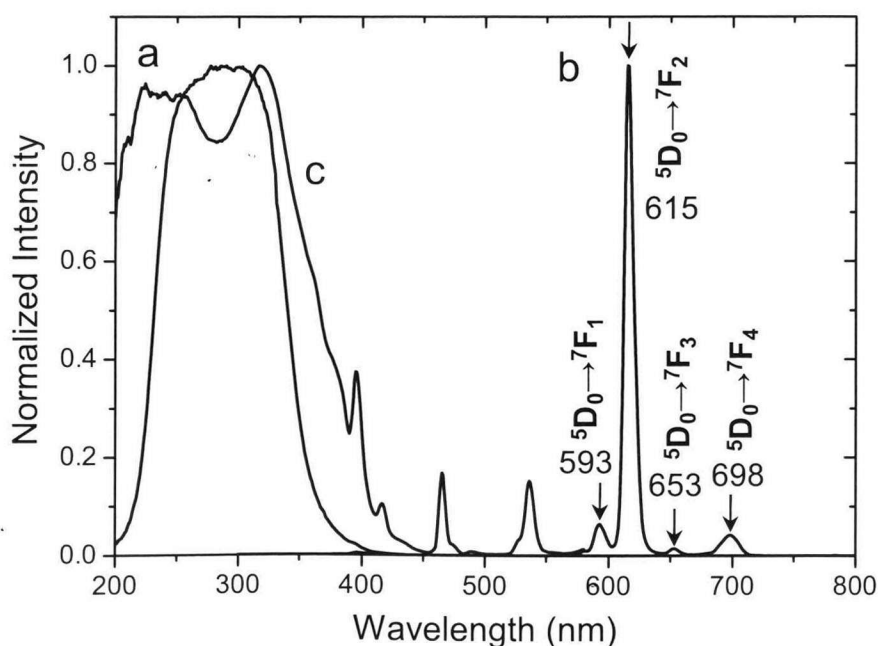


Figure 3. Steady-state diffuse reflectance (a), emission (b, excitation at 285 nm), and excitation (c, emission collected at 615 nm) spectra of nanosized Eu-MOF powders in the ambient atmosphere.

harvested in the BTB ligands is efficiently transferred to Eu^{3+} ions.

The Electron Transfer between the Photoexcited Eu-MOFs and Organic Compounds.

We first introduced *N,N,N',N'*-tetramethyl-*p*-phenylenediamine (TMPD) into an acetonitrile suspension of Eu-MOF nanoparticles. Because TMPD has a very low oxidation potential of +0.36 V versus NHE¹² and its oxidized form ($\text{TMPD}^{•+}$) causes a visible color change from colorless to blue,¹³ one can easily recognize the intermolecular electron-transfer reaction in the above system. As demonstrated in the inset of Figure 4, the color of the suspension containing Eu-MOF and TMPD changes to blue after UV irradiation (365 nm, 50 mW cm⁻²) for 10 min (b), whereas the solutions without Eu-MOF or TMPD result in no detectable change in solution color (a). The absorption spectrum clearly exhibits strong absorption bands at 565 and 614 nm after irradiation of the sample solution containing Eu-MOF and TMPD, which are in good agreement with those of $\text{TMPD}^{•+}$ (b in Figure 4).¹³ This fact assumes that the irreversible electron-transfer process takes place from TMPD molecules (electron donor) to the photoexcited Eu-MOF (electron acceptor) in

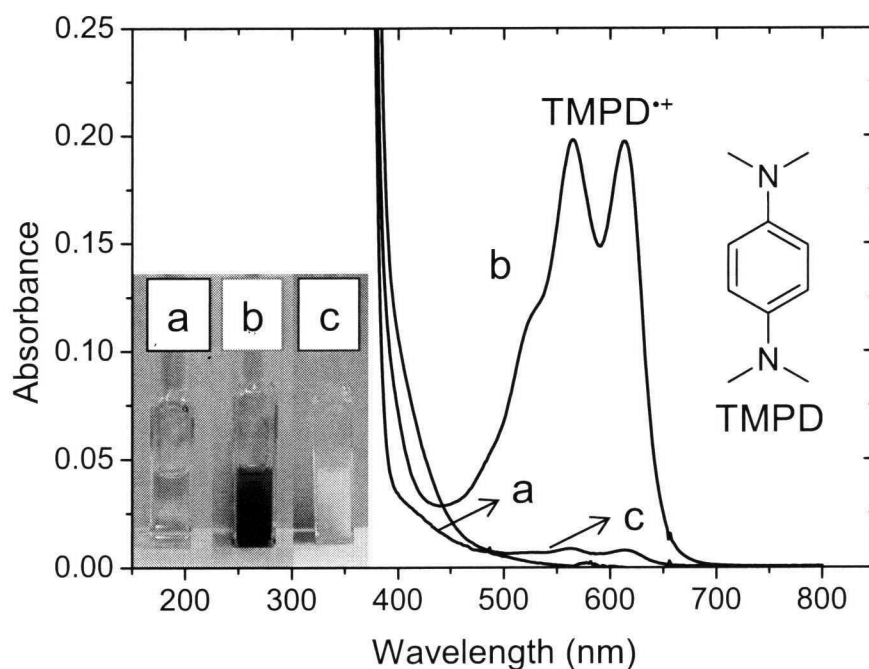


Figure 4. Steady-state UV-visible absorption spectra of TMPD (10 mM) in Ar-saturated acetonitrile before (a) and after UV irradiation for 10 min in the presence of Eu-MOF (b) or P-25 TiO_2 (c) nanoparticles. The inset shows the photographs of the optical cells containing the TMPD solutions in the absence (a) and presence of Eu-MOF (b) or P-25 TiO_2 (c) nanoparticles after UV irradiation for 10 min. The chemical structure of TMPD is also shown.

solution. When the Eu-MOF is replaced with a standard TiO₂ photocatalyst, P-25 (Japan Aerosil), and the sample is irradiated under the same conditions, the change in the solution color was not significant as compared with that of the reactant solution. This is consistent with the fact that TMPD molecules are more effectively adsorbed on the surfaces of Eu-MOF nanoparticles than are TiO₂ nanoparticles (BET surface area is ca. 50 m² g⁻¹, Figure 5).

To elucidate the reaction dynamics of excited Eu-MOF nanoparticles quantitatively, the emission decay profiles were measured at 615 nm by nanosecond time-resolved spectroscopy with a pulsed Nd³⁺:YAG laser (with a wavelength of 355 nm). Figure 6A shows the emission decay profiles of Eu-MOF nanoparticles in the absence and presence of 4-methoxythioanisole (TA-OMe) in acetonitrile. The measured emission decay profiles cannot be fit with single-exponential decay function, suggesting that Eu³⁺ ions have rather complicated relaxation dynamics between many

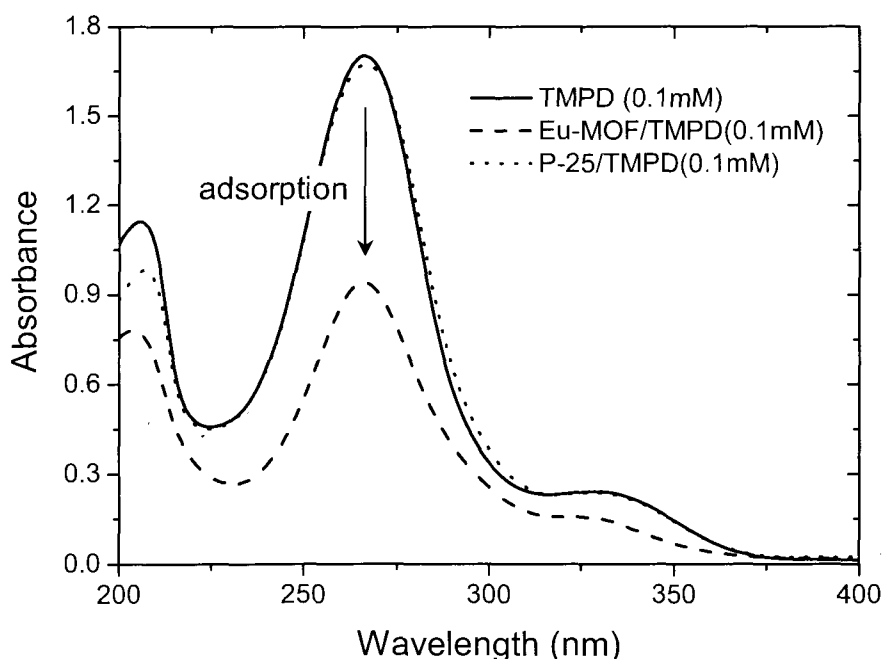


Figure 5. UV-visible absorption spectra of TMPD solution in acetonitrile after adsorption into Eu-MOF (dash line) and P-25 TiO₂ (dot line) under room light. It is interesting to note that the absorbance changes strongly dependent on the nature of photocatalyst under the same reaction conditions since the same amounts of Eu-MOF and P-25 TiO₂ nanoparticles is used. Steady-state UV-vis absorption spectra of TMPD (0.1 mM) (solid line) in acetonitrile at room temperature is also shown for comparison.

possible excited states. The triplet-triplet annihilation (i.e., $E^* + E^* \rightarrow E^{**} + E$, where E^* is the emissive excited state (5D_0 state), E^{**} is the higher excited state, and E is the ground state) is considered to be the primary reason for the complicated decay kinetics observed for Eu-MOF nanoparticles.¹⁴

The averaged emission lifetimes $\langle \tau \rangle$ were estimated from multiexponential fits for further data analysis.¹⁵ Upon increasing the concentration of TA-OMe, the $\langle \tau \rangle$ values apparently decreased. To determine the quenching rate constants (k_q), the $\langle \tau \rangle$ values are plotted against the concentration of quenchers (so-called Stern-Volmer plots). As shown in the inset of Figure 6A, an almost linear relationship between $\langle \tau \rangle^{-1}$ and the concentration of TA-OMe was obtained. The k_q value is then determined to be $7.2 \times 10^4 \text{ M}^{-1} \text{ s}^{-1}$ from a straight-line fit to the data, which is much lower than the diffusion-controlled rate constant, $\sim 10^{10} \text{ M}^{-1} \text{ s}^{-1}$, in the bulk solution. According to the fact that the samples incubated in the dark for 22 h results in the same k_q values, the contribution of the slow penetration of quenchers into the MOF structure over 30 min would be almost negligible (gray

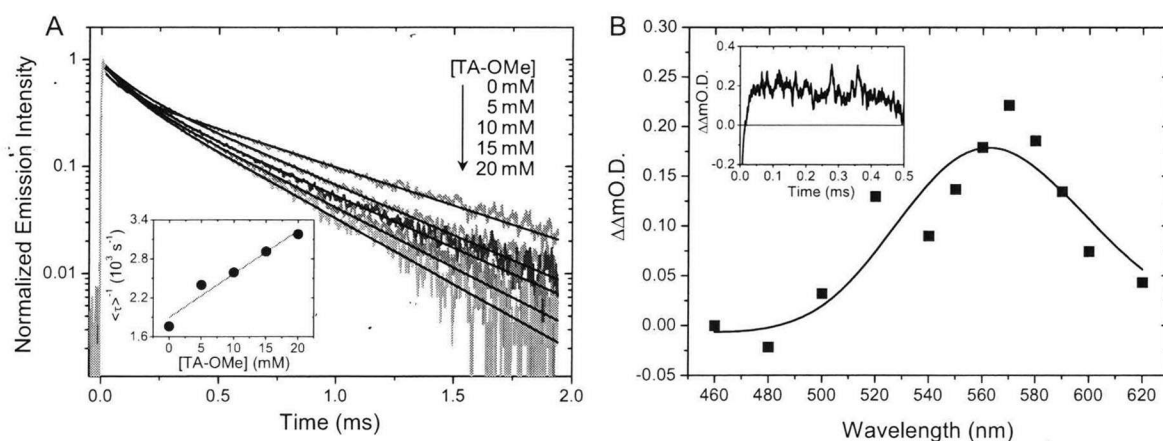


Figure 6. (A) Normalized emission decay profiles observed at 615 nm for Eu-MOF nanoparticles in acetonitrile in the absence and presence of TA-OMe. Black lines indicate the results fit by a biexponential function. The inset shows a linear relationship obtained for $\langle \tau \rangle^{-1}$ and the concentration of TA-OMe. (B) Transient absorption spectrum observed 40 μs after the laser flash during the 355 nm laser photolysis of Eu-MOF nanoparticles in acetonitrile in the presence of TA-OMe (20mM). The inset shows the time profile of transient absorption at 560 nm. The differential $\Delta\text{O.D.}$ ($\Delta\Delta\text{O.D.}$) values were obtained by subtracting the $\Delta\text{O.D.}$ values in the absence of TA-OMe from the $\Delta\text{O.D.}$ values in the presence of TA-OMe. The fit to a Gaussian function is shown by the solid line as a visual guide.

circles in Figure 7). Furthermore, as shown in Figure 6B, the transient absorption spectral feature obtained during 355 nm laser photolysis of Eu-MOF in the presence of TA-OMe in acetonitrile is almost identical to the reported ones for the radical cation of TA-OMe (TA-OMe^{•+}).¹⁶ This result strongly supports the conclusion that electron transfer from TA-OMe to photoexcited Eu-MOF occurs after the laser flash, even though it is difficult to estimate the formation rate of TA-OMe^{•+} accurately because of its very weak signal intensity and the interference from the Eu³⁺ emission (inset of Figure 6B). The k_q values determined for various quenchers are summarized in Table 1 with their oxidation potentials (E_{ox}) in acetonitrile. The free-energy change for electron transfer from organic quenchers to the excited Eu³⁺ is simply given by eq 1,^{17,18}

$$\Delta G_{ET} = E_{ox}(D) - E_{red}(A) - E_{exc}(A) \quad (1)$$

where $E_{ox}(D)$ and $E_{red}(A)$ are the electrochemical potentials for the donor and acceptor, respectively, and $E_{exc}(A)$ is the excited-state energy for the singlet or triplet state involved. The Coulomb interaction between the separated charges in acetonitrile is neglected because the interaction is considered to be negligibly small as compared to other parameters. For a theoretical estimation of the overall k_q , we have used the following well-known equation¹⁷

$$\frac{1}{k_q} = \frac{1}{k_{diff}} + \frac{1}{k_a} \quad (2)$$

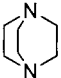
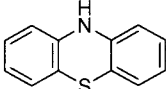
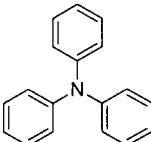
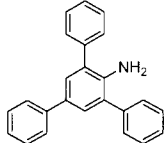
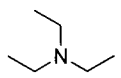
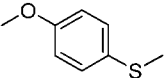
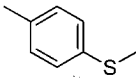
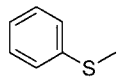
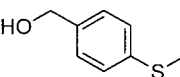
where k_{diff} ($= 1.9 \times 10^{10} \text{ M}^{-1} \text{ s}^{-1}$ in acetonitrile¹⁷) and k_a are the diffusion-controlled and the activation-energy-controlled electron-transfer reaction rate constants, respectively. The k_a value can be calculated using Marcus theory as given by eq 3,¹⁸

$$k_a = \sqrt{\frac{\pi}{\hbar^2 \lambda_s k_B T}} V(d_{DA})^2 \sum_{j_A, j_D} \text{FC}(j_A) \text{FC}(j_D) \times \exp \left\{ -\frac{(\lambda_s + \Delta G_{ET} + j_D \hbar \nu_D + j_A \hbar \nu_A)^2}{4 \lambda_s k_B T} \right\} \quad (3)$$

where \hbar is Planck's constant, λ_s is the solvent reorganization energy, $j_D \hbar \nu_D$ ($= \lambda_{v,D}$) and $j_A \hbar \nu_A$ ($= \lambda_{v,A}$) are the intramolecular reorganization energies for the electron donor and acceptor, respectively, and $V(d_{DA})$ is the electronic coupling element between electron donor and acceptor dependent on the distance between these species (d_{DA}) as given by eq 4,¹⁸

$$V(d_{DA}) = V_0 \exp \left\{ -\frac{\beta}{2} (d_{DA} - d_0) \right\} \quad (4)$$

Table 1. Molecular Structures and Oxidation Potentials (E_{ox}) of Quenchers and Free Energy Changes for Electron Transfer (ΔG_{ET}) and Quenching Rate Constants (k_q) Observed for Eu-MOF Nanoparticles

quencher	structure	diameter, nm	E_{ox} , V vs NHE	$-\Delta G_{ET}$, eV	k_q , $M^{-1} s^{-1}$
DABCO		0.48	+0.80 ^a	0.87	8.6×10^5 8.9×10^5 ^g
Ptz		0.94	+0.83 ^b	0.84	3.9×10^7
triphenylamine		0.97	+1.13 ^c	0.54	4.3×10^6
2,4,6-triphenylaniline		1.25	+1.18 ^d	0.49	2.2×10^6
TEA		0.64	+1.23 ^a	0.44	8.2×10^4 5.8×10^{4g}
TA-OMe		0.93	+1.37 ^e	0.30	7.2×10^4
TA-Me		0.85	+1.48 ^e	0.19	3.6×10^4
TA		0.74	+1.58 ^e	0.086	6.8×10^3
TA-CH ₂ OH		0.93	+1.59 ^f	0.076	2.8×10^4

^a Reference 24. ^b Reference 25. ^c Reference 26. ^d Reference 27. ^e Reference 28. ^f Reference 29. ^g The samples were kept under dark condition for 22 h.

where V_0 is the V at the contact distance (d_0) and β is the decay parameter. The λ_s for the electron transfer is given by eq 5,¹⁸

$$\lambda_s = \frac{e^2}{4\pi\epsilon_0} \left(\frac{1}{2r_D} + \frac{1}{2r_A} - \frac{1}{d_{DA}} \right) \left(\frac{1}{n^2} - \frac{1}{\epsilon} \right) \quad (5)$$

where r_D and r_A are the radii of the electron donor and acceptor, d_{DA} is their center-to-center separation at the instant of electron transfer, respectively. The permittivity constant of a vacuum, the refractive index and dielectric constant of the solvent are represented by ϵ_0 , n , and ϵ , respectively ($n = 1.344$ and $\epsilon = 37.5$ for acetonitrile at 293 K). Using eqs 3-5 and taking the values of $\lambda_{V,A} = 0$ eV and $\lambda_{V,D} = 0.3$ eV for Eu^{3+} ions¹⁹ and organic molecules,²⁰⁻²² respectively, $r_A = 0.19$ nm¹⁹ and $r_D = 0.43$ nm (average value for the studied quenchers), and $d_{DA} = 1.0$ nm (pore radius of Eu-MOF), we have calculated the λ_s value of 2.1 eV. Overall, the kinetic data give a reasonable fit to eq 3 with $V_0 = 300 \text{ cm}^{-1}$,²³ $\beta = 0.1 \text{ nm}^{-1}$,²³ the average frequency ν_D of 1500 cm^{-1} ,²⁰ as shown by a solid line in Figure 7. It should be noted that the k_q values observed for the present Eu-MOF systems are much higher by two or three orders of magnitude than those between the photoexcited

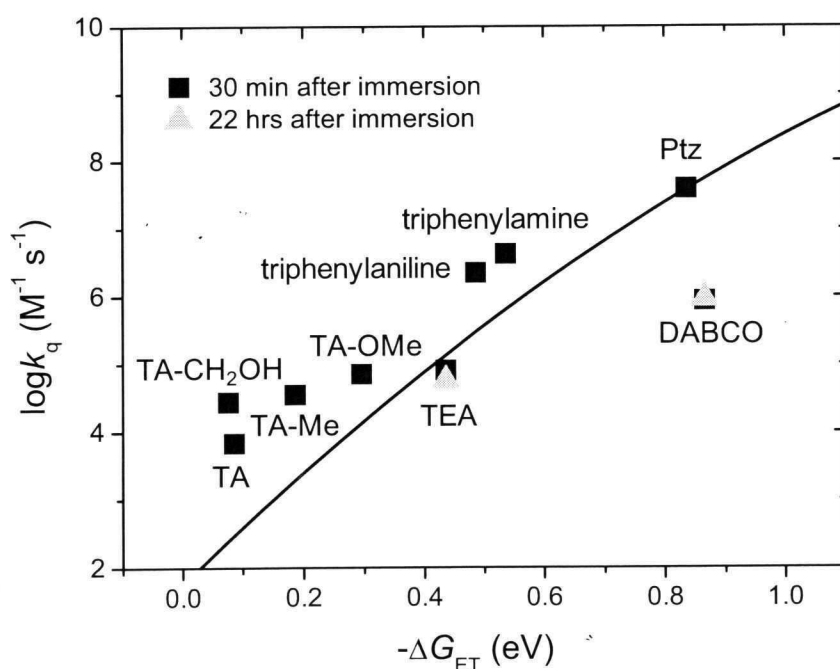


Figure 7. $-\Delta G_{ET}$ dependence of the k_q values between the photoexcited Eu-MOF nanoparticles and electron donors in acetonitrile. The black line represents the calculated k_q values.

MOF-5 and the same electron donors, when these values are compared at the same ΔG_{ET} .⁴ This large difference between the two systems might be due to the difference in the reorganization energies of electron-accepting sites, i.e., Eu^{3+} in Eu-MOF ($\lambda_{v,A} \sim 0$ eV)¹⁹ and surface defects in MOF-5 ($\lambda_{v,A} \sim 1$ eV)⁴, and the pore diameters of Eu-MOF (2.0 nm) and MOF-5 (1.2 nm) that contribute to the accessibility of quenchers to the reactive sites. Furthermore, a small difference in k_q observed for thioanisole (TA) and 4-(methylthio)phenylmethanol (TA-CH₂OH) suggests that the adsorption of organic compounds by -OH groups on the surface of Eu-MOF is relatively insignificant compared to Zn-based MOFs and metal oxides, such as ZnO and TiO₂.^{4,29}

Confocal Fluorescence Microscope Images of Microsized Eu-MOF Particles.

To examine how deeply quenchers penetrate the pore structures of Eu-MOF, we have investigated the change in fluorescent images before and after adding electron donors with different molecular sizes by utilizing confocal fluorescence microscopy. Confocal fluorescence microscopy is well suited for these investigations because the optical slice images enable 3D scans of objects with a resolution of ca. 200 nm in the horizontal direction and ca. 600 nm in depth. For this purpose, we have synthesized microsized Eu-MOF because the size of Eu-MOF nanoparticles (about 200 nm in length and 50 nm in diameter) used in this work is smaller than the optical diffraction limit. Figure 8 shows the luminescence quenching images of microsized Eu-MOF in the presence of phenothiazine (Ptz) (1 mM) or 1,4-diazabicyclo[2.2.2]octane (DABCO) (10 mM) in acetonitrile. Before quenchers were added, Eu-MOF particles exhibited a bright luminescent image (image a) without significant bleaching during the 405 nm laser irradiation.

The addition of Ptz molecules to the solution apparently and efficiently quenches the Eu^{3+} emission from the excited Eu-MOF. The most interesting observation is that the differential images (images c-e) as well as the images for quenching efficiency (QE) after the addition of the quencher (images f-h) demonstrate a slow but apparent penetration of Ptz molecules from the exterior surface into the inside of Eu-MOF particles with immersion time. After the exposure of the Ptz solution for 30 min, the QE was found to be more than 50% for the whole particles. Furthermore, the observation that the emission intensity of Eu-MOF particles was almost recovered after washing

with acetonitrile solvent implies that the quencher molecules were reversibly incorporated in the MOF structures without permanent adsorption inside pores and the decomposition of the frameworks. On the contrary, as shown in Figure 8i-k, the QE images for DABCO (10 mM) with different immersion times show that DABCO molecules penetrate into the Eu-MOF much faster

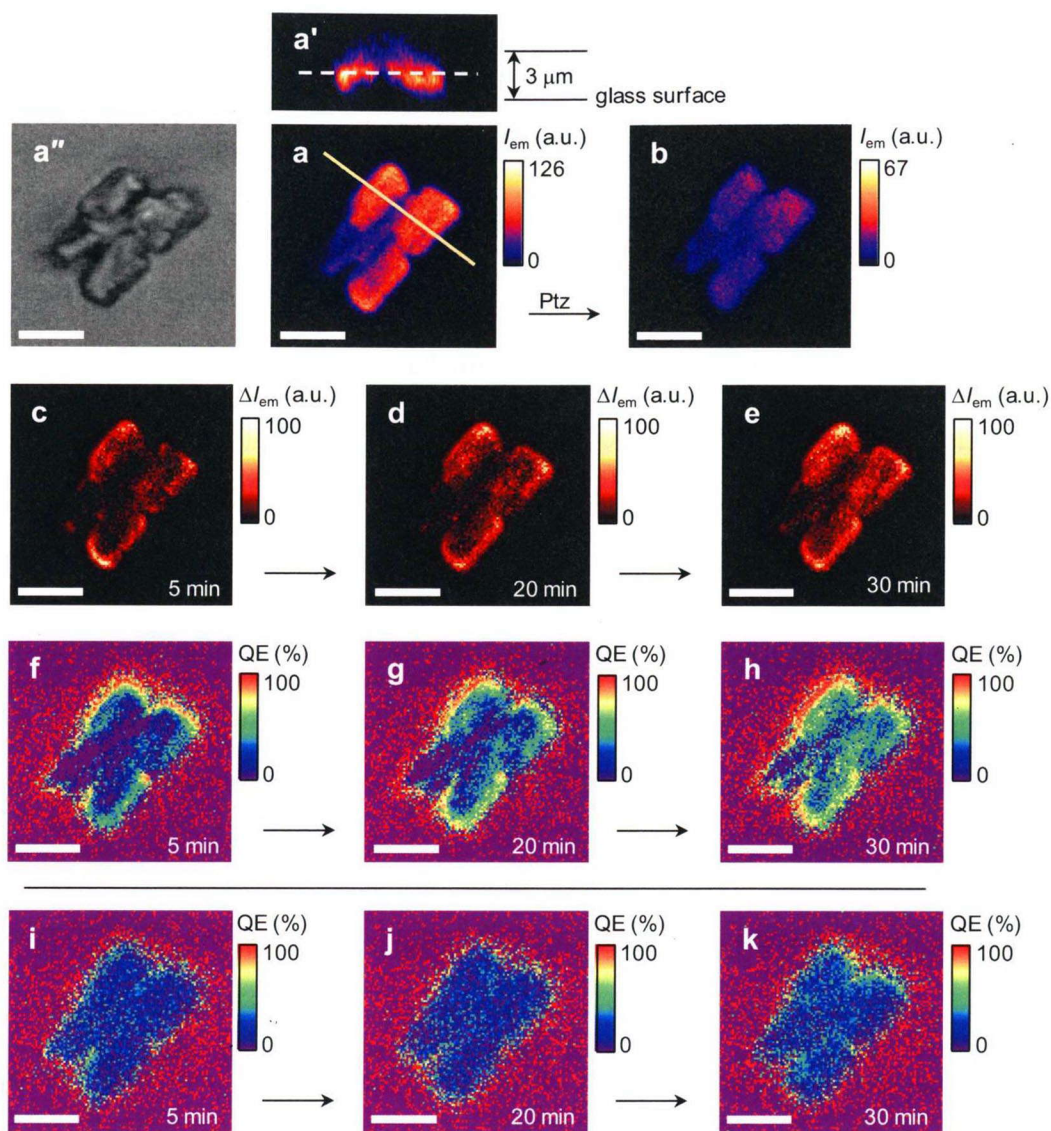


Figure 8. Confocal fluorescence microscope images of micro-sized Eu-MOF particles in the absence (a) and presence (b) of Ptz (1 mM) in acetonitrile. Images are obtained 1.5 μm above the glass surface (see broken line in image a''). Images a' and a'' are the sliced emission images (the line in image a) and the optical transmission image, respectively. Shown are the differential images (c-e), which are obtained by subtracting the image in the absence of quencher (image a) from the image in the presence of quencher (image b), and the images for quenching efficiency (QE), which are obtained by dividing the differential images (images c-e) by the initial image (image a), observed 5, 20, and 30 min after the addition of Ptz (f-h). The QE images for DABCO (10mM) are also shown (i-k). All scale bars are 3 μm .

than does Ptz. Similar tendencies were observed for other Eu-MOF particles. This result can be explained with the difference in the molecular size because the diameter of the DABCO molecule (0.48 nm) is much smaller than that of the Ptz molecule (0.94 nm). A close inspection of the observed luminescence quenching images does not indicate any abrupt depletion of emission for the examined area, which might be observable if any quenching of the Eu^{3+} emission is mainly governed by the penetration of quenchers through surface defects such as tiny cracks. The other notable observation is that the QE for DABCO is apparently lower than that for Ptz. This is consistent with the observation that k_q for DABCO is almost 2 orders of magnitude lower than that for Ptz (Figure 7). The difference of the molecular sizes of quenchers should affect the electron-transfer dynamics even if both the systems have a similar ΔG_{ET} . Indeed, the calculated k_a using eq 3 decreased by over 3 orders of magnitude when r_D was changed from 0.47 nm for Ptz to 0.24 nm for DABCO and the other parameters were fixed. This decrease in k_a is primarily attributed to the increase in λ_S by 0.77 eV. This undesired molecular size effect on λ_S , lowering k_q and eventually the overall yield of the one-electron oxidation reaction, would be partially compensated for by the higher penetration rates of smaller organic substrates in the framework.

Conclusions

For the first time, we discovered the size-selective one-electron oxidation processes of organic compounds under the photoirradiation of nanosized and microsized Eu-MOF particles by combining time-resolved emission and absorption spectroscopy, confocal microscopy, and a theoretical calculation based on the Marcus theory. Our findings led us confidently to assume the possibility that Eu-MOFs work as an efficient photocatalyst under UV light irradiation. By varying the length of the organic backbone of the ligands and by changing the degree of conjugation in the ligands, molecular recognition MOF photocatalysts extending their photosensitivity toward the visible light region will be developed.

References and Notes

1. Yaghi, O. M.; O'Keeffe, M.; Ockwig, N. W.; Chae, H. K.; Eddaoudi, M.; Kim, J. *Nature* **2003**, *423*, 705-714.
2. Kitagawa, S.; Kitaura, R.; Noro, S. *Angew. Chem. Int. Ed.* **2004**, *43*, 2334-2375.
3. Alvaro, M.; Carbonell, E.; Ferrer, B.; Llabrés i Xamena, F. X.; Garcia, H. *Chem. -Eur. J.* **2007**, *13*, 5106-5112.
4. Tachikawa, T.; Choi, J. R.; Fujitsuka, M.; Majima, T. *J. Phys. Chem. C* **2008**, *112*, 14090-14101.
5. Choi, J. R.; Tachikawa, T.; Fujitsuka, M.; Majima, T. *J. Phys. Chem. Lett.* **2010**, *1*, 1101-1106.
6. Allendorf, M. D.; Bauer, C. A.; Bhakta, R. K.; Houk, R. J. T. *Chem. Soc. Rev.*, **2009**, *38*, 1330-1352.
7. Binnemans, K. *Chem. Rev.*, **2009**, *109*, 4283-4374.
8. Devic, T.; Serre, C.; Audebrand, N.; Marrot, J.; Férey, G. *J. Am. Chem. Soc.* **2005**, *127*, 12788-12789.
9. Macero, D. J.; Anderson, L. B.; Malachuk, P. *J. Electroanal. Chem.* **1965**, *10*, 76-81.
10. Yamanaka, I.; Nakagaki, K.; Akimoto, T.; Otsuka, K. *J. Chem. Soc., Perkin Trans.* **1996**, *2*, 2511-2517.
11. Casanova, D.; Bouzigue, C.; Nguyen, T.-L.; Ramodiharilafy, R. O.; Bouzahir-Sima, L.; Gacoin, T.; Boilot, J.-P.; Tharaux, P.-L.; Alexandrou, A. *Nat. Nanotech.* **2009**, *4*, 581-585.
12. Bock, C. R.; Connor, J. A.; Gutierrez, A. R.; Meyer, T. J.; Whitten, D. G.; Sullivan, B. P.; Nagle, J. K. *J. Am. Chem. Soc.* **1979**, *101*, 4815-4824.
13. Albrecht, A. C. *Acc. Chem. Res.* **1970**, *3*, 238-248.

14. Baldo, M. A.; Adachi, C.; Forrest, S. R. *Phys. Rev. B* **2000**, *62*, 10967-10977.
15. James, D. R.; Liu, Y.-S.; De Mayo, P.; Ware, W. R. *Chem. Phys. Lett.* **1985**, *120*, 460-465.
16. Yokoi, H.; Hatta, A.; Ishiguro, K.; Sawaki, Y. *J. Am. Chem. Soc.* **1998**, *120*, 12728-12733.
17. Turro, N. J.; Ramamurthy, V.; Scaiano, J. *Modern Molecular Photochemistry of Organic Molecules*. University Science Books: Sausalito, California, 2010.
18. Marcus, R. A.; Sutin, N. *Biochim. Biophys. Acta.* **1985**, *811*, 265-322.
19. Inada, T.; Funasaka, Y.; Kikuchi, K.; Takahashi, Y.; Ikeda, H. *J. Phys. Chem. A* **2006**, *110*, 2595-2600.
20. Gould, I. R.; Ege, D.; Moser, J. E.; Farid, S. *J. Am. Chem. Soc.* **1990**, *112*, 4290-4301.
21. Balakrishnan, G.; Keszthelyi, T.; Wilbrandt, R.; Zwier, J. M.; Brouwer, A. M.; Buma, W. J. *J. Phys. Chem. A* **2000**, *104*, 1834-1841.
22. Kowert, B. A.; Marcoux, L.; Bard, A. J. *J. Am. Chem. Soc.* **1972**, *94*, 5538-5550.
23. Tavernier, H. L.; Kalashnikov, M. M.; Fayer, M. D. *J. Chem. Phys.* **2000**, *113*, 10191-10201.
24. Ruiz, G.; Rodriguez-Nieto, F.; Wolcan, E.; Féliz, M. R. *J. Photochem. Photobiol., A* **1997**, *107*, 47-54.
25. Barra, M.; Calabrese, G. S.; Allen, M. T.; Redmond, R. W.; Sinta, R.; Lamola, A. A.; Small, R. D. J.; Scaiano, J. C. *Chem. Mater.* **1991**, *3*, 610-616.
26. Weinberg, N. L.; Weinberg, H. R. *Chem. Rev.*, **1968**, *68*, 449-523.
27. Lund, H. *Electrochimica Acta*, **2006**, *52*, 272-277.
28. Fukuzumi, S.; Shimoosako, K.; Suenobu, T.; Watanabe, Y. *J. Am. Chem. Soc.* **2003**, *125*, 9074-9082.

29. Tachikawa, T.; Fujitsuka, M.; Majima, T. *J. Phys. Chem. C* **2007**, *111*, 5259-5275.

Chapter 3

Host-Guest Interactions in MOF Nanoparticles Using a Polarity-Sensitive Probe

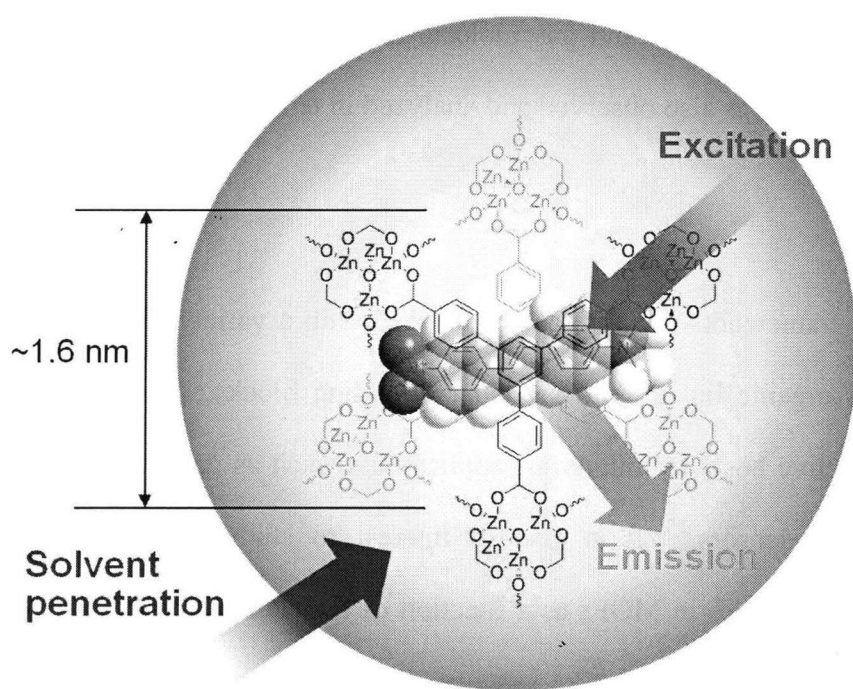
Abstract

We report in situ observations of molecular interactions and photodynamics for the polarity-sensitive fluorescence dye 4-dimethylamino-4'-nitrostilbene (DNS) when encapsulated inside of metal-organic frameworks (MOFs) by utilizing single-molecule, single-particle fluorescence spectroscopy. While the fluorescence intensity from DNS molecules adsorbed onto the surface of MOF-177 particles exhibited a strong solvent polarity dependence toward external solvent exchanges, the intensity from molecules encapsulated inside of well-defined MOF-177 particles slightly changed when the solvent was switched from toluene to chloroform. Furthermore, the photostability of the DNS molecules was significantly enhanced by incorporation into the MOF host. These observations strongly suggest that guest molecules encapsulated in MOFs should be protected from external solvent and gas molecules. The photoblinking behavior of encapsulated single DNS molecules was also observed and analyzed in terms of the probability density.

Introduction

Metal-organic frameworks (MOFs) can be formed with a variety of chemical structures via the self assembly of organic linkers and secondary building blocks.¹ Their widely tunable topology makes them attractive hosts for numerous applications, such as gas storage, catalysis, separations, drug delivery, and sensors.^{2,3} It is also of interest to study the photodynamic behaviors of incorporated chromophores in MOFs as a function of their local environmental structure since the molecular dynamics in nanosized pore systems should be affected by physicochemical-confining characteristics of the porous materials. Host-guest interactions have been studied through various

means, including spectroscopic measurements.⁴⁻⁶ For example, fluorescence dyes can be used as molecular probes to directly explore the local structures, molecular diffusion, and chemical reactions in porous hosts such as zeolites and mesoporous silica.⁵ The dynamics of molecules in host materials are rather complicated because these materials are highly heterogeneous both structurally and chemically. However, there are no previous studies that have reported detailed photophysical and photochemical properties of guest molecules in MOFs. A thorough examination of this issue will help us to better understand the molecular interactions within nanopores and provide an exciting new direction for control of materials properties on the molecular level. In this paper, we report the first example of in situ observations for host-guest interactions in individual MOF particles using the polarity-sensitive fluorescent probe 4-dimethylamino-4'-nitrostilbene (DNS) (Scheme 1).^{7,8} Among the MOF families, MOF-177, $\text{Zn}_4\text{O}(\text{1,3,5-benzenetricarboxylate})_2$, has an opening diameter of up to 1.4 nm and pore diameters of up to 1.7 nm, which are consistent with a high surface area of $4500 \text{ m}^2 \text{ g}^{-1}$ and a large pore volume of $1.59 \text{ cm}^3 \text{ g}^{-1}$; this implied that it was capable of including gas molecules such as H_2 and N_2 as well as much larger molecules like C_{60} and organic dyes.^{9,10}



SCHEME 1. Structure of a DNS Encapsulated MOF-177 Particle

Experimental Methods

Materials.

Submicrometer-sized MOF-177 particles were synthesized according to the procedures reported in literature with some modifications. Triethylamine (TEA) (130 μ L, 0.93 mmol) was very slowly added to *N,N*-dimethylformamide (DMF) solution (40 mL) containing $\text{Zn}(\text{NO}_3)_2 \cdot x\text{H}_2\text{O}$ (0.5 g, 2.64 mmol, Aldrich) and 1,3,5-tris(4-carboxyphenyl)benzene (H_3BTB , 0.2 g, 0.46 mmol, Aldrich). The mixture was allowed to stand for 2 h at room temperature and the resulting solid was collected by centrifugation, washed three times with DMF and chloroform, and then dried in an oven for 12 h at 363 K. MOF-177 is obtained when the $\text{Zn}(\text{NO}_3)_2 \cdot x\text{H}_2\text{O}/\text{H}_3\text{BTB}$ ratio is 6 and the TEA/ H_3BTB ratio is 2-3.

Characterizations.

To confirm the crystal phase and morphology of the prepared MOF-177 particles, powder X-ray diffraction (XRD) and transmission electron microscope (TEM) measurements were performed using a Rigaku RINT2500 XRD spectrometer with a Cu $\text{K}\alpha$ source and a Hitachi H-9000 instrument equipped with a tilting device operating at 300 kV, respectively. Scanning electron microscope (SEM) images were also obtained with a Hitachi S-2150 instrument. Steady-state UV-visible absorption and diffuse reflectance spectra were measured with UV-visible-NIR spectrophotometers (Shimadzu, UV-3100, and Jasco, V-570, respectively). Reflectance data were transformed into a Kubelka-Munk function. Steady-state emission spectra were measured by a Hitachi 850 fluorescence spectrophotometer. Measurements for the gas adsorption isotherms of N_2 (77 K) were performed using BELSORP-mini II volumetric adsorption equipment from BEL Japan. MOF-177 powders were placed in a sample tube and dried at 393 K for 6 h under vacuum before the measurements. The BET surface area was calculated from a line regression plot of $1/(V((P_0/P) - 1))$ versus P/P_0 (where V is the total volume absorbed at a particular P/P_0 point and P_0 is 1 atm of pressure) within the range of $0.02 < P/P_0 < 0.05$.

Inclusion of DNS into MOF-177.

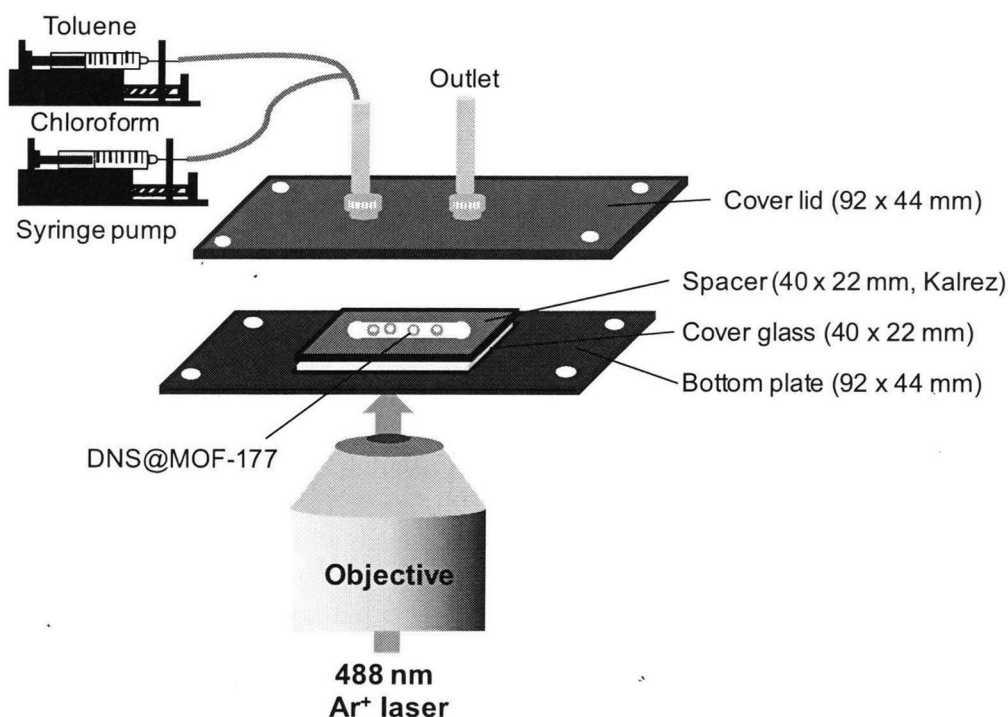
The synthesized MOF-177 was heated at 393 K for 6 h under vacuum to remove adsorbed

solvent and water molecules on the MOF-177 surface. It was immersed in a $1\mu\text{M}$ toluene solution of DNS (Fluka) ($[\text{MOF-177}] = 5\text{ g L}^{-1}$) at room temperature for 24 h under argon flow. To completely remove the excess DNS, the resultant material, denoted as DNS@MOF-177, was thoroughly washed with toluene, and then dried at 363 K for 12 h.

All chemicals were purchased from commercial sources (Aldrich, Tokyo Chemical Industry, and Nacalai Tesque) in the highest grade available and used without further purification.

Sample Preparations for Single-Molecule, Single-Particle Experiments.

Well-dispersed chloroform suspensions of the MOF samples were spin-coated on cleaned cover glasses. The cover glasses were annealed at 363 K for 30 min to immobilize the particles on the glass surface, and then mounted at the bottom of a single-stream flow cell that allowed the simultaneous exposure of the particles to a liquid medium and the monitoring the fluorescence signal (Scheme 2). The position of the particles was determined by the transmission image obtained by illumination from the halogen lamp above the sample and the photoluminescence image under the 365 nm light excitation of MOF-177 (Figure 2B).



SCHEME 2. Schematic Illustration of Home-Made Single-Stream Flow Cell

Single-Molecule, Single-Particle Measurements.

The experimental setup was based on an Olympus IX71 inverted fluorescence microscope. A circular-polarized continuous wave (CW) light emitted from a 488 nm Ar⁺ laser (Melles Griot, 35LAS450; 50 mW; $\sim 2 \text{ kW cm}^{-2}$, at the cover glass surface) that passed through an oil-immersion objective lens (Olympus, UPlanSApo, 1.40 NA, 100 \times) after reflection by a dichroic mirror (Olympus, DM505) was used to excite the sample. The emission from single particles on the cover glass was collected by using the same objective lens, and passed through an emission filter (Olympus, BA510IF) to remove undesired scattered light; the emission image was captured by imaged by an electron-multiplying charge-coupled device (EM-CCD) camera (Roper Scientific, Cascade II:512). The images were processed with Image J software (<http://rsb.info.nih.gov/ij/>). The background threshold was modified by the shot noise in each image above the background. Counts above the threshold were then considered to be the fluorescence signal. For spectroscopy, only the emissions that passed through a slit entered the imaging spectrograph (Acton Research, SP-2356); it was equipped with an EM-CCD camera (Princeton Instruments, PhotonMAX:512B). The width of the slit was 100 μm , which corresponded to 0.6 μm at the specimen because the images at the slit were magnified by the built-in 1.6 \times changer. The spectra were typically integrated for 5 s. The spectrum detected by the EM-CCD camera was stored in and analyzed with a personal computer. All experimental data were obtained at room temperature. A general approach was used to define the intensity threshold in order to distinguish between the on and off states. To determine the threshold that separates these states, the emission intensity distribution was fitted by a sum of two Gaussian functions. To determine the threshold that separates these states, the emission intensity distribution was fitted by a sum of two Gaussian functions. The threshold was chosen to be 3 σ greater than the background noise levels. Counts above the threshold were then assigned to the “on state”. At sufficiently long times, the histograms have only one or no counts per bin time due to finite counting statistics. Therefore, we analyzed the probability density, $P(t_{\text{off}})$, by weighting each point in the on histograms by the average time (Δt_{av}) between the nearest neighbor event bins using the following equation:

$$P(t_{\text{off}}) = \frac{N(t_{\text{off}})}{N_{\text{total}}} \times \frac{1}{\Delta t_{\text{av}}} \quad (1)$$

where $N(t_{\text{off}})$ and N_{total} are the number of off events of duration (t_{off}) and the total number of off events, respectively. The time distributions of the off-events follow a simple power law behavior as given by¹

$$P(t_{\text{off}}) = At^{-\alpha} \quad (2)$$

where A is the scaling coefficient and α is the power-law exponent that describes the distribution.

Fluorescence Lifetime Measurements.

The time-resolved emission spectra and decays were measured by time-correlated single photon counting (TCSPC) using a streak scope (Hamamatsu Photonics, C4334-01) equipped with a polychromator (Acton Research, SpectraPro150). The second harmonic oscillation (450 nm) of the output for the femtosecond laser (Spectra-Physics, Tsunami 3941-M1BB; full width at half-maximum (fwhm), 80 fs; 900 nm) pumped by a diode-pumped solid-state laser (Spectra-Physics, Millennia VIIIs) was used to excite the sample in a quartz cell. The observed temporal emission profiles fitted well to single or double exponential functions. All the measurements were carried out at room temperature.

Results and Discussion

Steady-State Spectral Measurements of MOF-177 Powders.

It was found that synthesized MOF-177 nanoparticles have the primary particle size is 0.5-1 μm , the BET surface area is 4482 $\text{m}^2 \text{g}^{-1}$, the pore volume is 1.80 $\text{cm}^3 \text{g}^{-1}$, and the average pore diameter is 1.6 nm) as a host material according to the procedures reported in the literature with some modifications.⁹⁻¹¹ There were no apparent changes in the powder XRD patterns during incorporation of DNS into MOF-177; the patterns were almost identical to those reported elsewhere (Figure 1).^{9,10} These results reveal that the MOF-177 framework structure was maintained even when DNS was incorporated (Figure 1A). Figure 1B shows the powder XRD patterns of dry MOF-177 powder, MOF-177 powder wetted with toluene, and dried MOF-177 powder after immersion in toluene. A

broad peak at around 18 degrees is due to the solvent. Figure 1C shows the magnified diffraction patterns at low angle region of panel B. XRD peaks were shifted to the higher angle, when MOF-177 powders were immersed in toluene. After the MOF-177 powder in toluene was completely dried up, the peaks returned to their original position. Figure 1D shows the powder XRD patterns at low angle region of dry DNS@MOF-177 powder and DNS@MOF-177 powder wetted with toluene. The peak widths at around 5.38 and 5.80 degrees become broad and the peak positions are shifted to the higher angle after immersion in toluene. The results of MOF-177 powders are also shown for comparison.

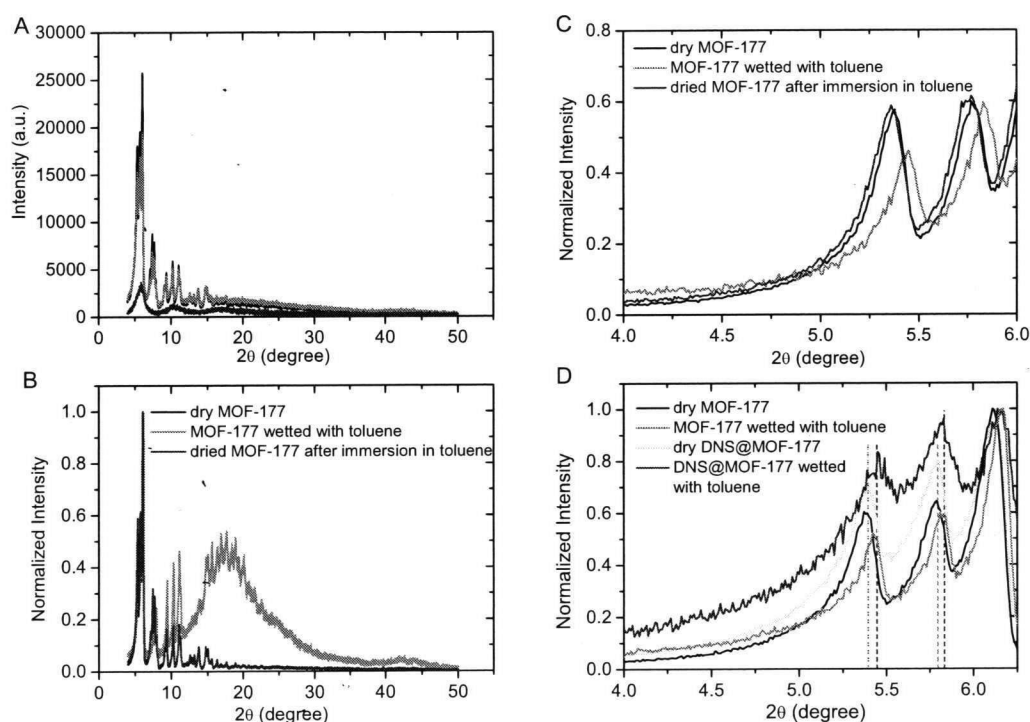


Figure 1. (A) Powder XRD patterns obtained for fresh MOF-177, DNS@MOF-177, and hydrated MOF-177 powders. (B) Powder XRD patterns of dry MOF-177 powder, MOF-177 powder wetted with toluene, and dried MOF-177 powder after immersion in toluene. A broad peak at around 18 degrees is due to the solvent. (C) Magnified diffraction patterns at low angle region of panel B. XRD peaks were shifted to the higher angle, when MOF-177 powders were immersed in toluene. After the MOF-177 powder in toluene was completely dried up, the peaks returned to their original position. (D) Powder XRD patterns at low angle region of dry DNS@MOF-177 powder and DNS@MOF-177 powder wetted with toluene.

Figure 2 shows the TEM image of MOF-177 particles. The average primary particle size was determined to be around 600 nm. The SEM images show the fresh MOF-177 and water-treated MOF-177 powders in Figure 3. These images show agglomerated particles. Fresh MOF-177 showed a regular pattern (Figure 3A), while no patterns were observed for the amorphous form (Figure 3B). The results can be explained in terms of hydrolysis of the MOFs, which also induces a remarkable reduction in surface area and pore structure by exposure of the MOF samples to moisture.

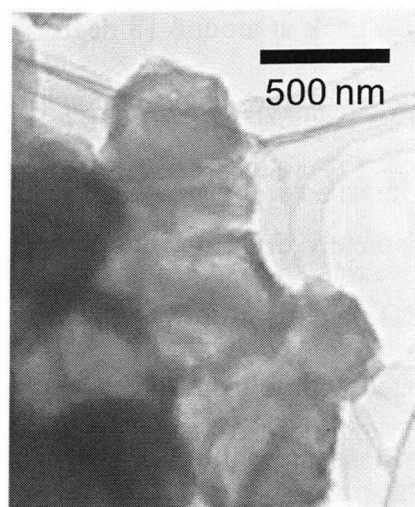


Figure 2. TEM image of MOF-177 particles. The average primary particle size was determined to be around 600 nm.

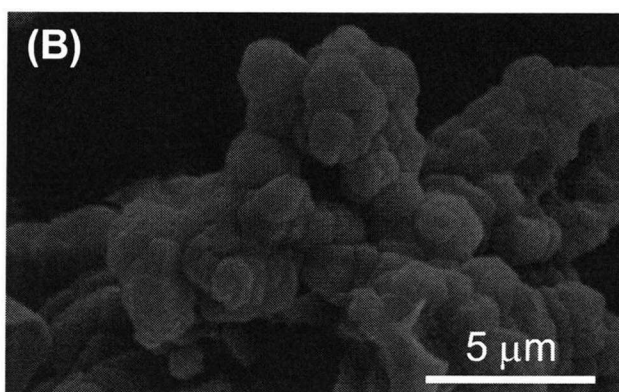
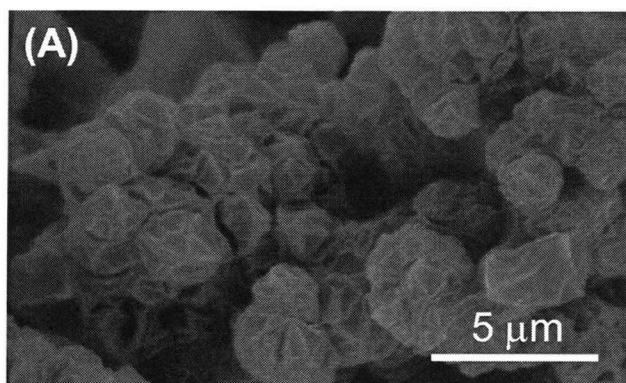


Figure 3. SEM images of freshly-prepared MOF-177 (A) and partially-decomposed (amorphous) MOF-177 (B) powders.

Figure 4 exhibits the steady-state UV-vis diffuse reflectance and emission spectra for DNS-encapsulated MOF-177 (DNS@MOF-177) particles and a toluene solution of DNS. The emission spectra from DNS in solvents of increasing polarity are provided in Figure 5 for the purpose of reference. The emission spectra shifted dramatically to longer wavelengths as the solvent polarity increased from hexane to acetonitrile. The high sensitivity of emission spectral features for the solvent polarity changes is due to a change of the dipole moment upon excitation.^{7,8} This indicates that DNS could be useful as a fluorescent probe for monitoring environmental polarity changes inside the MOF-177 cavity. The DNS@MOF-177 emission spectrum with a peak at

540-550 nm was observed under excitation at 488 nm, even though the DNS@MOF-177 absorption spectrum was not detectable due to the low loading efficiency of DNS ($\sim 1.4 \times 10^{-8}$ mol g⁻¹, as estimated from the absorbance change of the DNS solution).¹²

The observed peak wavelength in the emission spectrum strongly suggests that MOF-177 pores have a lower polarity than toluene ($\lambda_{\text{max}} = 565$ nm) but a higher polarity than hexane ($\lambda_{\text{max}} = 495$ nm). Since porous host materials such as zeolites are considered to be solid solvents, their characteristics can be described in terms of “solvent effects” as an analogy.¹³

Figure 6A and B depicts the emission and transmission images, respectively, of DNS@MOF-177 particles deposited on the cover glass (highlighted by circles). The

insets show magnified images of a single DNS@MOF-177 particle (see arrows). The particle size of the analyzed DNS@MOF-177 is on the scale of several hundreds of nanometers, which is close to that determined from TEM analysis (Figure 2). Figure 6C shows the histogram of the emission intensity averaged over the entire DNS@MOF-177 particle before photobleaching. For comparison, the histogram obtained from pure MOF-177 particles is also depicted. The emission intensity of particles apparently increased after incorporating DNS into MOF-177. Single-particle fluorescence spectra of individual DNS@MOF-177 particles were also observed under 488 nm laser excitation in ambient atmosphere (Figure 6D). The inset also shows the histogram for the emission peak position

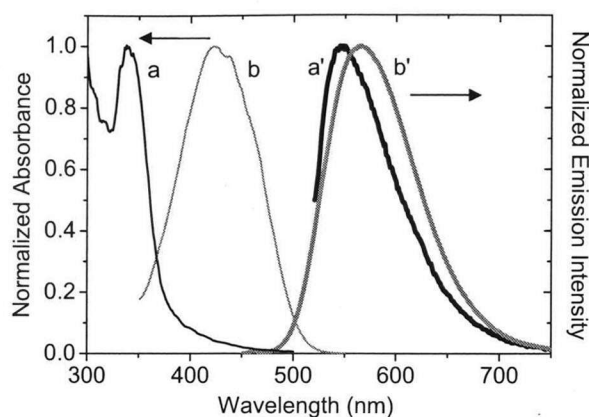


Figure 4. Steady-state UV-vis diffuse reflectance (a) and emission (a') spectra of DNS@MOF-177 powders in ambient atmosphere and absorption (b) and emission (b') of a toluene solution of DNS.

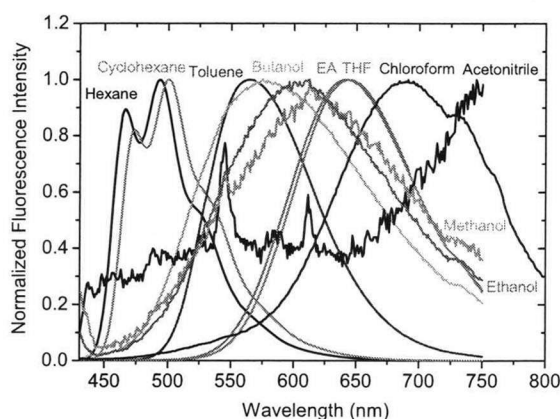


Figure 5. Steady-state fluorescence spectra of DNS in various solvents (EA: ethyl acetate, THF: tetrahydrofuran).

in wavenumbers. The histogram peak position for the DNS@MOF-177 emission was about 550 nm, which is very close to the value from the ensemble-averaged emission spectrum shown in Figure 4.¹⁴

DNS molecules in solution exhibited quite strong solvent dependence; its fluorescence quantum yield in chloroform (0.018) was about 30 times less than that in toluene (0.53).^{7,8} Our observations for both long-term and short-term exposure to environmental solvent indicated, however, that the emission intensity variation of DNS incorporated in a well-defined MOF-177 framework was only 30%, on average, upon changing the solvent from toluene to chloroform (Figure 7, left panel). It was also confirmed that DNS molecules encapsulated in MOF-177 are hardly desorbed from the MOF framework (Figure 8).

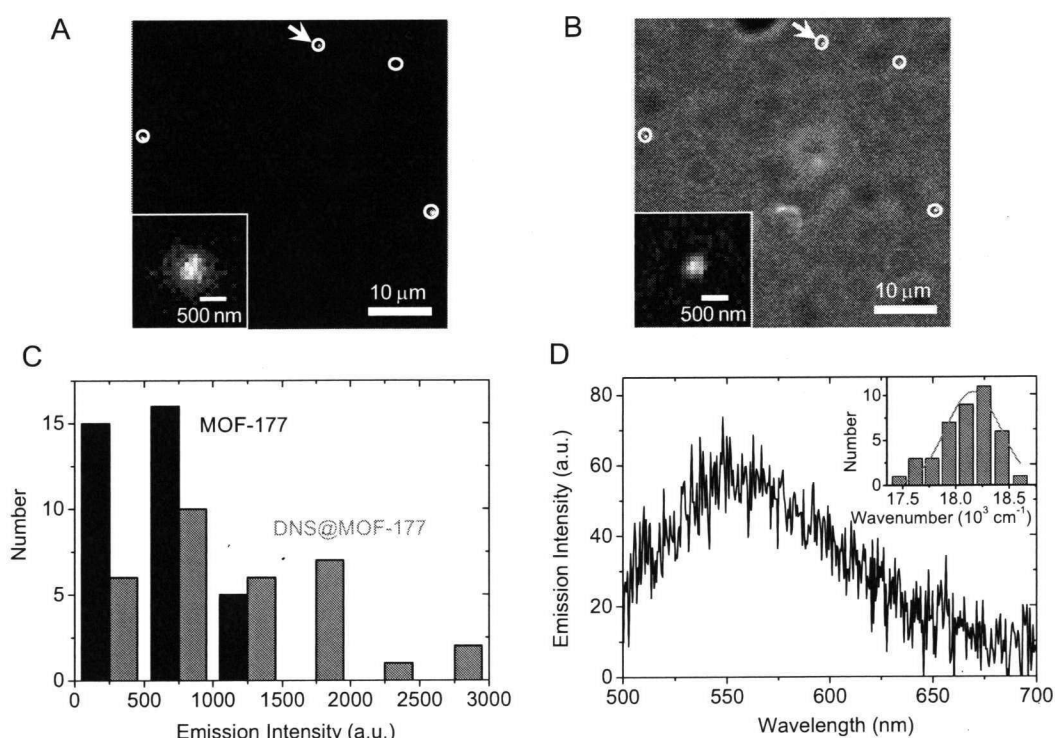


Figure 6. Emission (A) and transmission (B) images of DNS@MOF-177 particles on the cover glass in ambient atmosphere. The circles show identified DNS@MOF-177 particles. Insets show the magnified DNS@MOF-177 indicated by the arrows. (C) Histograms of the emission intensity observed for individual MOF-177 and DNS@MOF-177 particles. (D) Single-particle fluorescence spectrum observed during the 488 nm excitation of a single DNS@MOF-177 particle. The inset shows the histogram of the peak wavenumber of the emission spectra.

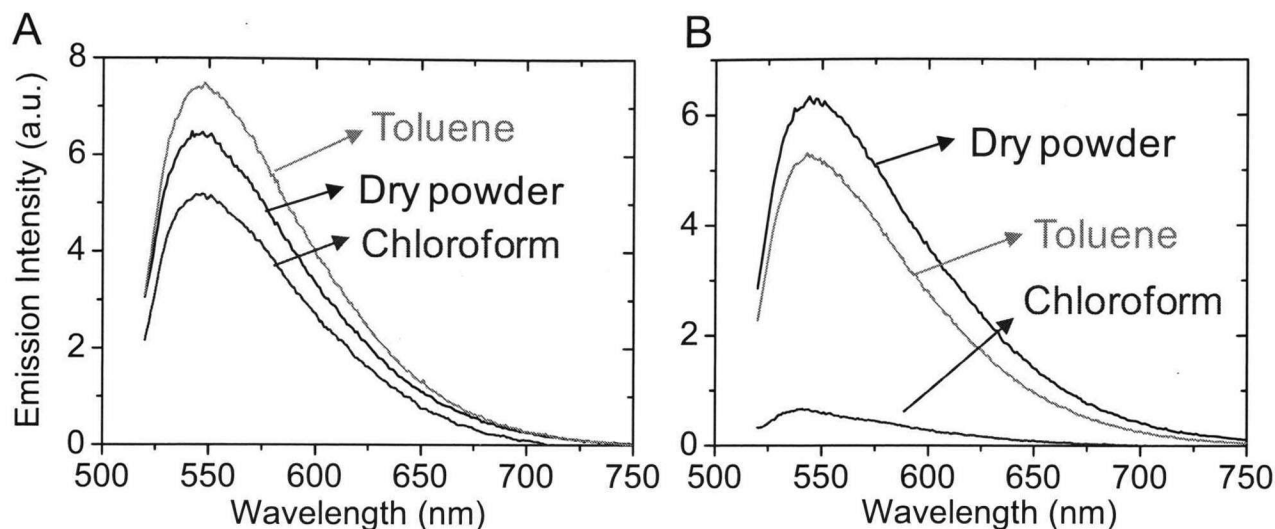


Figure 7. Ensemble-averaged emission spectra of fresh DNS@MOF-177 (A) and DNS molecules adsorbed on the decomposed MOF-177 (B). Spectral features observed from dry powder, in toluene, and in chloroform were directed, respectively. The irradiated areas of the samples were almost the same.

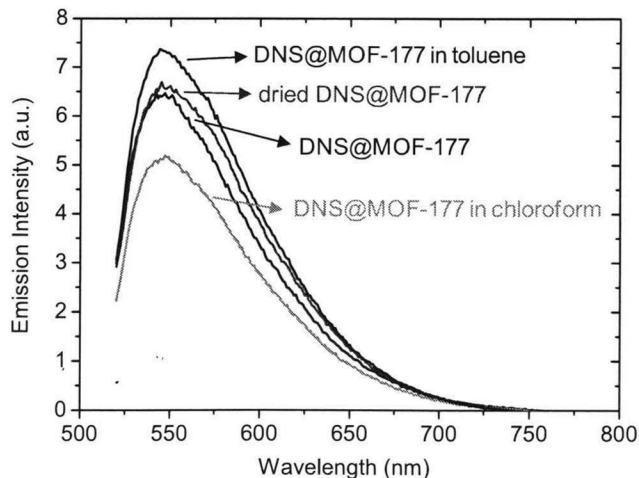


Figure 8. Emission spectra of DNS@MOF-177 in toluene and in chloroform. After the DNS@MOF-177 powder in chloroform was completely dried up, the emission intensity was recovered. This result suggests that DNS molecules encapsulated in MOF-177 are hardly desorbed from the MOF framework.

On the other hand, as shown in the right panel of Figure 7, the emission from DNS on the hydrated MOF-177, which has no microporous framework structure (the BET surface area is $9 \text{ m}^2 \text{ g}^{-1}$), was almost completely quenched in chloroform. This is consistent with the assumption that the well-defined MOF-177 structure effectively isolated the chromophores confined inside of its nanopores from the surrounding environment, thus suggesting that the molecular interaction of DNS with aromatic linkers of MOF-177 is more dominant than that with the solvent molecules. This interpretation is also supported by geometrical considerations in that the molecular size of DNS (1.7 nm length; 0.67 nm width)^{7,8} is comparable to the MOF-177 pore diameter (Scheme 1).^{9,10} To strengthen our conclusion, ensemble-averaged fluorescence lifetime measurements were carried out. The average fluorescence lifetimes observed for DNS@MOF-177 suspended in toluene and in chloroform were 3.2 and 3.1 ns, respectively, which are consistent with the time (2.9 ns) for DNS molecules in toluene (Figure 9 and Table 1).

In a highly polar solvent, the formation of a short-lived nonradiative TICT state is suggested.^{7,8} For the DNS@MOF-177 particles in toluene, it is not possible to fit the profile with a single-exponential function because of the distribution of lifetimes of DNS molecules adsorbed on the surface of MOF-177 particles. Therefore, the average lifetime, $\langle \tau \rangle$, was tentatively evaluated to be 3.2 ns (see Table 1). The fast decay component with a lifetime of 0.23 ns observed for the DNS@MOF-177 in chloroform is reasonably assigned to desorbed DNS molecules into the solution and/or surface-adsorbed DNS molecules on the MOF-177 particles.

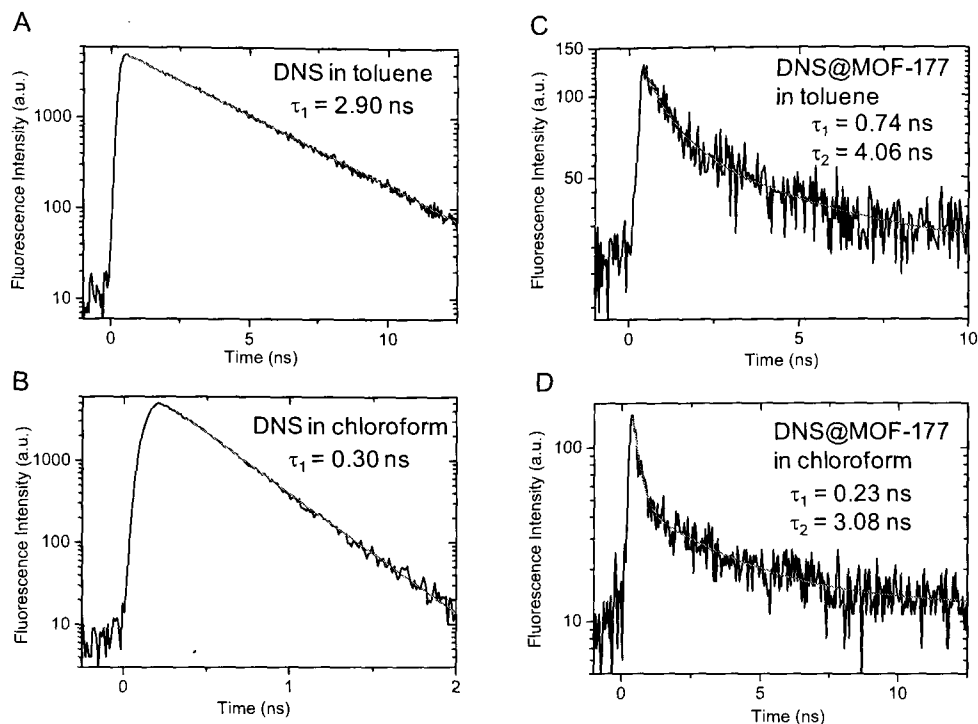


Figure 9. Fluorescence lifetimes observed for DNS in toluene (A) and in chloroform (B) (6 μM), and DNS@MOF-177 suspended in toluene (C) and in chloroform (D) (0.5 g L⁻¹). The excitation wavelength is 450 nm. The lines indicate single or double exponential curves fitted to the temporal profiles.

Table 1. Fluorescence Lifetimes and Maximum Wavelengths of Free DNS Molecules and DNS@MOF-177 Particles in Solutions

sample	τ_1 , ns (a_1 , %)	τ_2 , ns (a_2 , %)	$\langle \tau \rangle$, ns ^c	λ_{max} , nm
DNS in toluene	2.90 ^a	-	-	574 \pm 5
DNS in chloroform	0.30 ^a	-	-	703 \pm 5
DNS@MOF-177 in toluene	0.74 ^b (64)	4.1 ^b (36)	3.2	560 \pm 10
DNS@MOF-177 in chloroform	0.23 ^b	3.1 ^b	-	540 \pm 10

^a Errors within $\pm 5\%$. ^b Errors within $\pm 15\%$. ^c The average lifetime, $\langle \tau \rangle$, evaluated using the

$$\text{equation: } \langle \tau \rangle = \frac{\sum_{i=1}^{i=n} a_i \tau_i^2}{\sum_{i=1}^{i=n} a_i \tau_i}.$$

Solvent exchange experiments on single particles by utilizing a flow cell system enabled us to examine the local environment around DNS molecules in the MOF-177 framework (Scheme 2). As demonstrated in Figure 10, DNS@MOF-177 particles in toluene were observed as bright spots, while the emission intensity of DNS@MOF-177 in chloroform decreased but was easily distinguishable from the background. Although the difference in the ensemble averaged fluorescence intensity of DNS@MOF-177 caused by exchanging the solvent is relatively small, our single-particle data analysis revealed that individual particles exhibited significant changes in its intensity within several minutes by solvent exchange. The different responsiveness of each particle is probably explained because the deformed porous structures and microscopic surface cracks present in the individual particles would decrease and increase the penetration rates of solvent molecules into the framework, respectively. The process of solvent change is fully reversible since the higher intensity can be restored by switching back from chloroform to MOF-177 was completely quenched as the solvent was changed from toluene to chloroform. On the other hand,

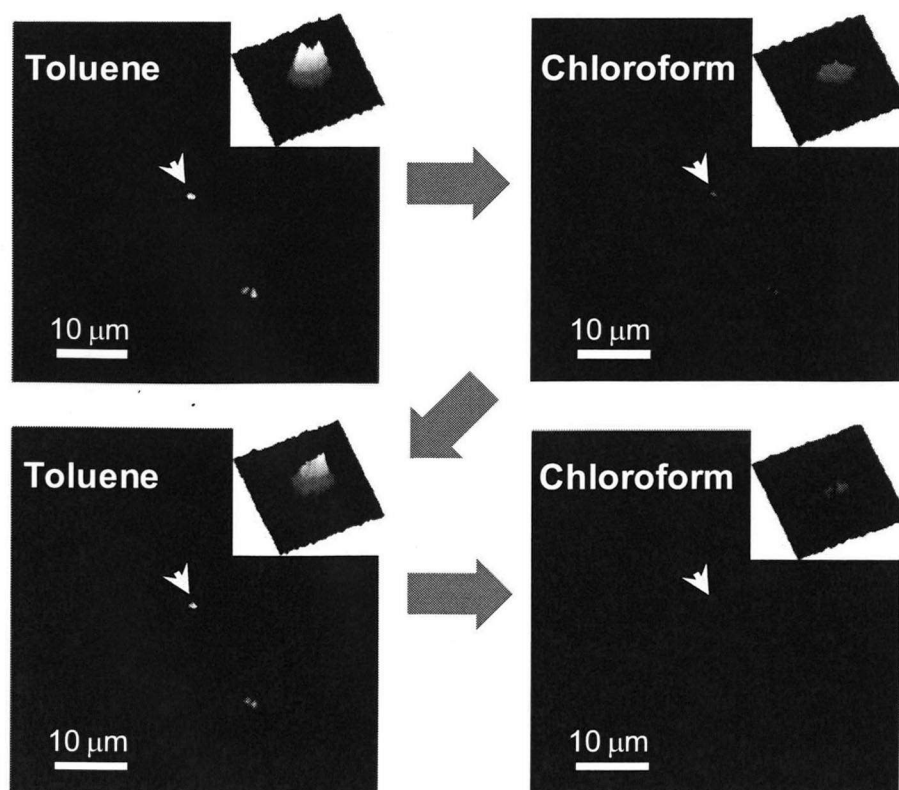


Figure 10. Single-particle fluorescence images of DNS@MOF-177 particles during solvent exchange. The immersion time in each solvent was 3 min. Insets show the magnified images ($4\ \mu\text{m} \times 4\ \mu\text{m}$) of the particle indicated by the arrows.

the fluorescence of DNS molecules adsorbed on the decomposed MOF-177 was completely quenched as the solvent was changed from toluene to chloroform (Figure 11).

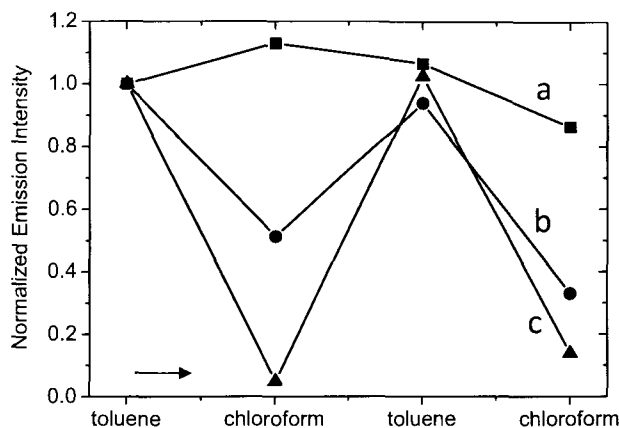


Figure 11. Normalized emission intensity changes observed for single MOF-177 (a) and DNS@MOF-177 (b) particles, and DNS molecules adsorbed on the decomposed MOF-177 (c) as the solvent was exchanged. The images were captured under static conditions (i.e., without solvent flow).

We further measured the bleaching rates of individual DNS@MOF-177 particles in ambient atmosphere. The typical bleaching behavior of DNS@MOF-177 is shown in Figure 12A. The continuous emission intensity decay profiles observed for individual DNS@MOF-177 particles are due to the high concentrations of dye molecules, that is, the sum of many photobleaching steps at different time scales. The bleaching time (τ) for most DNS@MOF-177 particles was longer than that for DNS molecules on the glass surface ($\tau \approx 14$ s); these values were calculated by using a single-exponential fitting of the recorded data for fluorescence intensity and the number of detected molecules as a function of time, respectively (Figure 13).¹⁵ Assuming that the photo-oxidation process is the major photochemical reaction responsible for the observed bleaching of DNS emissions, the penetration of oxygen molecules into fresh MOF frameworks can be efficiently restricted by steric hindrance in their structures.

The fluorescence intermittency or blinking phenomenon is an important characteristic of single-molecule (single-particle) spectroscopy.¹⁶⁻²² As demonstrated in Figure 12B and 12C, the on-off blinking of single DNS molecules was observed for some of the DNS@MOF-177 particles (about 10% of the particles) during the bleaching process. It should also be noted that no detectable translational diffusion of single DNS molecules in MOF-177 was confirmed during the course of the single-molecule experiments.²³ Here, a general approach was applied to define the intensity

threshold in order to distinguish between the on and off states.^{21,22} The off-time histogram does not show a single-exponential decay, thus inferring that the related reaction processes are intrinsically heterogeneous and cannot be characterized by a single rate constant. We thus analyzed the probability density of off time intervals (t_{off}) according to the simple power law, $P(t_{\text{off}}) = At^{-\alpha}$, where A is the scaling coefficient and R is the power law exponent.²¹ The determined R of 1.8 ± 0.1 ²⁴ is similar to those (1.4-2.0) reported for organic dyes¹⁶⁻¹⁹ and semiconductor quantum dots (QDs).²⁰⁻²² The observed fluorescence blinking may be explained by the following reasons. One possible explanation for complex blinking dynamics is the involvement of nonemissive twisted intramolecular charge-transfer (TICT) states which are closely related to torsional motions of specific bonds.^{7,8} Another potential explanation comes from proton transfer between the MOF-177 framework and DNS molecules, which results in protonation of the dimethylamino nitrogen in DNS.^{7,8,19,25} The local pore environment of MOF-177 may produce protons from organic linkers of

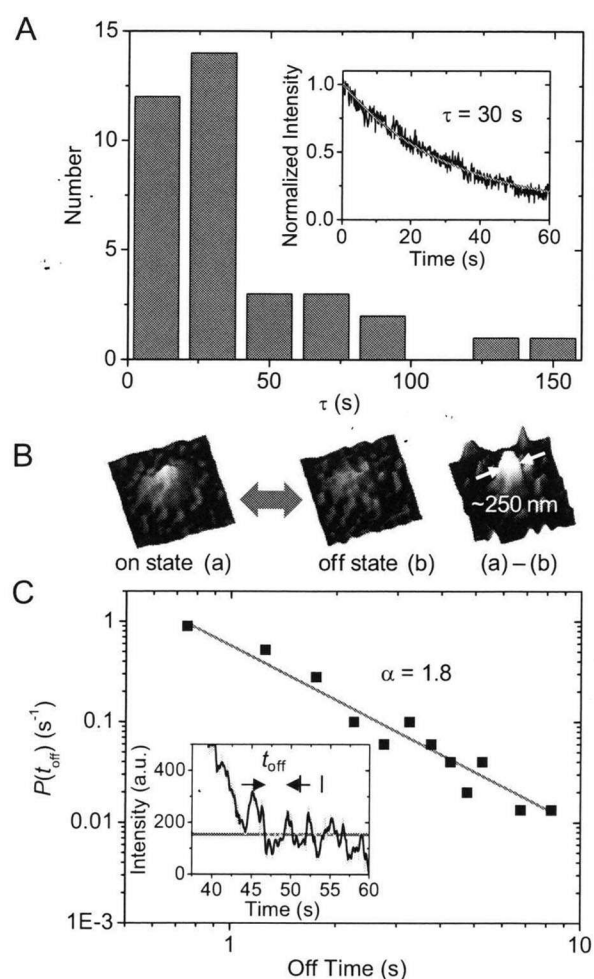


Figure 12. (A) Histogram of the bleaching time constant (τ) of DNS@MOF-177 on the cover glass in ambient atmosphere. The inset shows a typical trajectory of the emission intensity of DNS@MOF-177 during the 488 nm laser irradiation. The line indicates the single-exponential fit. (B) Typical single-molecule fluorescence “on” (a) and “off” (b) images and the differential image [(a)-(b)] ($1.3 \mu\text{m} \times 1.3 \mu\text{m}$). The fwhm of a single-molecule fluorescent spot is ~ 250 nm, which is comparable to the size of the diffraction-limited spot. (C) Off-time probability density, $P(t_{\text{off}})$, constructed from trajectories for 20 single DNS@MOF-177 particles (over 100 events). The red line indicates the power law fit. The inset shows the typical blinking behavior of a single DNS molecule encapsulated in the MOF-177 particles in toluene during the bleaching process. The analyzed area is approximately $300 \text{ nm} \times 300 \text{ nm}$. The blue line is the threshold level.

the framework structure through deprotonation under base conditions,²⁸ which makes proton transfer a viable mechanism for the observed blinking process. Further detailed studies of the blinking statistics are required to clarify the underlying mechanism.²⁹

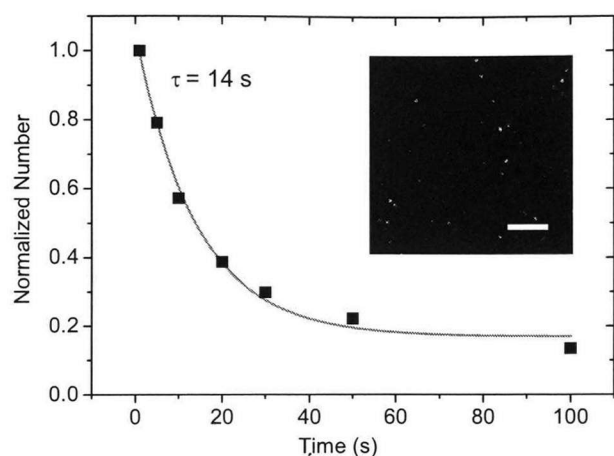


Figure 13. Photoirradiation time dependence of the number of single DNS molecules on the glass surface in ambient atmosphere. The bleaching time (τ) of 14 s was calculated by using a single-exponential fitting of the number of detected molecules as a function of time. The inset shows the single molecule fluorescence image observed for DNS molecules coated on a quartz cover glass under the 488 nm laser irradiation in ambient atmosphere. The scale bar

Conclusions

In summary, for the first time, we carried out in situ observations of host-guest interactions in individual dye encapsulated MOFs by utilizing single-molecule, single-particle fluorescence spectroscopy. Well-defined MOF-177 particles were found to act as good protection material against solvent penetration even if the MOF structure allowed the incorporation of rather large chromophores such as DNS. In the future, we intend to develop a strategy to fabricate novel host-guest composites of MOFs and a variety of functional molecules suitable for new applications including photoelectronic and optical devices.

References and Notes.

1. Yaghi, O. M.; O'Keeffe, M.; Ockwig, N. W.; Chae, H. K.; Eddaoudi, M.; Kim, J. *Nature* **2003**, *423*, 705-714.
2. Kitagawa, S.; Kitaura, R.; Noro, S. *Angew. Chem. Int. Ed.* **2004**, *43*, 2334-2375.

3. Long, J. R.; Yaghi, O. M. *Chem. Soc. Rev.* **2009**, 38, 1213-1214 (Metal-Organic Frameworks Issue).
4. Schüth, F.; Sing, K. S. W.; Weitkamp, J., Eds., *Handbook of Porous Solids*. Wiley-VCH: Weinheim, Germany, 2002.
5. Weckhuysen, B. M. *Angew. Chem. Int. Ed.* **2009**, 48, 4910-4943.
6. Roeffaers, M. B. J.; De Cremer, G.; Uji-i, H.; Muls, B.; Sels, B. F.; Jacobs, P. A.; De Schryver, F. C.; De Vos, D. E.; Hofkens, J. *Proc. Natl. Acad. Sci. U.S.A.* **2007**, 104, 12603-12609.
7. Gruen, H.; Görner, H. *J. Phys. Chem.* **1989**, 93, 7144-7152.
8. Lapouyade, R.; Kuhn, A.; Letard, J.-F.; Rettig, W. *Chem. Phys. Lett.* **1993**, 208, 48-58.
9. Chae, H. K.; Siberio-Pérez, D. Y.; Kim, J.; Go, Y. B.; Eddaoudi, M.; Matzger, A. J.; O'Keeffe, M.; Yaghi, O. M. *Nature* **2004**, 427, 523-527.
10. Furukawa, H.; Miller, M. A.; Yaghi, O. M. *J. Mater. Chem.* **2007**, 17, 3197-3204.
11. Tachikawa, T.; Choi, J. R.; Fujitsuka, M.; Majima, T. *J. Phys. Chem. C* **2008**, 112, 14090-14101.
12. The number of DNS molecules per particle before the washing procedure was roughly calculated to be about 200 molecules by taking the density of the material (0.427 g cm^{-3})¹⁰ and the average particle size ($\sim 600 \text{ nm}$).
13. Derouane, E. G. *J. Mol. Catal. A: Chem.* **1998**, 134, 29-45.
14. The slight difference in the peak wavelength between ensemble and single-particle experiments is possibly due to the contribution of decomposed (hydrated) particles and the spectral response of the detection system ($>520 \text{ nm}$).

15. The observed short bleaching time ($\tau \approx 10$ s) for some DNS@MOF-177 particles can be attributed to the presence of DNS adsorbed on the external surface of MOF-177.
16. Haase, M.; Hübner, C. G.; Reuther, E.; Herrmann, A.; Müllen, K.; Basché, T. *J. Phys. Chem. B* **2004**, *108*, 10445-10450.
17. Yeow, E. K. L.; Melnikov, S. M.; Bell, T. D. M.; De Schryver, F. C.; Hofkens, J. *J. Phys. Chem. A* **2006**, *110*, 1726-1734.
18. Barbon, A.; Bott, E. D.; Brustolon, M.; Fabris, M.; Kahr, B.; Kaminsky, W.; Reid, P. J.; Wong, S. M.; Wustholz, K. L.; Zanré, R. *J. Am. Chem. Soc.* **2009**, *131*, 11548-11557.
19. Bott, E. D.; Riley, E. A.; Kahr, B.; Reid, P. J. *ACS Nano* **2009**, *3*, 2403-2411.
20. Frantsuzov, P.; Kuno, M.; Jankó, B.; Marcus, R. A. *Nat. Phys.* **2008**, *4*, 519-522.
21. Kuno, M.; Fromm, D. P.; Hamann, H. F.; Gallagher, A.; Nesbitt, D. J. *J. Chem. Phys.* **2001**, *115*, 1028-1040.
22. Cui, S.-C.; Tachikawa, T.; Fujitsuka, M.; Majima, T. *J. Phys. Chem. C* **2008**, *112*, 19625-19634.
23. This would be due to the intermolecular interactions, such as van der Waals and π - π interactions, between DNS molecules and aromatic linkers of MOF-177 and/or the incorporation of defects in the framework.
24. Despite careful consideration, it was not possible to rule out the contribution of more than two molecules on the blinking statistics. This effect might lead to an increase in α .
25. Electron transfer might be considered to be responsible for complex blinking of organic chromophores.^{26,27} Two mechanisms of electron transfer versus proton transfer are quite different.^{18,19} At the present stage, however, there is no clear experimental evidence for the electron transfer between the excited DNS molecules and MOF-177.

26. Zondervan, R.; Kulzer, F.; Orlinskii, S. B.; Orrit, M. *J. Phys. Chem. A* **2003**, *107*, 6770-6776.
27. Biju, V.; Micic, M.; Hu, D.; Lu, H. P. *J. Am. Chem. Soc.* **2004**, *126*, 9374-9381.
28. Huang, L.; Wang, H.; Chen, J.; Wang, Z.; Sun, J.; Zhao, D.; Yan, Y. *Microporous Mesoporous Mater.* **2003**, *58*, 105-114.
29. A more exciting and ambitious possibility is the inherent flexibility of the MOF-177 framework that enables these volume changes. This structural change should govern both host-guest interactions and rotational dynamics of DNS molecules. In fact, a slight XRD peak shift toward lower 2θ angles was observed after immersion of MOF-177 and DNS@MOF-177 powders in toluene (Figure 1). This peak shift is possibly attributable to the swelling of MOF-177 frameworks.^{30,31}
30. Serre, C.; Mellot-Draznieks, C.; Surblé, S.; Audebrand, N.; Filinchuk, Y.; Férey, G. *Science* **2007**, *315*, 1828-1831.
31. Horike, S.; Shimomura, S.; Kitagawa, S. *Nat. Chem.* **2009**, *1*, 695-704.
32. Naito, K.; Tachikawa, T.; Fujitsuka, M.; Majima, T. *J. Am. Chem. Soc.* **2009**, *131*, 934-936.

General Conclusions

In this study, by utilizing various spectroscopic methods including single-particle fluorescence microscopy as well as time-resolved spectroscopic method, systematic studies of interfacial electron transfer between photoexcited MOFs particles and various organic compounds were carried out.

Chapter 1, we reported the nature of luminescence transitions in MOF-5_n and the interfacial charge transfer from the photoexcited MOF-5_n to the surface adsorbents. Basically, the optical transition responsible for the green emission of MOF-5 is similar to that observed from ZnO. However, there are significant differences in the temperature dependences of the PL intensity change and peak-energy shift, and in the activation energies for the thermal quenching or activation processes.

From the steady-state and time-resolved PL measurements, the bimolecular reaction rates between the photoexcited MOF-5_n and S, such as aromatic sulfides and amines, were determined. The one-electron oxidation reaction of S during the 355 nm laser flash photolysis of MOF-5_n in acetonitrile was directly examined using TDR spectroscopy. The relatively high oxidation efficiency of MOF-5_n compared to P-25 TiO₂ photocatalyst was found from the comparative studies on the amount of adsorbates and the concentration of S^{•+}. It should be noted that S^{•+} generated in the MOF-5 system has a significantly long lifetime of over 50 μ s. The theoretical calculation based on the Marcus theory for the electron transfer reactions revealed that relatively low HT rate and long lifetime of S^{•+} obtained for the MOF-5 system can be ascribed to the larger value of $\lambda_{v,D} = 1.2$ eV for the MOF-5_n (h_{tr}⁺)/MOF-5_n couple, contrary to semiconductor nanoparticles, such as ZnO and TiO₂. It is believed that the flexibility of the MOF structure and the accessibility of solvent molecules into the porous structure play important roles in overall reorganization of the charge transfer system. Moreover, the influence of adsorbed water on the photoinduced reaction processes of MOF-5_n was examined. Although the spectral assignment is incomplete, the electron transfer reactions with S were observed during the 355 nm laser flash photolysis of water-treated MOF-5_n (MOF-5_{aq}) powder in acetonitrile. It was concluded that the excited triplet state of terephthalate,

which is dissociated from the MOF structure, is involved in the redox processes.

Chapter 2, the one-electron oxidation processes of organic compounds under photoirradiation of nanosized and micro-sized Eu-MOF particles has been studied by combining time-resolved emission and absorption spectroscopy, confocal microscopy, and theoretical calculation based on the Marcus theory. These results suggest that Eu-MOFs work as an efficient photocatalyst under UV light irradiation and exhibit apparent size-selectivity for the organic compounds.

Chapter 3, in situ observations of host-guest interactions in individual dye-encapsulated MOFs by utilizing single-molecule, single-particle fluorescence spectroscopy were carried out. Well-defined MOF-177 particles were found to act as good protection material against solvent penetration even if the MOF structure allowed the incorporation of rather large chromophores such as DNS.

As a relatively new class of materials, MOFs will continue to attract interest and inquiry by both academia and industry. They exhibit considerable potential applications of molecular-recognitive MOF photocatalysts for extending their photosensitivity toward the visible light region by varying both the length of the organic backbone of the ligands and the degree of conjugation in the ligands. It can be developed a strategy to fabricate novel host-guest composites of MOFs and a variety of functional molecules suitable for new applications including photoelectronic and optical devices.

The expectation of this thesis is that it can serve not only as a reference brochure for the experienced researchers in the MOF field, but also as an introduction booklet for those who are interested in MOFs and those just enter this field.

List of Publications

1. Photoinduced charge-transfer processes on MOF-5 nanoparticles: Elucidating differences between metal-organic frameworks and semiconductor metal oxides
Takashi Tachikawa, **Jun Rye Choi**, Mamoru Fujitsuka, and Tetsuro Majima
J. Phys. Chem. C **2008**, *112*(36), 14090-14101.
2. Europium-based metal-organic framework as a photocatalyst for one-electron oxidation of organic compounds
Jun Rye Choi, Takashi Tachikawa, Mamoru Fujitsuka, and Tetsuro Majima
Langmuir **2010**, *26*(13), 10437-10443.
3. Evaluating host-guest interactions in a metal-organic framework using a polarity-sensitive probe
Jun Rye Choi, Takashi Tachikawa, Mamoru Fujitsuka, and Tetsuro Majima
J. Phys. Chem. Lett. **2010**, *1*(7), 1101-1106.

Acknowledgements

The author wishes to express her sincere gratitude to Professor Tetsuro Majima for his kind guidance, valuable suggestions, and encouragement during her studies. It has been great pleasure for the author to study in his research group. The author is deeply grateful to Assistant Professor Takashi Tachikawa for his helpful advice, discussions, and encouragement. The author is also indebted to Associate Professor Mamoru Fujitsuka, Associate Professor Kiyohiko Kawai, Specially Appointed Professor Akira Sugimoto, and Specially Appointed Assistant Professor Jung Kweon Choi for their helpful suggestions. The author is deeply grateful to Professor Sung Sik Kim, Department of Chemistry, Chonbuk National University, for his valuable suggestions.

The author is deeply grateful to Professor Yoshihisa Inoue and Professor Shuhei Seki, and all Professor of Department of Applied Chemistry, Graduate School of Engineering, Osaka University, for their valuable suggestions.

The author is grateful working with members of Professor Majima's research group, including Dr. Takumi Kimura, Miss Nan Wang, Mr. Man Jae Park, Mr. Shi-Cong Cui, Mr. Kyu Chan Song, Miss Eri Matsutani, Mr. Soichiro Yamashita, Miss Soo Yeon Kim, Mr. Mitsuo Hayashi, Mr. Tomoyuki Yonezawa, Miss Mayuka Ishikawa for their suggestions and hearty encouragement. The author thanks all the past members of Professor Majima's research group for their friendship and helpful discussions.

The author thanks the Ministry of Education, Culture, Sports, Science and Technology (MONBUKAGAKUSHO: MEXT) of the Japanese Government for the financial support.

Finally, the author expresses to thank her family and friends so much for their endless supports, encouragement and love during my graduate study.

2010. 9.

Jun Rye Choi

